

**Understanding Organic Photovoltaic Cells:  
Electrode, Nanostructure, Reliability, and Performance**

by

**Myung-Su Kim**

A dissertation submitted in partial fulfillment  
of the requirements for the degree of  
Doctor of Philosophy  
(Materials Science and Engineering)  
in The University of Michigan  
2009

Doctoral Committee:

Professor Jinsang Kim, Chair  
Professor L. Jay Guo  
Professor Max Shtein  
Professor Anton Van der Van

© Myung - Su Kim 2009  
All Rights Reserved

**To Joseph, Rachel, Sung-Hee and my family in South Korea**

## ACKNOWLEDGMENTS

After four long years, it is time to complete my Ph.D. studies. At the beginning of this program, my lack of research experience meant I had to spend much time learning about the research system. To me, pursuing a Ph.D. meant taking complete responsibility for understanding information accurately, successfully applying knowledge, designing and managing experiments in a productive manner, using research creatively in my topic selection, setting criteria to scientifically analyze results, contributing to professional society, and ensuring effective communication. I would like to thank Prof. Jinsang Kim for his patience and guidance during my graduate studies. Prof. Kim consistently showed his trust and belief in me, and this strongly motivated me to achieve my goals. I am also thankful for my committee members; Professors L. Jay Guo, Anton Van der Van, and Max Shtein deserve special thanks for their work on this thesis committee. They provided professional discussions and collaboration opportunities that I greatly appreciate.

In addition, the support of my family was a great asset, and without it, I could not have earned this Ph.D. When I began studying in the United States, Rachel was 1 year old and Joseph was not yet born. How time has flown. Rachel is now a 2<sup>nd</sup> grade elementary school student and my son has begun to speak. Before I began my studies in the U.S., I wrote a letter to my 6-month-old daughter in which I promised to be a good father. Frankly speaking, balancing my education with fatherhood was not easy. However, Sung-Hee's devotion to the raising of our children has enabled me to focus on my research more than would be possible otherwise. I give my sincerest thanks to Rachel and Joseph for their big smiles and for constantly showing their love for me.

My family in South Korea has also provided great mental support. I have encountered many hurdles during this journey, and my family's love and encouragement has kept me focused.

These supports have been a great part of the world I have experienced so I am happy.

## TABLE OF CONTENTS

<b>DEDICATION.....</b>	<b>ii</b>
<b>ACKNOWLEDGMENTS .....</b>	<b>iii</b>
<b>LIST OF FIGURES .....</b>	<b>ix</b>
<b>LIST OF TABLES .....</b>	<b>xii</b>
<b>ABSTRACT.....</b>	<b>xiii</b>
<b>CHAPTER 1 INTRODUCTION.....</b>	<b>1</b>
1.1 Photovoltaic Effect.....	1
1.2 Brief History of Photovoltaic Cell .....	3
1.3 Thesis flow.....	5
1.4 Reference .....	6
<b>CHAPTER 2 BACKGROUND.....</b>	<b>7</b>
2.1 Scope of the Background .....	7
2.2 History of OPV cells.....	8
2.2.1 Single layer OPV cells.....	8
2.2.2 Bilayer OPV cells .....	9
2.2.3 Bulk Heterojunction OPV cells .....	10
2.3 Device Physics of OPV Cells .....	14
2.3.1 General Working Principle.....	14
2.3.2 Device Physics of Organic Blend PV Cell.....	18

2.4 Strategies to improve the OPV device performance.....	21
2.4.1 Bandgap Tuning and Tandem Cell.....	21
2.4.2 Nanostructured PV Cell.....	24
2.4.3 High Mobility Semiconducting Organic .....	29
2.5 General Experimental Materials and Methods .....	32
2.5.1 General Materials .....	32
2.5.2 Processing Techniques .....	35
2.6 References.....	38

<b>CHAPTER 3 THE EFFECTS OF PROCESSING PARAMETERS ON THE REPRODUCIBILITY OF ORGANIC PHOTOVOLTAIC CELLS: P3HT AND PCBM BLENDS SYSTEM .....</b>	<b>39</b>
3.1 Introduction.....	39
3.2 Experimental.....	42
3.3 Results and discussion .....	43
3.3.1 Blend layer quality .....	43
3.3.2 LiF as an interlayer between blend layer and cathode .....	45
3.3.3 Minor effect of oxidation on reproducible performance of OPV cell .....	48
3.3.4 Excellent reproducible performance of OPV cell through optimization.....	49
3.4 Conclusions.....	54
3.5 References.....	55

**CHAPTER 4 THE EFFECTIVE VARIABLES TO CONTROL FILL  
FACTOR OF ORGANIC PHOTOVOLTAIC CELLS.....56**

4.1 Introduction.....56

4.2 Experimental.....59

    4.2.1 Materials .....59

    4.2.2 Device fabrication and characterization.....59

4.3 Results and discussion .....60

    4.3.1 Blend morphology effect on FF.....60

    4.3.2 The effect of regioregularity of conjugated polymer  
        on FF .....63

    4.3.3 Blend film thickness effect on FF.....63

    4.3.4 The effect of interface between blend layer and  
        electrode on FF .....64

    4.3.5 The effect of light intensity on FF .....68

4.4 Conclusions.....70

4.5 References.....71

**CHAPTER 5 CHOICE OF ELECTRODE GEOMETRY FOR ACCURATE  
MEASUREMENT OF ORGANIC PHOTOVOLTAIC CELL  
PERFORMAMNCE.....72**

5.1 Introduction.....72

5.2 Experimental.....74

    5.2.1 Device fabrication.....74

    5.2.2 Electrode patterning .....74

5.2.3	Device characterization.....	74
5.3	Results and discussion .....	76
5.3.1	Observation of overestimation of OPVC performance .....	76
5.3.2	Evidences of extra current .....	79
5.3.3	Quantitative analysis of extra current of OPVC .....	81
5.5	Conclusions.....	83
5.6	References.....	84

**CHAPTER 6 FLEXIBLE CONJUGATED POLYMER PHOTOVOLTAIC  
CELLS WITH CONTROLLED NANOSCALE HETEROJUNCTIONS  
FABRICATED USING NANOIMPRINT LITHOGRAPHY .....86**

6.1	Introduction.....	86
6.2	Experimental.....	88
6.2.1	Fabrication of the SiO <sub>2</sub> mold .....	88
6.2.2	Device fabrication and characterization.....	88
6.3	Results and discussion .....	91
6.3.1	Design principle of nanostructured OPV cell.....	91
6.3.2	Nanoimprinting lithography as a patterning tool.....	91
6.3.3	Performance enhancement of nanostructured .....	94
6.4	Conclusions.....	97
6.5	References.....	98



<b>CHAPTER 7 SUB MICROMETER SCALE PATTERNED ORGANIC PHOTOVOLTAIC DEVICE USING TiO<sub>2</sub> AND P3HT.....</b>	<b>100</b>
7.1 Introduction.....	100
7.2 Experimental.....	102
7.3 Results and discussion .....	105
7.4 Conclusions.....	108
7.5 References.....	109
 <b>CHAPTER 8 CONCLUSIONS.....</b>	 <b>110</b>
8.1 Conclusions.....	110
8.1.1 Highly reproducible performance of blend OPV cell .....	110
8.1.2 The relations between fill factor and resistance.....	111
8.1.3 Accurate characterization.....	113
8.1.4 The performance enhancement of OPV cell having patterned interface between donor and acceptor .....	114

## LIST OF FIGURES

<b>Figure 1.1.</b> Solar spectrum.....	1
<b>Figure 1.2.</b> Photoelectric effect and photovoltaic effect. ....	2
<b>Figure 1.3.</b> Chronicle overview of oil price.....	4
<b>Figure 2.1.</b> The device structures of OPV cells .....	9
<b>Figure 2.2.</b> Photoinduced charge transfer from conjugated polymer.....	10
<b>Figure 2.3.</b> Morphology of P3HT and PCBM blend OPV Cell.....	12
<b>Figure 2.4.</b> Morphology of CdSe and P3HT blend and device performance.....	13
<b>Figure 2.5.</b> Device working principle from light absorption to charge collection.....	14
<b>Figure 2.6.</b> The definition of fill factor and circuit of photovoltaic .....	15
<b>Figure 2.7.</b> J-V curves under dark condition and illumination .....	17
<b>Figure 2.8.</b> The Absorption Characteristics of Conjugated Polymers .....	23
<b>Figure 2.9.</b> Nanostructured OPV Cell Structure .....	26
<b>Figure 2.10.</b> Nanostructured OPV Cell Using PRINT Process.....	27
<b>Figure 2.11.</b> CuPc and PTCBI-based Nanostructured OPV Cell.....	28
<b>Figure 2.12.</b> Hole mobilities of Organic Semiconductors .....	30
<b>Figure 2.13.</b> Scheme of Spin Coating Process.....	35
<b>Figure 2.14.</b> Nanoimprint Lithography Process Scheme .....	36
<b>Figure 2.15.</b> Diagram of Vacuum Evaporator.....	37
<b>Figure 3.1.</b> J-V curves with optical microscopy images of the spincast P3HT and PCBM blend solution .....	44

<b>Figure 3.2.</b> Schematic band diagrams having charge trapping and accumulation by aggregate impurities. Black bars in the band diagram indicate possible barrier or trap by the aggregates of P3HT and PCBM. ....	45
<b>Figure 3.3.</b> J-V curves of ITO/ PEDOT:PSS/ P3HT+PCBM/ Al devices .....	46
<b>Figure 3.4.</b> J-V curves from OPVC w/o LiF layer and w/ LiF layer .....	47
<b>Figure 3.5.</b> The degradation of OPVC .....	49
<b>Figure 3.6.</b> The reproducible device performance of five OPVCs .....	50
<b>Figure 3.7.</b> The Performance variations of OPV cells .....	51
<b>Figure 3.8.</b> The performance variation of OPVC having different device sizes.....	52
<b>Figure 4.1.</b> The definition of fill factor and relations with $R_s$ and $R_{sh}$ .....	57
<b>Figure 4.2.</b> The annealing effect on the FF of OPVCs .....	61
<b>Figure 4.3.</b> The regio regularity effect of conjugated polymers on FF.....	62
<b>Figure 4.4.</b> Thickness effect on FF .....	64
<b>Figure 4.5.</b> The interface effect between the cathode and the blend layer on FF .....	65
<b>Figure 4.6.</b> The effect of anode conductivity and illumination intensity effect on FF .....	67
<b>Figure 4.7.</b> JV curves of a P3HT and PCBM blend photovoltaic device under various illumination intensities .....	68
<b>Figure 5.1.</b> J-V curves of OPVCs having island type electrode geometry and crossbar-type electrode geometry.....	77
<b>Figure 5.2.</b> Characterization scheme of OPVC having crossbar-type electrode geometry under illumination larger than the overlapped area of the crossbar-type electrodes. Excess current generation in PEDOT:PSS//Al device where there is no ITO. ....	78
<b>Figure 5.3.</b> J-V curves of devices having crossbar-type electrode geometry under various sizes of illumination.....	78

<b>Figure 5.4.</b> The plot of excess current ( $I_{sc}-I_{sc}^*$ ) from PEDOT:PSS//Al device vs. extra device area of PEDOT:PSS//Al device .....	80
<b>Figure 5.5.</b> J-V curves of organic photovoltaic cells having crossbar-type electrode geometry as the aluminum cathode was cut to remove excess current from PEDOT:PSS//Al device .....	80
<b>Figure 6.1.</b> Nanostructured conjugated polymer solar cells fabricated using NIL .....	90
<b>Figure 6.2.</b> SEM images of TDPTD on a flexible ITO-coated PET which imprinted with grating molds .....	92
<b>Figure 6.3.</b> A flexible conjugated polymer solar cell with controlled nanoscale heterojunctions .....	94
<b>Figure 6.4.</b> Characterization of the imprinted device performance .....	95
<b>Figure 7.1.</b> Device fabrication scheme.....	103
<b>Figure 7.2.</b> SEM images of the patterned $TiO_2$ .....	106
<b>Figure 7.3.</b> Absorption spectra of OPV cell (left), and JV curves of the control cell and the imprinted cell (blue open square) .....	107

## LIST OF TABLES

<b>Table 3.1.</b> The statistical analysis of comprehensive device performance of OPV cells .....	52
<b>Table 4.1.</b> The performances of P3HT and PCBM blend photovoltaic devices under different various annealing conditions.....	62
<b>Table 4.2.</b> Device performances of P3HT and PCBM blend photovoltaic devices having different regioregularity of the conjugated polymer .....	63
<b>Table 4.3.</b> The device performance depending on blend layer thickness effect .....	64
<b>Table 4.4.</b> FF change depending on the interface between cathode and blend layer .....	66
<b>Table 4.5.</b> Device performances depending on anode conductivity .....	67
<b>Table 4.6.</b> Device performances depending on illumination intensity.....	67
<b>Table 4.7.</b> The device performances of a P3HT and PCBM blend photovoltaic device under various illumination intensities .....	69
<b>Table 5.1.</b> Illumination area dependence of OPVCs (2 x 2 mm <sup>2</sup> ) having crossbar type electrode.....	79
<b>Table 6.1</b> The performance of the flexible solar cells with controlled nanostructures .....	96

## ABSTRACT

My Ph.D. research has focused on alternative renewable energy using organic semiconductors. During my study, first, I have established reliable characterization methods of organic photovoltaic devices. More specifically, less than 5% variation of power conversion efficiency of fabricated organic blend photovoltaic cells (OBPC) was achieved after optimization. The reproducibility of organic photovoltaic cell performance is one of the essential issues that must be clarified before beginning serious investigations of the application of creative and challenging ideas.

Second, the relationships between fill factor (FF) and process variables have been demonstrated with series and shunt resistance, and this provided a chance to understand the electrical device behavior. In the blend layer, series resistance ( $R_s$ ) and shunt resistance ( $R_{sh}$ ) were varied by controlling the morphology of the blend layer, the regioregularity of the conjugated polymer, and the thickness of the blend layer. At the interface between the cathode including PEDOT:PSS and the blend layer, cathode conductivity was controlled by varying the structure of the cathode or adding an additive.

Third, we thoroughly examined possible characterization mistakes in OPVC. One significant characterization mistake is observed when the crossbar electrode geometry of OPVC using PEDOT:PSS was fabricated and characterized with illumination which is larger than the actual device area. The hypothesis to explain this overestimation was excess photo-current generated from the cell region outside the overlapped electrode area, where PEDOT:PSS plays as anode and this was clearly supported with investigations.

Finally, I incorporated a creative idea, which enhances the exciton dissociation efficiency by increasing the interface area between donor and acceptor to improve the power conversion efficiency of organic photovoltaic cells. To achieve this, nanoimprint

lithography was applied for interface area increase. To clarify the effect of the interface area between donor and acceptor, we used two kinds of device structures. One was ITO/thermally deprotectable poly thiophene (TDPTD) /PCBM/Al and the other was ITO/TiO<sub>2</sub>/P3HT/gold (Au). In both cases, the enhanced device performance depending on the interface area was observed.

# CHAPTER 1

## INTRODUCTION

### 1.1 The Photovoltaic Effect

Photovoltaic cells generate useful electric energy from sun light through multiple steps of energy conversion processes . Light is made up of packets of energy, called photons, whose energy depends on the frequency, or color, of the light. The solar spectrum covers ultra violet to infrared wavelength ranges. Only 30% of incident light energy is in the visible light range, while over 50% is in the infrared range. The photons in UV and visible range have enough energy to pump electrons in semiconducting material, and this can be effectively used for charge generation. However, IR waves are too weak to generate electricity using conventional PV technology.

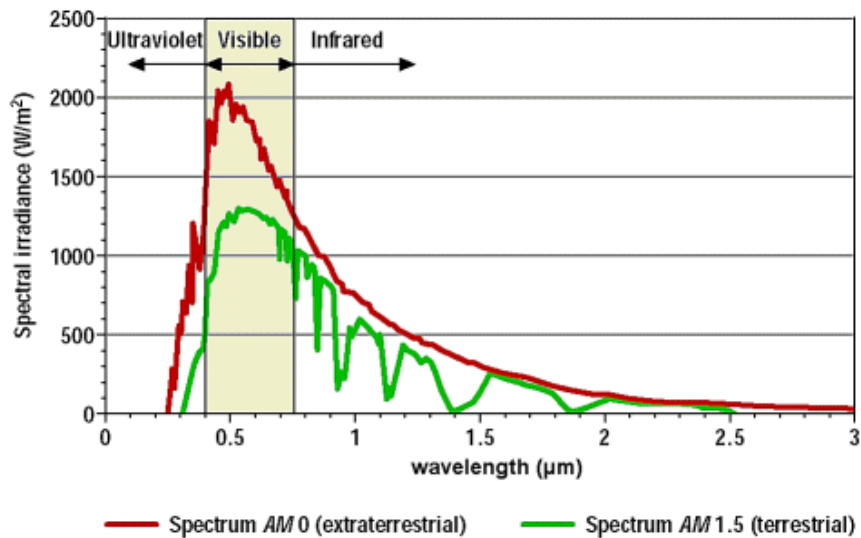
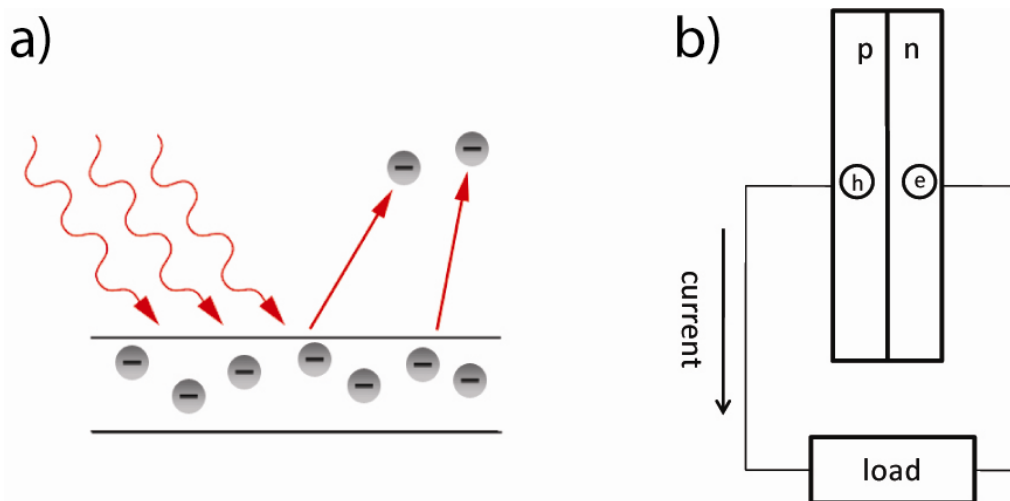


Figure 1.1. Solar spectrum.



The photovoltaic effect was discovered in 1839 by Edmund Becquerel, a French experimental physicist who experimented with an electrolytic cell made up of two metal electrodes. Becquerel found that certain materials produced small amounts of electric current when exposed to light. In 1905, Einstein explained the photoelectric effect, which established the foundation for a theoretical understanding of the photovoltaic effect. When photons in the UV range are illuminated on a metal surface, free electrons escape from the metal surface due to excitation energy from the incident light. They are then ejected into the atmosphere. In most cases, when absorbed photons in a material pump ground state electrons to the excited state the excited electrons promptly relax to the ground state. However, in photovoltaic devices, the excited electrons and the produced hole in the ground state should be collected separately to produce power.



**Figure 1.2.** a) Photoelectric effect and b) Photovoltaic effect.

Let's discuss the photovoltaic process in more detail. The photovoltaic process is composed of four steps: light absorption, charge generation, charge transport, and charge collection.<sup>1</sup> Light absorption occurs when the material has a semiconducting property that responds to incident waves. The absorption characteristic is dependent on the bandgap of the semiconducting material and its intrinsic extinction coefficient. The next step is charge generation. When the incident photon hits electrons at the ground state, inorganic semiconductors generate free carriers. However, in organic semiconductors, excited electrons slightly relax and then form an exciton, a bounded electron and hole pair. To

make an efficient organic photovoltaic cell, effective dissociation of excitons is a key issue because the binding energy of the exciton is large.<sup>2</sup> Once the excitons are dissociated the next step is the charge transport process, involving the transport of dissociated charges to electrodes through charge transporting pathways. During the charge transport, if the transporting medium has defects such as charge traps or barriers that hinder charge transport, cell performance decreases. Removing this loss mechanism during the transport process should be achieved to improve the cell performance. The final step is the charge collection, which occurs when the transported charges are collected from the semiconductor to the cathode or anode at the interface. When the interface is not carefully optimized, it can cause a dissipating sink of the transported charges.

## **1.2 A Brief History of the Photovoltaic Cell**

Forty years after Edmund Bequerel discovered the photovoltaic effect from the immersed platinum in electrolytes, William Adams and Richard Day observed the photovoltaic effect in a sample of selenium placed between two metal electrodes. This was the first solid photovoltaic device. The photovoltaic effect in this device originates from the association of selenium and metal. Twenty years later, Charles Fritts developed the first large-area photovoltaic device. Each of these early cells was comprised of a metal electrode/ semiconductor/ semitransparent thin metal electrode with a bottle neck to transmit incident light. Due to this limitation, the resulting power conversion efficiency was limited to less than 1%.

In the 1950s, PV cells achieved significant improvement over PCE and found a first practical application. In 1954, Bell Labs revealed the first high-power silicon PV cell, which used a p-n junction and reported a PCE of 6%.<sup>3</sup> Excited by this outstanding achievement, the *New York Times* forecasted that solar cells would eventually harness the “limitless energy of the sun.” In 1958, PV array-powered radios appeared on the US Vanguard I space satellite, and this was the first time PV technology was practically utilized. In this period, there also appeared PV cells made of cadmium sulphide, gallium arsenide, cadmium telluride, and indium phosphide. However, each technology had its own disadvantage. For example, cadmium, which is used in CdS and CdTe PV cells, is a

toxic element, GaAs-based PV cells are very expensive to produce, and the indium used in InP PV cells is limited. Therefore, silicon-based PV cells were regarded as the most promising PV technology.<sup>4</sup>

In the 1970s, two oil crises facilitated research on photovoltaic technology that improved the performance of PV cells. Research focused on developing device physics and process technology.<sup>5</sup> Methods to reduce the production costs of thin film technologies using amorphous silicon or microcrystalline silicon were also actively investigated. Additionally, research into tandem cell structures and bandgap tuning of semiconducting materials was conducted during this period to improve power conversion efficiency.<sup>6</sup> However, at this point in time, the mass production of infra for semiconducting devices was not well advanced, and production costs were still high compared to those of oil.

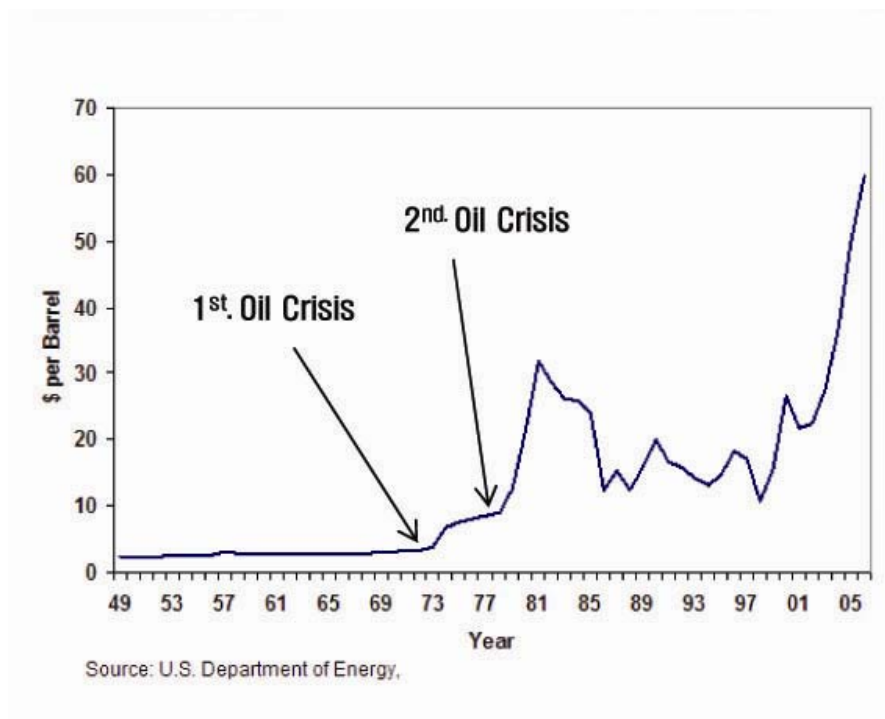


**Figure 1.3.** Chronicle overview of oil price.

In the 1990s and 2000s, interest in photovoltaics increasingly expanded. In large part, this interest has been prompted by the widespread deregulation of the energy supply and environmental issues related to global warming, which has increased the desire to secure alternative energy sources.<sup>7</sup> For example, the price for a barrel of oil was recently

around \$150.00, and this fact influenced governments and companies to seek alternative energy sources to reduce their reliance on oil. Also, governments in many nations offer subsidies for 1/3 to 1/2 of total PV system installation costs, which has accelerated the creation of large companies based on PV technology. In the first decade of the 2000s, PV technology has begun to impact the world by encouraging the expansion of energy resources from oil to green energy.<sup>4</sup>

In this context, recent concepts for organic semiconductors were established by Alan J. Heeger, Alan G. MacDiarmid, and Hideki Shirakawa, who won the Nobel prize for their contribution.<sup>8</sup> Their finding was really astonishing because it highlighted the potential transition of PV materials from inorganic to organic semiconductors, which could lower production costs and ease of processing. This discovery has promoted a lot of active research. This dissertation focuses on PV cells that use organic semiconductors, and reports on these investigations as follows.

### **1.3 Thesis Organization**

The background chapter covers general information about the device working principles, materials, fabrication methods, and device structures of organic PV cells. At the end, strategies to improve the PCE of PV cells are briefly introduced.

Chapters 3 and 4 discuss device fabrication optimization and device behavior understanding of OBPC. The work discussed in these chapters was essential for the production of reliable data from the following experiments. Chapter 5 discusses a proper electrode geometry for correct and reproducible performance. Chapters 6 and 7 report the improvement in OPVC performance achieved by improving exciton dissociation efficiency by making a patterned donor and acceptor interface. This sub-micrometer scale patterned interface also played a role as a light trapper, and additional performance improvement was achieved. Exciton dissociation was mainly improved by increasing the interface between donor and acceptor by using nanoimprinting lithography. The final chapter 8 draws relevant conclusions, discusses the lessons learned, and suggests directions for further research.

#### 1.4 References

1. Stephen R. Forrest, *MRS bulletin* **30**, 28-32 (2005).
2. M. Knupfer, *Appl. Phys. A: Mater. Sci. & Proc.*, **77**, 623-626 (2003).
3. E. Lorenzo, *Solar Electricity: Eng. of Photovoltaic System*. (Progensa, 1994).
4. D. Anderson, *Clean Electricity from Photovoltaics*. (London Imperial College Press, 2001).
5. M. Wolf, *Historical development of solar cells*. (IEEE press, 1976).
6. M. A. Green, *Photovoltaics: Coming of Age*. (Conf. Record 21st IEEE Photovoltaic Specialists Conf., 1990)
7. T. Markvart, *Solar Electricity*. (Wiley, 2000).
8. Edwin J. Louis Hideki Shirakawa, Alan G. MacDiarmid, Chwan K. Chiang and Alan J. Heeger, *J. Chem. Soc.*, 578-580 (1977).

## **CHAPTER 2**

### **BACKGROUND**

#### **2.1 Scope of the Background**

This chapter focuses on organic photovoltaic technology, and introduces more details about the history of OPV technology, device physics, and strategies to improve the performance. In describing the history of OPV cells, significant achievements in device performance are addressed according to the development of the device structure. The device physics of OPV cells have not yet been fully established, but as an example, the ‘expanded pn junction model’ is introduced, and the parameters characterizing the device’s performance are derived. In addition, various strategies to improve the performance of OPV cells are discussed based on device operating principles.

## 2.2 History of OPV Cells

### 2.2.1 Single layer OPV Cell

The single layer device structure of OPV cells is comprised of a transparent electrode/organic photosensitive semiconductor/electrode. (Figure 2.1) In 1994, this structure was created by R. N. Marks *et al.* using 50-320 nm thickness of poly (*p*-phenylene vinylene) (PPV) sandwiched between an ITO and a low work function cathode. The reported quantum efficiencies for this device were around 0.1% under 0.1mW/cm<sup>2</sup> intensity.<sup>1</sup>

This low quantum efficiency resulted from intrinsically low mobility of charges through semiconducting organics. The carrier mobility of semiconducting organics remains around 10<sup>-3</sup> cm<sup>2</sup>/V·s, while the mobility of single crystalline silicon is about 10<sup>3</sup> cm<sup>2</sup>/V·s order. This indicates that the photogenerated charges in semiconducting organics require more time to be collected from electrodes. The slow charge transport itself decreases the efficiency of the OPV cell, but also increases the recombination chance of charges in the device. The other problem that causes the low PCE of OPV cells is exciton formation, which are strongly bound dipole charges of photoexcited semiconducting organics.<sup>2</sup> Free electrons and holes are desired as an efficient charge carrier because the bound exciton requires an additional exciton dissociation step to make free carriers, which can decrease the carrier generation efficiency. In a single layer OPV cell, only one place to dissociate excitons into free carriers is the interface between semiconducting organics and a cathode. Later, it was known that the excitons are more efficiently dissociated at the interface between donor and acceptor, and a bilayer OPV cell was developed by inserting an acceptor layer between a donor semiconducting organic and a cathode.

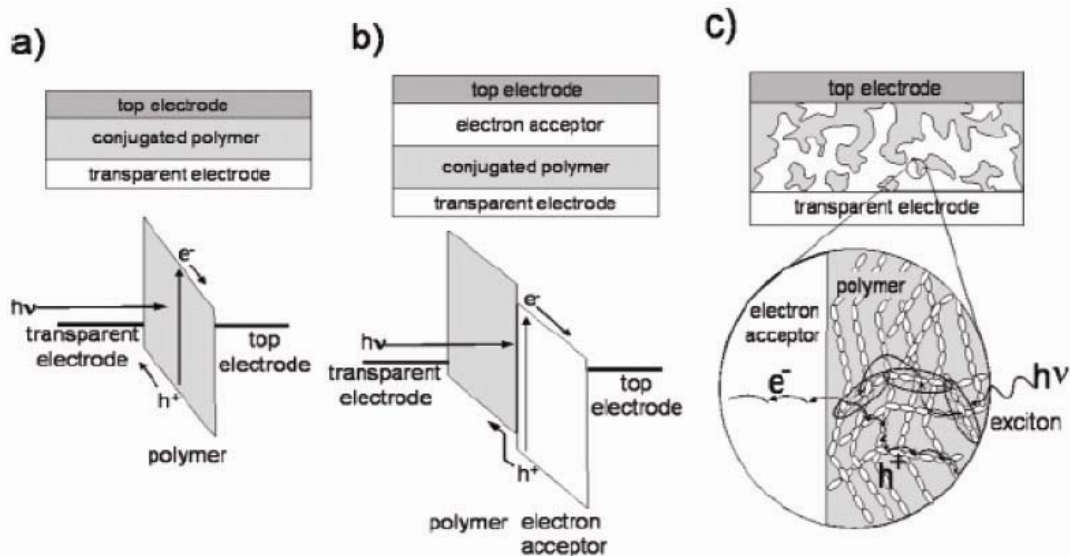


**Figure 2.1.** The device structures of OPV cells: a) Single layer OPV cell; b) Bilayer OPV cell; c) Bulk heterojunction OPV cell.

### 2.2.2 Bilayer OPV Cells

The bilayer OPV cell structure includes an additional electron transporting layer than is found in the single layer OPV structure. (Figure 2.1 b) This structure was first realized by C. W. Tang in 1985 and the device structure was comprised of indium tin oxide (ITO)/ copper phthalocyanine (CuPc)/ perylene tetracarboxylic derivative (PV)/ silver (Ag).<sup>3</sup> The reported PCE was 1% under simulated AM2 conditions. This ten-fold PCE increase resulted from improving exciton dissociation efficiency by adding electron transporting material that forms an offset energy band with hole transporting material.

However, the reported PCE of bilayer OPV cells is still significantly lower than that of inorganic based PV cells. One reason for this is the intrinsically short exciton diffusion length of excitons in organic semiconductors, which are typically around 10-20nm.<sup>4,5,6</sup> Researchers attempted to overcome this limitation in the bilayer OPV cell by using buckminsterfullerene,  $C_{60}$  in which the exciton diffusion length is around 20nm. P. Peumans *et al.* replaced perylene tetracarboxylic derivative with  $C_{60}$  as an acceptor in the device structure and the device produced 3.5% PCE.<sup>7</sup> This improvement of PCE is attributed to the longer travel distance of excitons in the triplet state of  $C_{60}$ . However, since donor and acceptor layers are around 40-60nm thickness, most of the absorbed photon energy is not efficiently converted to free carriers and dissipated by



recombination, which indicates that photogenerated excitons are dissociated only near the interface between donor and acceptor.

Other approaches to building bilayer OPV cells use conjugated polymers. Sariciftci *et al.* fabricated the first bilayer OPV cell that used a conjugated polymer where the hole transporting material was MEH-PPV and the electron transporting material was C<sub>60</sub>. In this structure, MEH-PPV plays a role in both absorbing photons and transporting holes to an anode, and C<sub>60</sub> transports electrons to a cathode.<sup>8</sup> In this OPV cell, the obtained PCE was 0.04% under monochromatic incident light at 514.5nm, and the performance was only slightly improved compared to single polymer layer PV cells. Halls *et al.* optimized the thickness of conjugated polymer and C60 layer and achieved 9% quantum efficiency under 0.25 mW/cm<sup>2</sup> intensity.<sup>4</sup>

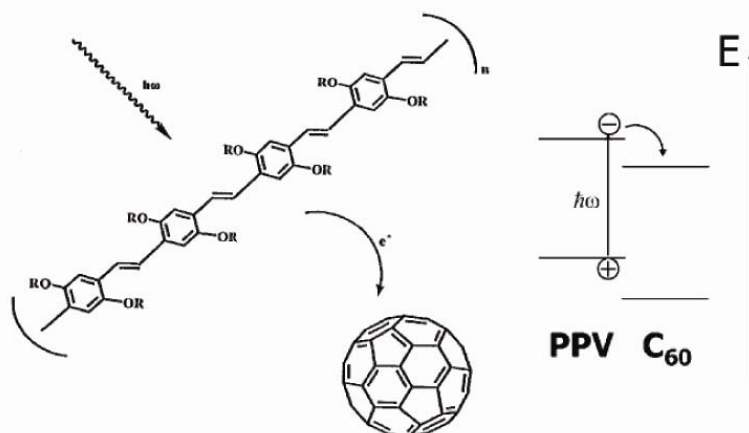


**Figure 2.2.** Photoinduced Charge Transfer from Conjugated Polymer, PPV, to C<sub>60</sub>.

### 2.2.3 Bulk Heterojunction OPV Cells

On the point that bilayer OPV cells collect very small amounts of excitons created near the interface of donor and acceptor, bulk heterojunction OPV cells, which have an intermixed composite of donor and acceptor, have an advantage in terms of their having a much larger interface area between donor and acceptor. (Figure 2.1c) and (Figure 2.3b, c))

For the first time, Yu *et al.* investigated a phase-separated polymer blend composite made of poly[2-methoxy-5-(2'-ethyl-hexyloxy)-1,4-phenylene vinylene], MEH-PPV, as a donor and cyano-PPV, CN-PPV, as an acceptor.<sup>9</sup> The photo-

luminescence and electroluminescence of both component polymers was quenched in the blend, which is indicative of rapid and efficient separation of photogenerated electron-hole pairs with electrons on the acceptor and holes on the donor. Diodes made with such composite semiconducting polymers as the photosensitive medium show promising photovoltaic characteristics with energy conversion efficiency of 0.9%, which is 20 times larger than that of diodes made with pure MEH-PPV.

After discovering the conjugated polymer blend OPV cell, Yu *et al.* also reported improved PCE from the conjugated polymer and C<sub>60</sub>-based bulk heterojunction OPV cell. Composite films of MEH-PPV and fullerenes exhibited PCE of about 2.9%, which is better by more than two orders of magnitude than what has been achieved with devices made with pure MEH-PPV.<sup>10</sup> The efficient charge separation results from photoinduced electron transfer from MEH-PPV (as donor) to C<sub>60</sub> (as acceptor) at the large interface, and the high collection efficiency results from a bicontinuous network of internal donor-acceptor heterojunctions.

The next significant improvement in PCE of blend OPV cells was achieved using poly (3-hexylthiophene) (P3HT) as a hole transporting polymer. Gang Li *et al.* fabricated a blend OPV cell using P3HT and PCBM, soluble C<sub>60</sub> derivative. The significant improvement in PCE results mainly from the crystallinity of P3HT.<sup>11</sup> After casting P3HT and PCBM blend solutions on PEDOT:PSS/ITO, the blend film morphology was controlled by varying the evaporation rate. During the solvent annealing, P3HT and PCBM formed a well-mixed, interdigitated blend film where P3HT forms fibril-like crystalline morphology and PCBM aggregates are embedded. (Figure 2.3 b, c) This phase separated morphology of blend layers enhances the hole mobility of the conjugated polymer, and also improves the absorption efficiency from the fibril-like P3HT aggregates. The best performance from the optimized blend OPV cell was 4.4%.

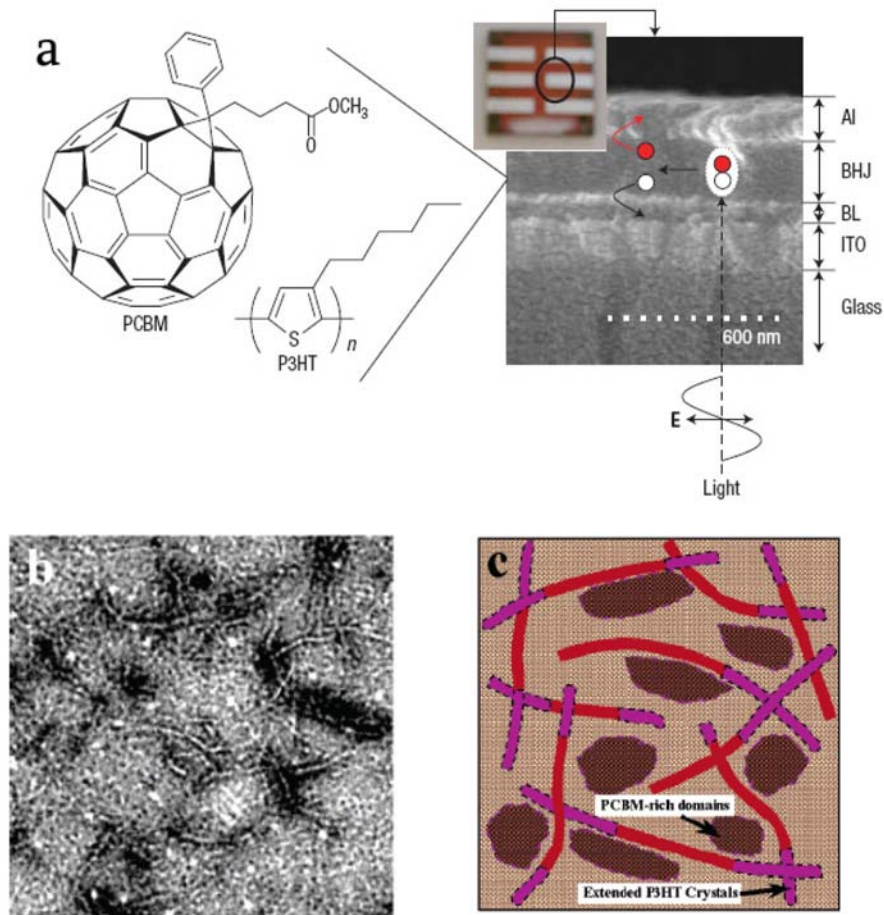


**Figure 2.3.** Morphology of P3HT and PCBM blend OPV Cell: a) Molecular structures of P3HT and PCBM and device cross section of OPV cell<sup>12</sup>; b) TEM image of blend composite of P3HT and PCBM; c) Schematic diagram of phase separated blend of P3HT and PCBM.<sup>13</sup>

Y. Kim *et al.* also investigated a similar blend OPV structure focused on the regioregularity of P3HT.<sup>12</sup> They prepared various P3HT and PCBM blend solutions in which P3HT had different regioregularities ranging from 80% to 96%. The fabricated devices were thermally annealed to induce phase separation of P3HT and PCBM. The investigation revealed that a higher order of regioregularity of P3HT helps to form the crystallized fibril-like shape of P3HT, which improves charge transport as well as light absorption efficiency.

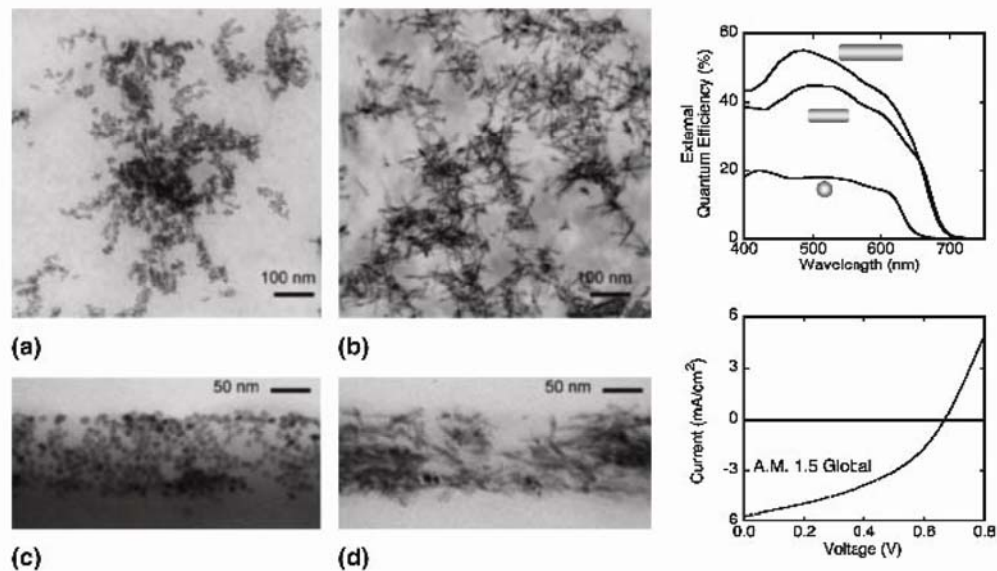


**Figure 2.4.** Morphology of CdSe and P3HT blend and Device Performance: a) morphology of CdSe quantum dots and P3HT; b) Morphology of quantum rod and P3HT; c) ; d) Cross section TEM images of a) and b).<sup>14</sup>

To create a hybrid blend OPV cell, inorganic nanoparticles instead of PCBM or C60 were also blended with conjugated polymers. The initial work was conducted using CdSe nanoparticles with P3HT. The advantage of this system is that the photo physical property and charge transports can be tuned by designing the structure of the acceptor. For example, as the size of CdSe nanoparticles increases, the bandgap decreases, which means that the absorption band of the acceptor shifts to a longer wavelength range.<sup>14</sup> This unique tunability of photophysical properties can be utilized to enhance absorption efficiency of PV cells, because a conjugated polymer absorbs usually only between 350nm to 650nm, which only absorbs partial UV and visual light wave ranges of the solar spectrum. The second merit of the hybrid blend OPV cell is the tunability of electrical charge transport. The electrons, after light absorption and charge dissociation, are transported to a cathode in two ways: internal transport inside a molecule, and electron hopping from one molecule to another. For example, in the case that an acceptor has a rod shape instead of spherical shaped quantum dots, the chance of internal charge transport along the rod increases due to the dimensionality.

## 2.3 Device Physics of the OPV Cell

### 2.3.1 General Working Principle

In OPV cells, the photovoltaic process of converting light to electricity is composed of four consecutive steps.<sup>15</sup>

$$\eta_{eff} = \eta_{abs} \times \eta_{diss} \times \eta_{trans} \times \eta_{col}$$

$\eta_{abs}$  : light absorption efficiency

$\eta_{diss.}$ : exciton dissociation efficiency

$\eta_{trans}$  : charge transport efficiency

$\eta_{col}$  : charge collection efficiency

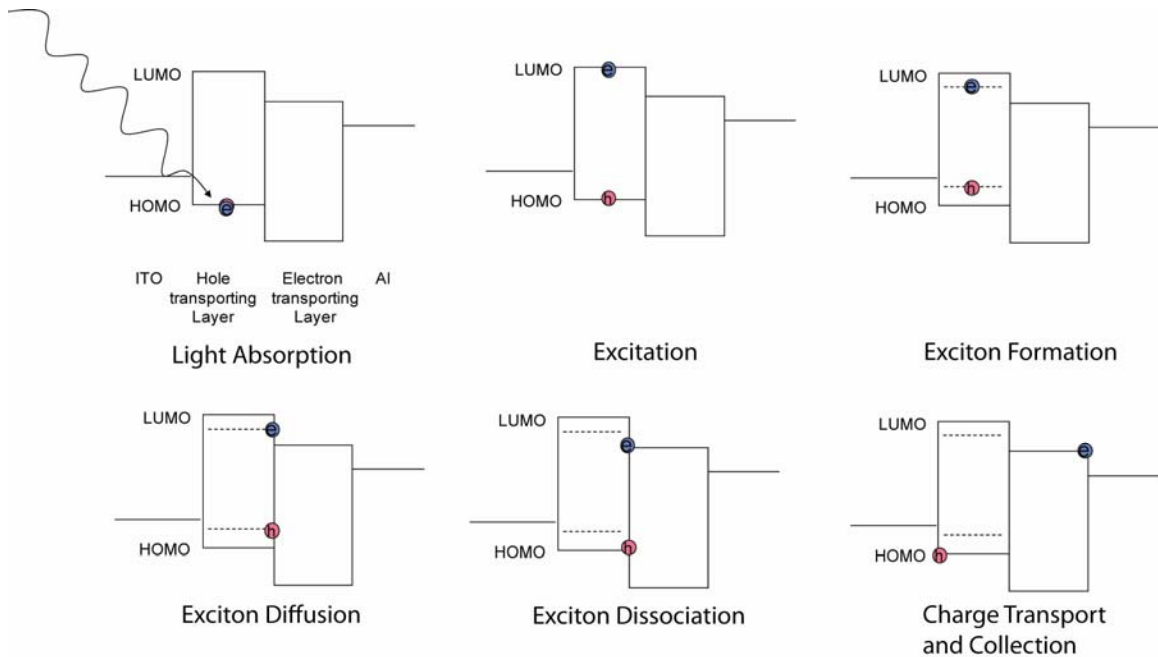


**Figure 2.5.** Device Working Principle from Light Absorption to Charge Collection.

The first step is light absorption leading to exciton formation. When sunlight is directed onto photosensitive semiconducting organics, electrons in HOMO are excited to LUMO. After light absorption, inorganic semiconductors immediately produce free carriers, while organic semiconductors require additional processes to produce free

carriers. First, organic semiconductors form excitons, which are strongly bound electron-hole pairs, that then diffuse inside of the organic semiconductor, which is independent on an applied electric field. The typical exciton diffusion length in an organic semiconductor is around 10-20nm, and exciton dissociation occurs only at the interface between the donor and the acceptor due to the offset of HOMO states of the donor and the acceptor.<sup>16</sup> If excitons do not reach the interface, they recombine and the absorbed energy is dissipated without generating photocurrent. Therefore, to efficiently generate power, the excitons have to be dissociated and collected at electrodes before recombination. The performance of an OPV cell is characterized by a J-V curve, as seen in figure 2.6a, below.

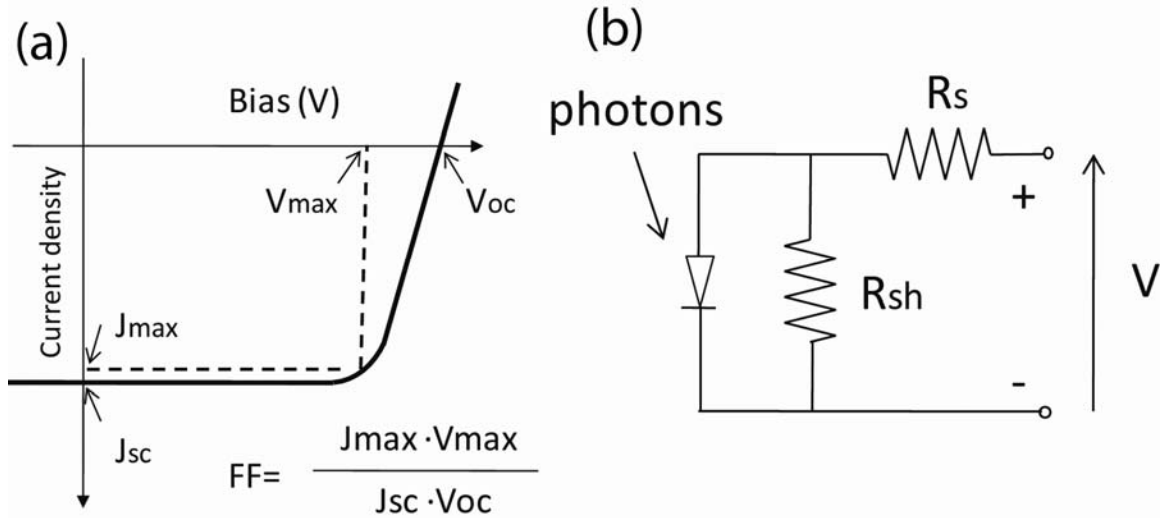


**Figure 2.6.** a) The definition of fill factor (FF),  $J_{max}$ : current density at the maximum of  $J \times V$  in 4<sup>th</sup> quadrant,  $V_{max}$ : bias at the maximum of  $J \times V$  in 4<sup>th</sup> Quadrant; b) Circuit of photovoltaic device,  $R_s$ : series resistance,  $R_{sh}$ : shunt resistance.

The general current density and voltage characteristic under illumination are shown in figure 2.6a. and a electrical circuit of photovoltaic device is depicted in figure 2.6b. Under dark conditions, there is no current at the short circuit condition. Under an illumination condition, the incident photons generate current and the minus current density in the 4<sup>th</sup> quadrant of J-V curve indicates this photogenerated current.

Parameters such as short circuit current ( $J_{sc}$ ), open circuit voltage ( $V_{oc}$ ), fill factor (FF), and power conversion efficiency (PCE) are used to quantitatively analyze the performance of PV cells. For an ideal diode, the dark current density  $J_{dark}(V)$  is

$$J_{dark}(V) = J_o (e^{qV/k_B T} - 1) \quad (1)$$

Where  $J_o$  is a constant,  $k_B$  is Boltzmann's constant and T is temperature in degrees Kelvin.

The overall current voltage response of the cell can be approximated as the sum of the short circuit photocurrent and the dark current. Although the reverse current, which flows in response to voltage in an illuminated cell, is not formally equal to the current that flows in the dark, the approximation is reasonable for many photovoltaic materials. The sign convention for current and voltage in photovoltaics is that the photocurrent is negative. With this sign convention, the net current density in the cell is

$$J(V) = J_{dark}(V) - J_{sc}, \quad (2)$$

which becomes, for an ideal diode,

$$J(V) = J_o (e^{qV/k_B T} - 1) - J_{sc}. \quad (3)$$

When the contacts are isolated, the potential difference has its maximum value, the open circuit voltage  $V_{oc}$ . This is equivalent to the condition when the dark current and short circuit photocurrent exactly cancel out. For the ideal diode,

$$V_{oc} = \frac{kT}{q} \ln\left(\frac{J_{sc}}{J_o} + 1\right). \quad (4)$$

Equation (4) shows that  $V_{oc}$  increases logarithmically with light intensity.

Figure **2.6a** shows that the current-voltage product is negative and the cell generates power when the voltage is between 0 and  $V_{oc}$ . At  $V < 0$ , the illuminated device acts as a photodetector, consuming power to generate a photocurrent that is light dependent but bias independent. At  $V > V_{oc}$ , the device again consumes power. This is the region where light emitting diodes operate.

The fill factor (FF) is calculated as

$$FF = \frac{J_m V_m}{J_{sc} V_{oc}} \quad (5)$$

to denote the part of the product of  $V_{oc}$  and  $J_{sc}$  that can be used. With this, the power conversion efficiency can be written as

$$Power = \frac{P_{OUT}}{P_{IN}} = \frac{J_{MAX} V_{MAX}}{P_{IN}} = \frac{FF J_{sc} V_{oc}}{P_{IN}}. \quad (6)$$

When we consider parasitic resistances such as series resistance ( $R_s$ ) and shunt resistance ( $R_{sh}$ ), equation (3) is modified as follows

$$J(V) = J_o(e^{qV/k_B T} - 1) + \frac{V - JAR_s}{R_{sh}} - J_{sc} \quad (7)$$

In the real cell, power is dissipated through the resistance of the contacts and through leakage currents. These effects are equivalent electrically to two parasitic resistances in series ( $R_s$ ) and in parallel ( $R_{sh}$ ) (Figure 2b). The series resistance arises from the resistance of the cell material to current flow, particularly through the front surface to the contacts. The parallel or shunt resistance arises from leakage of current through the cell. Since series and shunt resistances reduce fill factor, smaller  $R_s$  and larger  $R_{sh}$  are required in order to fabricate an efficient PV cell.

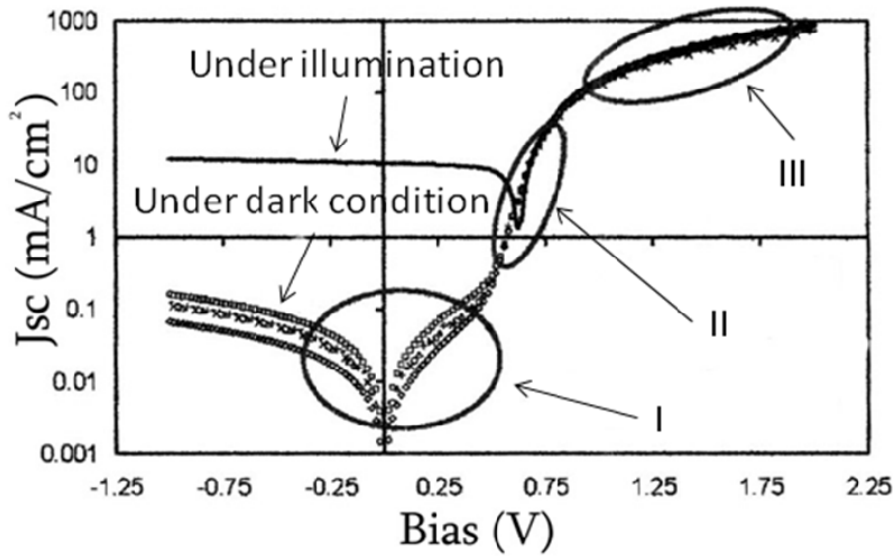


**Figure 2.7.** J-V curves under dark condition and illumination. Y axis is log scale.<sup>17</sup>

The derived equation (7) includes comprehensive elements to explain the J-V curve of a PV cell. The Y axis in Figure 2.7 is plotted in log scale and the J-V curve has three regions that can be correlated with  $R_{sh}$  (region I), exponential behavior of pn junction (region II), and  $R_s$  (region III):

- I. A linear regime at negative voltages and low positive voltages where the current is limited mainly by  $R_{sh}$



- II. An exponential behavior at intermediate positive voltages where the current is controlled by the diode
- III. A second linear regime at high voltages where the current is limited by the  $R_s$ .

### 2.3.2 Device Physics of Organic Blend PV Cells

The organic blend cell reported the best performance 3 to 5%.<sup>11,12</sup> However, since the active blend layer of P3HT and PCBM has interdigitated morphology, a comprehensive equation describing the working principle of a blend OPV cell is necessary.

Recently, Waldauf *et al.* developed a three dimensionally ‘expanded pn junction’ model to describe the behavior of the organic blend PV cell.<sup>17</sup> In this investigation, MDMO-PPV/PCBM or P3HT/PCBM blend systems were used to produce experimental data. In addition, the equations in the model, which are based on equation (3) introduced in chapter 2.3.1, which analytically describe the behavior of the organic blend PV cell, was further developed by applying the characteristics of organic blend PV cells. Then the equations were confirmed by fitting the data to them.

Before directly discussing an equation that includes the complicated structure of blend layer morphology, we can consider a flat bilayer organic PV cell as a simple organic pn junction. In this bilayer device, charges are generated at the interface of donor and acceptor by dissociating excitons. Then, holes and electrons are transported to electrodes through donor and acceptor layers. This basic structure can be applied to organic blend layers by considering the blend system as many tiny pn junctions that are three dimensionally interconnected.

On this basis, equations for blend OPV cell can be specified further from equation (7).

$$J(V) = J_o (e^{qV/k_B T} - 1) + \frac{V - JAR_s}{R_{sh}} - J_{sc} \quad (8)$$

The characteristic pn junction has an exponential relation of current and bias over a certain bias. The parameter that affects the exponential part of the JV-characteristic is

the saturation current ( $J_o$ ), which reflects the number of charges able to overcome the energetic barrier in the reverse direction. It represents the charge density in the vicinity of the barrier. In classical pn functions, the charge density consists of a temperature independent intrinsic part reflecting the purity of the materials  $J_i$  and a thermally activated part. The latter shows an exponential dependence on the temperature T and the height of the respective energetic barrier, i.e., the difference in the internal chemical potentials. Mathematically obtained values of  $\Phi$  from MDMO-PPV/PCBM and P3HT and PCBM have been well matched with experimentally obtained values of  $E_{LUMO}-E_{HOMO}$ .

$$J_o = J_i e^{q\phi / nkT} \quad (9)$$

Next, light generated current density ( $J_{sc}$ ) can be explained in detail by considering the charge generation rate,  $G$ . In this derivation, this model requires the following assumptions:

- I. Blend layer has a large interface area between donor and acceptor, which enhances charge dissociation efficiency
- II. After exciton formation, charge dissociation is more dominant than recombination
- III. After charge dissociation, charges can recombine at the interface during transport, which is a loss of generated charge.

Under illumination, light is absorbed and charges are generated throughout the blend layer. The generation rate  $G$ , representing the number of charges generated inside a device of area  $A$  per second, is then given by the number of photons absorbed per second, which is a function of the incident photon flux  $\Phi_{photon}$ . This gives the number of incident photons per second and area, the absorption coefficient  $\alpha$ , the thickness  $d$  of the layer, and the probability for the separation  $\nu_{cs}$  of the generated excitons into free charge carriers:

$$G = \nu_{CS} \Phi_{photon} A(1 - e^{-\alpha d}).$$

For simplicity the generated charges within the volume of the blend layer can be transformed to an average amount of generated charges per volume per second  $g=G/V=\nu_{CS} \Phi_{photon} A(1 - e^{-\alpha d})/d$ . To contribute to an external current, the generated charges must

be extracted before recombination. The probability for charge carriers within a volume  $V$  in distance  $l$  from the electrode being extracted is determined by the time scale for the recombination, i.e., the charge carrier lifetime  $\tau$ , and the maximum distance a charge can travel prior to the recombination, which is given by  $l_{max} = \tau \mu E_i = \tau \mu (V - V_{bi})/d$ . Here,  $\mu$  is the charge mobility and  $E_i$  is the internal potential, which is set by the applied voltage  $V_{appl}$  and the built-in potential  $V_{bi}$ , i.e., the difference between the acceptor LUMO and the donor HOMO. This implies two regions for the light generated current density  $J_{sc}$ . For  $d < l_{max}$ , all light generated charge carriers are extracted and  $J_{sc}$  is given by

$$J_{sc} = \text{sgn}(V_{appl} - V_{bi}) v_{CS} \Phi_{photon} A(1 - e^{-\alpha d}) q \quad \text{for } d < | l_{max} | .$$

For  $d > l_{max}$ , only the charge carriers that are within a distance of  $l_{max}$  of the electrodes can be extracted. Therefore  $J_{sc}$  is described by

$$J_{sc} = \frac{l_{max}}{d} (V_{appl} - V_{bi}) v_{CS} \Phi_{photon} A(1 - e^{-\alpha d}) q$$

$$= \frac{\tau \mu (V_{appl} - V_{bi})}{d^2} v_{CS} \Phi_{photon} A(1 - e^{-\alpha d}) q \quad \text{for } d > | l_{max} | .$$

In the expanded  $pn$ -junction model, exciton dissociation takes place at a well-defined interface between the donor and the acceptor material, and charge transport occurs via channels of pure phases. The predictions of the model for the temperature dependence of the dark current, built-in potential, and light-generated photoconductivity are experimentally verified on various donors combined with PCBM in blend OPV devices, including polythiophenes, polyphenylenes, and polyfluorenes. The close correlation of the experimental results with the predictions of the model supports the validity of the expanded  $pn$ -junction picture. The expanded  $pn$  junction provides a better description of the physics of organic bulkheterojunction photovoltaic cells than the MIM model used until now. However, the expanded  $pn$  junction model does not describe the loss mechanism during charge transport and needs to be improved.

## 2.4 Strategies to Improve OPV Cell Performance

In chapter 2.3.1 the general working principles of OPV cells were discussed. These include light absorption, exciton dissociation, charge transport, and charge collection.<sup>15</sup> Using strategies to maximize each step, the performance enhancement of an OPV cell can be effectively achieved. For example, light absorption can be improved by bandgap tuning of organic semiconductors or stacking multiple PV cells, i.e., tandem cell, where each stacked cell absorbs different regions of the solar spectrum. Exciton dissociation can be improved by increasing the interface area between donor and acceptor. Finally, the charge mobility in organic semiconductors affects charge transport efficiency.

### 2.4.1 Bandgap Tuning and Tandem Cells

The bandgap tuning of semiconducting organics and the fabrication of tandem cell structure can effectively enhance absorption efficiency. Considering that conventional conjugated polymers absorb sun light in the visual wavelength range from 350 to 650nm, photon energy in near IR regions of sunlight, where more photon flux is found, is dissipated by transmitting the photosensitive layer without exciton generation. Therefore, black dye absorbing broader wavelength range is a promising candidate to enhance absorption efficiency. One of the most promising strategies to realize absorption enhancement was a new material synthesis of low bandgap conjugated polymer using electron donor and electron acceptor repeating units.<sup>18,19</sup> The absorption spectrum of the low bandgap conjugated polymer is shown in Figure 2.8d.

However, two problems arise when low bandgap conjugated polymer is used for the OPV cell.<sup>19</sup> One problem is the unavoidable reduction of the open-circuit voltage ( $V_{oc}$ ) compared with high-bandgap polymers. This occurs because the  $V_{oc}$  is related to the energy difference between the lowest unoccupied molecular orbital (LUMO) of the electron acceptor and the highest occupied molecular orbital (HOMO) of the electron donor as equation (9) shows clearly in chapter 2.3.2. The other challenge is to have a large enough driving force for electron transfer from the polymer to the electron acceptor. This means that the LUMO of the electron donor must be closer in energy to vacuum than the LUMO of the electron acceptor in order to have enough driving force for exciton dissociation at the interface of the electron donor and acceptor. When decreasing the

bandgap of a polymer, both the LUMO level and the HOMO level are affected. The LUMO position of the polymers might be shifted away from the vacuum level so much that the use of new electron acceptors with lower LUMO levels than the commonly used PCBM is needed for preparing an efficient solar cell.

Another strategy for enhancing the absorption efficiency of OPV cells is the building of a tandem cell.<sup>20, 21</sup> Since each conjugated polymer has a unique bandgap, broad sunlight cannot be harvested efficiently by a single polymer. Therefore, double layers or triple layers of stacked tandem cell structures in OPV cells, of which each layer absorbs a different light wave range, can resolve the limited absorption problem of a single device. (Fig 2.8e, f) However, to fabricate a well-performing tandem cell, challenging technical issues should be carefully considered. For example, the interfacial electrode layer located between the front and back cells could be an issue. The interfacial electrode layer should be able to collect electrons from the front cell, transmit light, which will be absorbed in the back cell, and collect holes from the back cell. When electron and hole collection is not balanced at the interfacial electrode layer, charges accumulate and this lowers the performance of the OPV cell. In reality, fabricated tandem cells suffer from interfacial layer problems, and significantly improved performance with tandem cells has not been reported, although each front cell and back cell showed good photovoltaic performance.

Recently, using tandem cell structure, K. Lee *et al.* successfully demonstrated improved performance of an OPV cell with 6.5% PCE.<sup>22</sup> In the blend layers, semiconducting polymers and fullerene derivatives consisted of photoactive layers. A transparent titanium oxide (TiO<sub>x</sub>) layer was used as an interfacial electrode that separates and connects the front cell and the back cell. The TiO<sub>x</sub> layer served as an electron transport and collecting layer for the first cell and as a stable foundation that enabled the fabrication of the second cell to complete the tandem cell architecture.

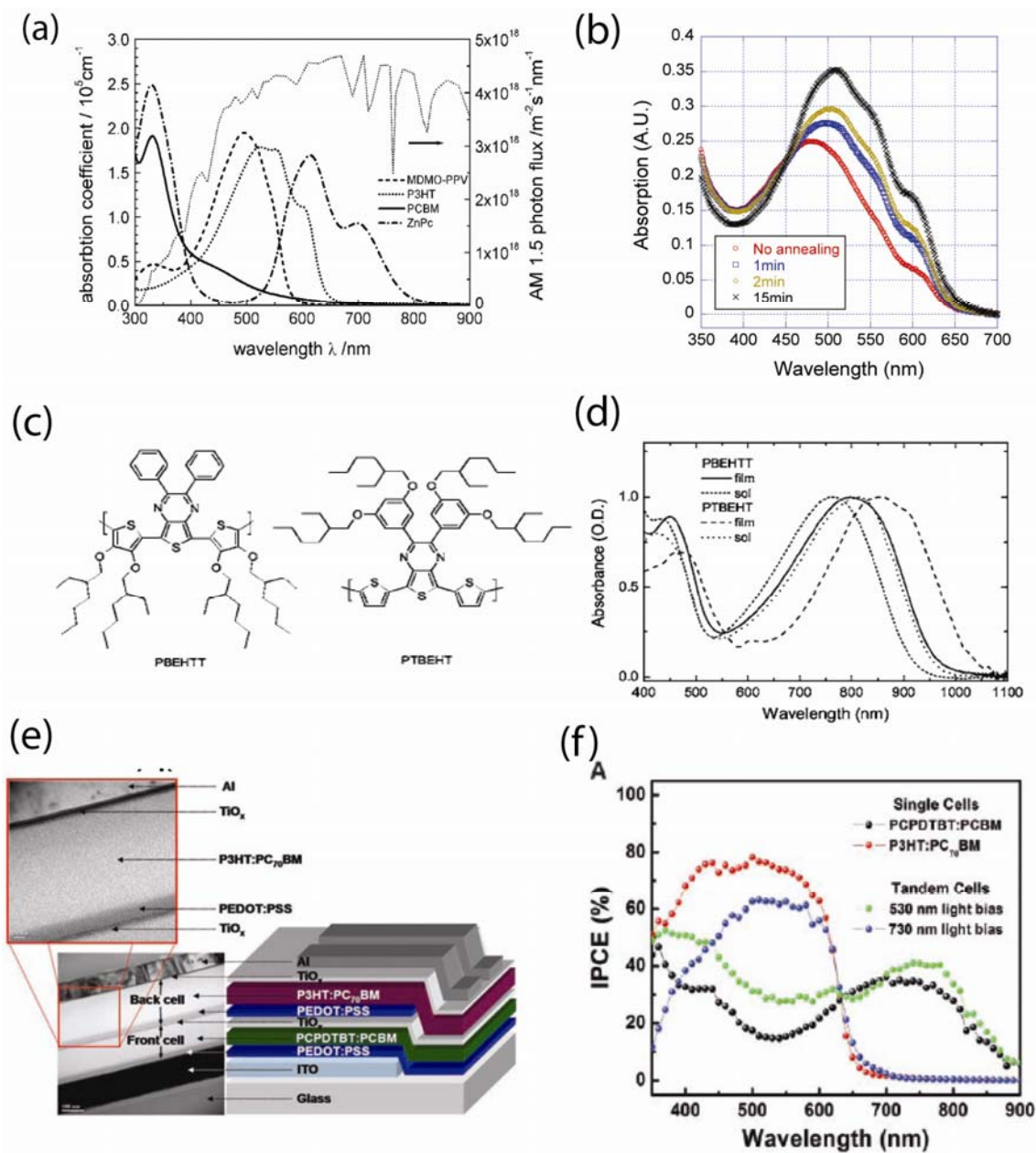


**Figure 2.8.** The Absorption Characteristics of Conjugated Polymers: a) Absorption spectra of organic semiconductors with solar spectrum<sup>23</sup>; b) Absorption evolution of P3HT during annealing; c) Chemical structure of IR absorbing conjugated polymers; d) Absorption spectra of IR absorbing conjugated polymers<sup>18</sup>; e) Tandem cell using conjugated polymer and fullerene derivative blend cells; and f) Incident photon conversion efficiency of tandem cell.<sup>22</sup>

Another way to improve absorption efficiency is through better intermolecular packing, which can change the chromophore properties of conjugated polymers by forming intermolecular aggregation.<sup>24</sup> As an example, regioregular P3HT has excellent intermolecular packing because there are two moieties promoting the intermolecular packing: hexyl group side group and thiophene ring in the backbone. Spincoated polymer film is solidified and dried very rapidly and the cast polymers are kinetically frozen before stabilizing molecular packing. The annealing process supplies energy into the kinetically frozen film and reforms molecular packing. (Figure **2.8b**) During annealing, the maximum absorption peak of P3HT increases and the maximum absorption wavelength  $\lambda$  shifts to a longer wavelength due to the intermolecular ground state aggregation, resulting in absorption efficiency enhancement.

#### **2.4.2 Nanostructured PV Cell**

After observing the photovoltaic response from the single layer OPV cell, the first significant PCE improvement of the OPV cell was achieved by fabricating a donor and acceptor bilayer OPV cell. The interface between the donor and acceptor has an offset of HOMO and LUMO states, which dissociates excitons. To achieve further improvement of OPV cell performance, this concept was enhanced by building intermolecularly blended OPV cells with very large interfaces of donor and acceptors in molecular scale. The resulting performance of the blend OPV cell was 3-5%, which is 2-3 times better than the bilayer OPV cell. However, the bottleneck of the blend OPV cell is that its randomly interdigitated blend layer holes and electrons travel long distances before reaching an electrode. This may increase charge recombination chance. In addition, the blend layer has a discontinuous island structure in matrix so that generated charges in the islands cannot be collected at an electrode, resulting in dissipation of absorbed light energy.

The nanostructured OPV cell was designed to overcome the charge recombination problem of the blend OPV cell, and maintain efficient exciton dissociation.<sup>25, 26</sup> To build an excellently performing nanostructured OPV cell, the design principles of nanostructured OPV cells should be addressed. First, the patterned structure should be able to maximize exciton dissociation. Since excitons travel 5 to 20nm, a 10 to 40nm

period pattern can be expected to efficiently dissociate excitons. Second, the height of the pattern should be tuned to absorb enough photons without losing charges by recombination. For example, 200nm thick P3HT absorbs over 90% of incident light at the maximum absorption peak wave length, and in this case, the pattern height should be around 200nm thick. If the film is thicker than 200nm, the film absorbs almost 100% of incident photon but some portion of generated charges may recombine due to longer travel distance. Thicker film has a higher series resistance and lower shunt resistance as well. If the film is thinner than 200nm, the photoactive layer absorbs fewer than 90% of photon charges, but the lower series resistance and higher shunt resistance of the device are beneficial. The overall performance of the OPV cell will be determined by both combinational effects. Third, the morphology of the capping layer covering the nanostructured pattern may have importance. When the capping layer is evaporated onto the nanostructured pattern, the vacuum-deposited layer should cover the patterned bottom layer conformally. When conformal coating is achieved, the interface of donor and acceptor layers is able to form a continuous pn junction. Another issue is the topography of the deposited layer between the cathode and acceptor. (Figure 2.9) If the top topography has grooves, light absorption can be enhanced due to the refraction of light in the patterned photoactive layer, which results in a longer travel distance of incident light. When the refractive indices of semiconducting layers are different, the grooved pattern changes light travel direction inside the organic layers. To create a grooved coating of the capping layer, spincoating can be used. This is because a grooved topography can originate from the nanostructured bottom layer when the top layer is spincoated on a patterned nanostructure with a proper process condition. In addition, the deposited cathode layer on top of the grooved pattern of the capping layer has the same pattern transferred from the bottom layer, and this may induce additional light scattering in the PV device because of the reflection of the metal cathode.



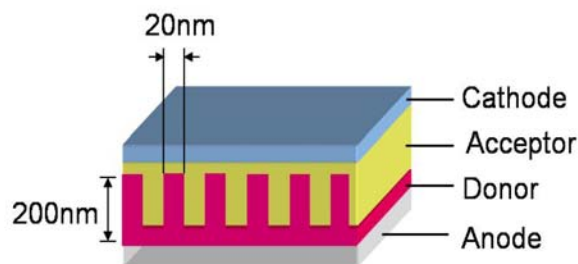


**Figure 2.9.** Nanostructured OPV Cell Structure

Various nanostructured OPV cells have been realized using diverse approaches. In chapters 5 and 6, OPV cells that were patterned using nanoimprint lithography, as well as the performance improvement that resulted from this pattern, will be discussed in detail.

McGehee *et al.* fabricated nanostructured OPV cells using a nanostructured perfluoropolyether (PFPE) template, which was replicated from a nanopatterned silicon master mold. Anatase titania nanostructures with post-like features ranging from 30 to 100 nm in height and 30 to 65 nm in spacing were fabricated using the Pattern Replication in Nonwetting Templates (PRINT) process.<sup>27</sup> P3HT layers, with or without Z907 dye, were cast on the nanostructured TiO<sub>2</sub>. Finally, Ag cathode was evaporated to complete cell fabrication. Z907, one of the dyes, was coated to enhance light absorption in the OPV cell.

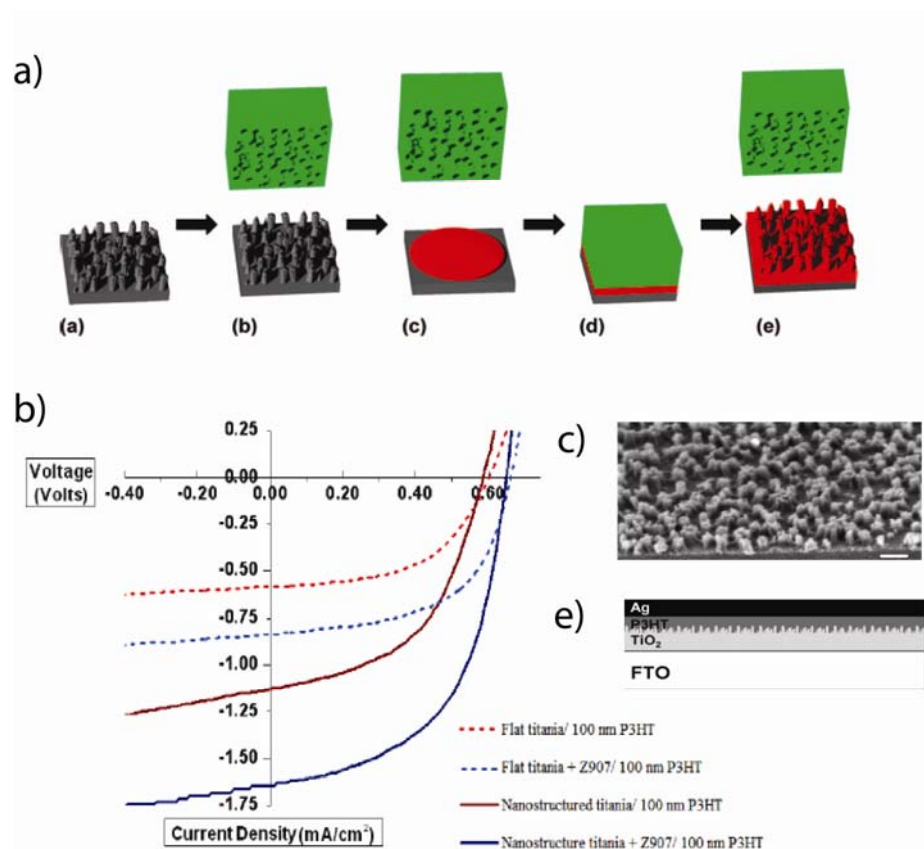


**Figure 2.10.** Nanostructured OPV Cell Using PRINT Process: a) Nanopattern fabrication process using porous PFPE template; b) JV curves from  $\text{TiO}_2$  and conjugated polymer PV cells having different interface structure; c) Imprinted  $\text{TiO}_2$  precursor; and d) Cross section of fabricated OPV cell having nanopatterned interface.<sup>27</sup>

Compared with flat devices, the nanopatterned OPV cells showed two to three-fold increased performance, which results from the increased interface area between donor and acceptor. The patterned OPV with Z907 dye also showed improved PCE compared with the patterned OPV cells without Z907, and this improvement is attributed to the enhanced absorption from dye.

As another approach, nanostructured OPV cells based on small molecule organic semiconductors was fabricated using organic vapor phase deposition (OVPD) by F. Yang *et al.*<sup>28</sup> This approach yielded a two to three-fold fold increase in PCE compared with flat control devices. The needle shaped CuPc was grown by varying temperature, pressure and carrier gas flow in the deposition chamber, and the grown donor surface area was increased. **(Figure 2.11c)** In the nanostructured OPV cell fabrication using small molecule organic semiconductors, the uniform and conformal deposition of the acceptor

layer onto the nanostructured donor layer is a challenging step, because conventional thermal evaporation cannot deposit the acceptor layer conformably because of the shadow effect from the needle shaped CuPc. Compared with vacuum thermal evaporation, OVPD has large molecular surface diffusivity. Therefore, this method enabled conformal coating of the acceptor on the nanostructured donor, and a well-performing nanostructured OPV cell was fabricated.

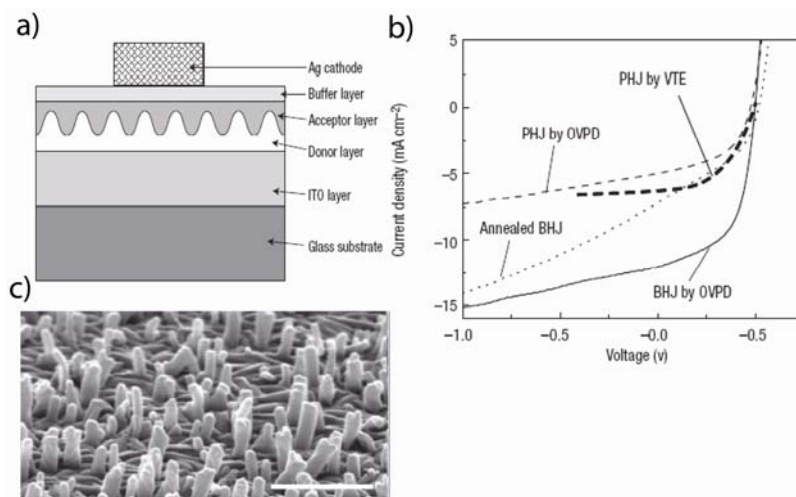


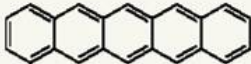
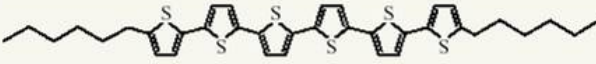
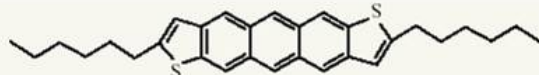
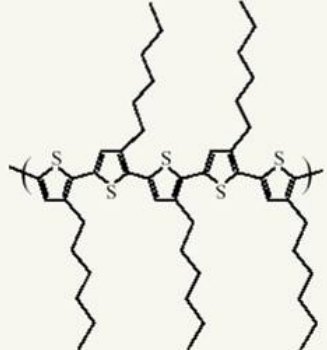
**Figure 2.11.** CuPc and PTCBI-based Nanostructured OPV Cell: a) Schematic device structure; b) JV curves from bilayer OPV cell and nanostructured OPV cell; and c) Nanostructured CuPc morphology.<sup>28</sup> Scale bar: 500nm.

However, until now, significant PCE improvement by fabricating nanostructured OPV cells has not been reported. The nanostructured OPV cell improved the performance 2 to 3 times compared with flat OPV cells. However, in some cases, the performance of the flat cell is much lower than the blend OPV; therefore, overall performance improvement of nanostructured OPV cells was not significant. Because nanostructured OPV cells were proposed to overcome the limitations of blend OPV cells, an explanation for the limited improvement of nanostructured OPV cells should be considered. Several issues may limit improvement of nanostructured OPV cells. Poor electrical properties, such as lower mobility of semiconductors originating from nanopatterned structures, might be one important issue. During patterning, the semiconducting layer is deformed and there is no guarantee of high performance electrical properties. The mobility of semiconductors has a huge impact in the device performance, but there is no established method to measure the mobility of only protruded or engraved regions in the

nanopatterned structure. Other issues include questions about whether excitons are efficiently dissociated or if the dissociated charges recombine at pn junction in the vertical direction. Achieving a well-performing nanostructured OPV cell is very challenging. Furthermore, it might be even more challenging to clearly address how nanostructured OPV cells are fabricated and resolving all possible fabrication problems.

### **2.4.3 High Mobility Semiconducting Organics**

When the performance of silicon PV cells is correlated with mobility, the mobility issue becomes a critical factor for determining PCE. Silicon PV cells can be categorized into a-Si PV cells,  $\mu$ c-Si PV cells, and single crystalline PV cells, depending on the morphology of the silicon layer. An a-Si PV cell has an amorphous phase silicon layer with a hydrogen dangling bond, and this amorphous structure does not have a lattice. A single crystalline silicon PV cell has a single, perfect crystalline structure and the whole layer is comprised of units of lattice without defects. The characteristic of the morphology of  $\mu$ c-Si is that crystalline silicon domain and grain boundary. The silicon crystalline domains are distributed in the matrix. Depending on crystalline growth conditions, morphology and electrical properties can be controlled. When other processing and fabrication parameters are optimized, the highest PCE from an a-Si PV cell is around 12%, and PCE from single crystalline PV cell is 24%. This shows a good match with the mobility trend. The mobility of single crystalline is over  $600\text{cm}^2/\text{V}\cdot\text{s}$ , while the mobility of a-Si is around  $0.1\sim 1\text{cm}^2/\text{V}\cdot\text{s}$ .

Semiconductor	Representative chemical structure	Mobility ( $\text{cm}^2\text{V}^{-1}\text{s}^{-1}$ )
Silicon	Silicon crystal	300–900
	Polysilicon	50–100
	Amorphous silicon	~1
Pentacene		~1
$\alpha,\omega$ -dihexylsexithiophene		$10^{-1}$
$\alpha,\omega$ -dihexylanthradithiophene		$10^{-1}$
Regioregular poly(3-hexylthiophene)		$10^{-1}$
Organic-inorganic hybrid	Phenethylamine-tin iodide	~1

**Figure 2.12.** Hole Mobilities of Organic Semiconductors.

The mobility of organic semiconductors provides an important indication about the possibility to improve performance. Gang Li *et al.* achieved 4.4% PCE from P3HT and PCBM blend OPV cells, and investigated hole and electron mobility in the device.<sup>11</sup> The morphology of the OPV cell was controlled by solvent annealing using dichlorobenzene. When the active blend layer was phase separated, the hole mobility ( $\mu_h$ ) of P3HT was  $5.5 \times 10^{-5} \text{ cm}^2/\text{V}\cdot\text{s}$  and the electron mobility ( $\mu_e$ ) of PCBM was  $7.7 \times 10^{-5} \text{ cm}^2/\text{V}\cdot\text{s}$ . Since both mobilities are in a similar range, the charges were not confined in the device and charge transport was balanced to the electrode. However, since the best mobility of self-organized P3HT is around  $0.1 \text{ cm}^2/\text{V}\cdot\text{s}$  which is a huge gap compared to  $10^{-5} \text{ cm}^2/\text{V}\cdot\text{s}$  in the blend OPV cell, we can expect enhanced performance of an OPV cell by improving the mobility of semiconducting organics. To improve the mobility of

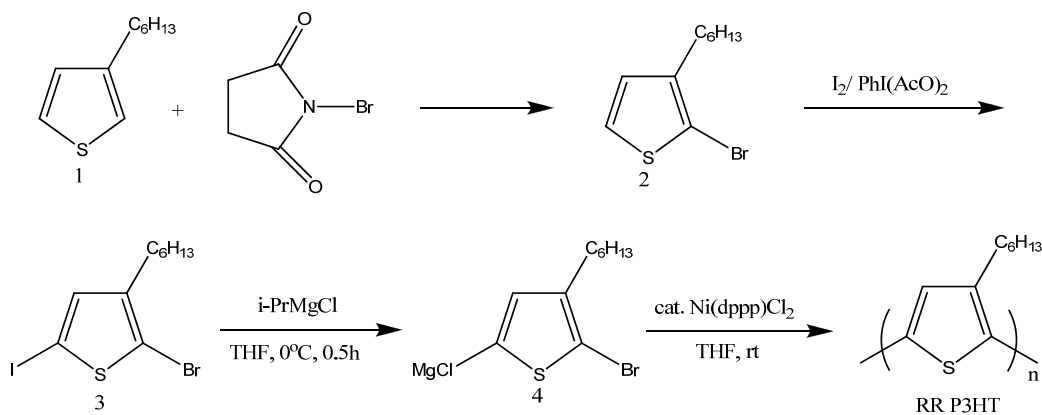
organic semiconductors, novel material design and morphology control are promising strategies.

## 2.5 General Experimental Materials and Methods

The following sections summarize the materials and fabrication processes used in the thesis work.

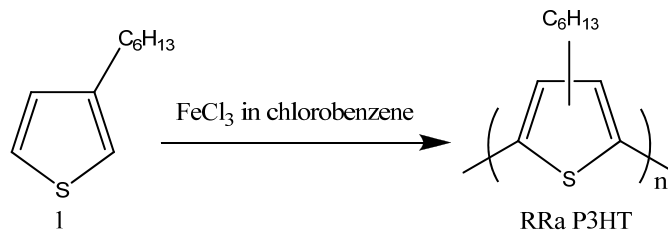
### 2.5.1 General Materials

#### Regioregular P3HT



**1** was reacted with 1 equiv of NBS in THF at 0 °C for 1 hour. Then **3** was synthesized by reaction of **2** with 1.1 equiv of iodobenzene diacetate at room temperature. Treatment of 2-bromo-3-hexyl-5-iodothiophene (**3**) with 1 equiv of isopropylmagnesium chloride at 0 °C gave **4** via magnesium-iodine exchange. The addition of 0.4 mol % of Ni(dppp)Cl<sub>2</sub> (dppp = 1,3-bis-(diphenylphosphino)propane) to the reaction mixture and stirring at room temperature led to RR P3HT.

#### Regiorandom P3HT



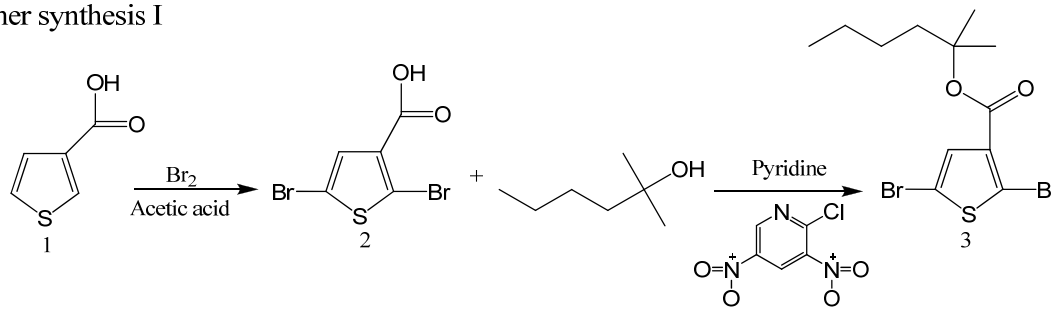
1g of 3-hexylthiophene was reacted with 3.99g of FeCl<sub>3</sub> in chlorobenzene. Since FeCl<sub>3</sub> was not completely dissolved in chlorobenzene, when the mixture was transferred to the reactor, careful handling was required. The polymerization was done for 2 hours at

room temperature, and then the polymers were dedoped with the mixture of hydrazine and water for 24 hours.

Thermally Deprotectable Thiophene Derivative (TDPTD)

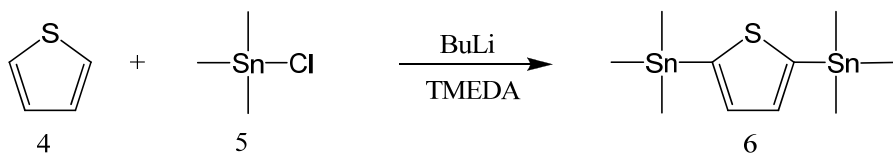
TDPTD was polymerized by reacting two monomers of **3** and **6**.

Monomer synthesis I



**2** was synthesized by bromination of **1**. Br was added drop by drop at room temperature, and the mixture with **1** was reacted at 60° C for 8 hrs. The esterification of **2** was carried out using 2-chloro-3,5-dinitropyridine as a condensing agent. 2-chloro-3,5-dinitropyridine (21 mmol) was added to a mixture of 2,5-dibromo-3-thiophenecarboxylic acid (21 mmol) and 2-methyl-2-hexanol (27.5 mmol) in pyridine and kept under a nitrogen atmosphere. The mixture was stirred at 115° C for 30 min, and then cooled to room temperature. The solution was then poured into 6% aqueous NaHCO<sub>3</sub> and extracted twice with petroleum ether.

Monomer synthesis II

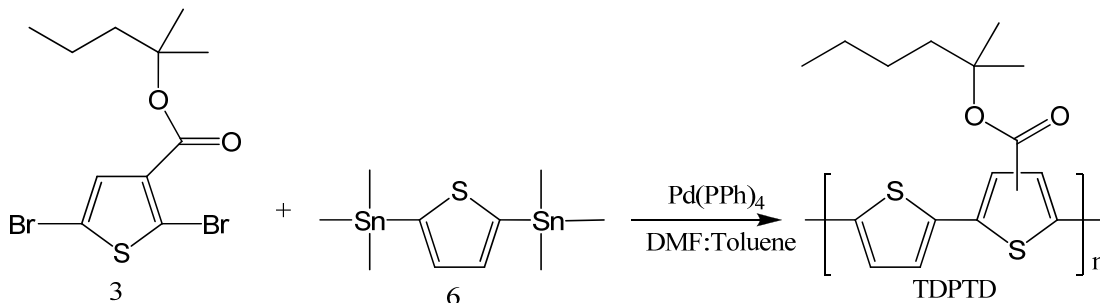


To a 250 mL three-neck flask, thiophene (37.5 mmol) and tetramethylethylene diamine (75 mmol) were added under N<sub>2</sub>. Following addition of butyl lithium 2.5 M solution in hexane, the mixture was brought to reflux for 30 min, leading to the formation of a white precipitate. The mixture was then cooled to -70°C and trimethyltin chloride (75 mL 1 M solution in THF, 75 mmol) was added over a period of 5 min. The cooling bath was then removed, and the reaction was allowed to proceed at room temperature for 12 hrs. The



solution was then poured into 200 mL water and extracted with ether. The combined organic layers were then dried over anhydrous  $\text{MgSO}_4$ . After filtration and removal of the solvent, the crude solid was recrystallized from ethanol.

### Polymerization



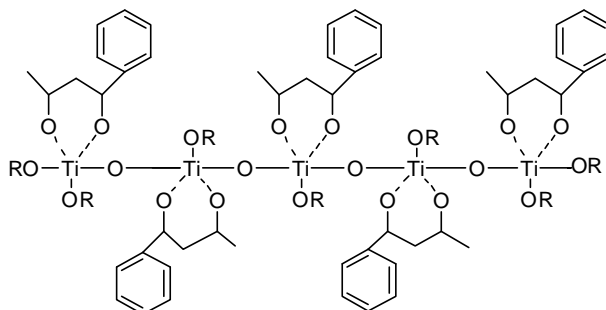
A mixture of 2-methyl-2-hexyl-2,5-dibromothiophene-3-carboxylate (1.00 g, 2.6 mmol) and 2,5-di(trimethyltin)thiophene (1.07 g, 2.6 mmol) was prepared in a 100 mL 3-neck flask, and  $\text{Pd}(\text{PPh}_3)_4$  (0.16 g) was then added. DMF (7 mL) and toluene (30 mL) were added via syringe. The mixture was heated to 120° C for 12 hrs, then allowed to cool to room temperature and poured into 300 mL of methanol to precipitate the polymer.

### Titania Precursor

An n-type  $\text{TiO}_2$  precursor was used for patterned  $\text{TiO}_2$  based organic photovoltaic cell fabrication discussed in chapter 7. The material was provided by Dr. Ho-Cheol Kim's group at IBM Almaden Research Center.

To form a n-type anatase  $\text{TiO}_2$ , we used a commercially available organic titanate as the precursor of titania. N-butyl polytitanate,  $n\text{-C}_4\text{H}_9\text{O}-[\text{Ti}(\text{O}-n\text{-C}_4\text{H}_9)_2\text{O}]_n\text{-n-C}_4\text{H}_9$  with molecular weight of  $\sim 1250$  g/mol, was used in this study. We reacted 6.25 g of n-butyl polytitanate (Tyzor® BTP, DuPont, Wilmington, Delaware) with 4.46 g of benzoylacetone (BzAc, Aldrich) to synthesize a chelated precursor. The chelated precursor was dissolved in propylene glycol propyl ether (PGPE) to make a 30 wt% solution.

To obtain an anatase structure, the spincast precursor film was calcined at 450° C for 1 hr. During calcination, the organic functional groups at the precursor were burned out.



## 2.5.2 General Processing Techniques

### Spin Casting

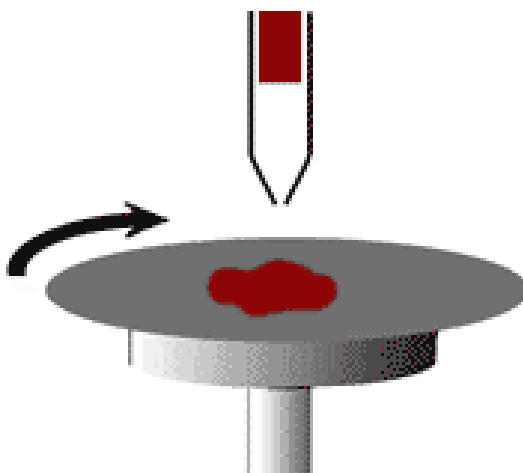


**Figure 2.13.** Scheme of Spin Coating Process.

Spin coating is a simple and precise method that uses centrifugal force to produce a uniform thin film ranging from 20 to 300nm in thickness. The variables in spin casting process are solvent concentration, spin speed, and spin time. By varying solution concentration and spin speed, the film thickness can be easily controlled. For organic PV cell fabrication, organic semiconductors require 100 to 200nm film thickness. Spin time is determined by drying the wet film. During spincasting, volatile solvent is evaporated and typical spin time is 30 sec to 1 min.

Nanoimprint Lithography (NIL)

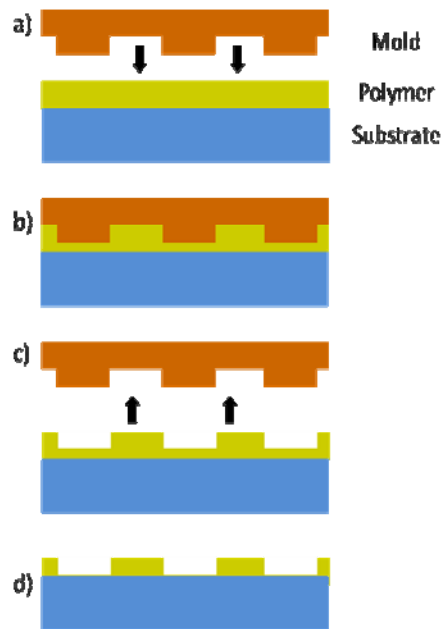


**Figure 2.14.** Nanoimprint Lithography Process Scheme: a) and; b) Imprinting; c) Demolding; and d) Anisotropic etching.

Nanoimprint lithography is a novel method to fabricate nanometer scale patterns. It is a simple process with low cost, high throughput, and high resolution.<sup>29</sup> It creates patterns by mechanical deformation of imprint resist and subsequent processes. The imprint resist is typically a monomer or polymer formulation that is cured by heat or UV light during the imprinting. Adhesion between the resist and the template is controlled to allow proper release.

The principle of pattern transfer using nanoimprint lithography is simple. First, a master mold having a pattern is required. The mold is placed on the polymer resist thin film, which is spincoated on a substrate. Then, the assembled elements are heated over the glass transition temperature of the polymer. Finally, pressure is applied to the sample in order to deform the polymer resist. After demolding, the residual layer can be removed using the etching process.

## Vacuum Evaporation

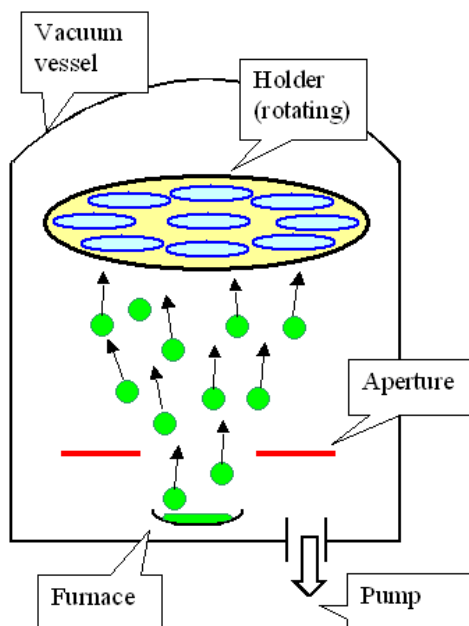


**Figure 2.15.** Diagram of Vacuum Evaporator.

Thermal evaporation is a method to deposit thin film of metal or small molecule organic semiconductors. The variables to control the metal evaporation are vacuum chamber pressure, source material purity, and evaporation power, which is correlated with the evaporation rate. The pressure of the vacuum chamber should be maintained around  $5 \times 10^{-7}$  torr to ensure good quality deposition. When the deposition is conducted at pressure higher than  $1 \times 10^{-6}$  torr without reaching low enough pressure, hot vaporized metal particles react with remaining oxygen molecules and form metal oxide. Deposited layers with this condition lose metallic reflection and electrical properties. For high quality thin film, material purity over 99.99% is essential. High purity source material lowers the chance of side reactions or impurity formation during evaporation. The evaporation rate ranges from  $1 \text{ \AA} / \text{sec}$  to  $3 \text{ \AA} / \text{sec}$  in most investigations in the article. Source materials should be evaporated slowly to protect the sub-layer, which can be damaged by hot vapors.

## 2.6 References

1. R. N. Marks *et al.*, *J. Phys.: Condens. Matter* **6**, 1379 (1994).
2. M. Knupfer, *Appl. Phys. A: Mater. Sci. & Proc.* **77**, 623-626 (2003).
3. C. W. Tang, *Appl. Phys. Lett.* **48**, 183 (1986).
4. J. M. Halls *et al.*, *Appl. Phys. Lett.* **68**, 3120 (1996).
5. L. S. Roman L.A.A. Patterson, and O. J. Inganas *J. Appl. Phys.* **86**, 487 (1999).
6. M. Theander *et al.*, *O. Phys. Rev.* **61**, 12957 (2000).
7. Aharon Yakimov Peter Peumans and Stephen R. Forrest, *J. Appl. Phys.* **93**, 3693 (2003).
8. N.D. Sacriciftci, *Appl. Phys. Lett.* **62**, 585 (1993).
9. G. Yu and A. J. Heeger, *J. Appl. Phys.* **78**, 4510 (1995).
10. J. J. M. Halls *et al.*, *Nature* **376** (498) (1995).
11. Gang Li *et al.*, *Nature Materials* **4**, 864 (2005).
12. Y. Kim *et al.*, *Nature Materials* **5**, 197 (2006).
13. X. Yang *et al.*, *Nanoletters* **5**, 579 (2005).
14. J. J. Dittmer W. U. Huynh, and A. P. Alivisatos, *Science* **295**, 2425 (2002).
15. Stephen R. Forrest, *MRS bulletin* **30**, 28 (2005).
16. P. Heremans V. I. Arkhipov, and H. Bassler, *Appl. Phys. Lett.* **82**, 4605 (2003).
17. C. Waldauf *et al.*, *J. APP. PHYS.* **99**, 104503 (2006).
18. F. Zhang *et al.*, *Adv. Mater.* **18**, 2169 (2006).
19. M. M. Wienk *et al.*, *Appl. Phys. Lett.* **88**, 153511 (2006).
20. G. Dennler *et al.*, *Appl. Phys. Lett.* **89**, 073502 (2006).
21. A. Yakimov and S. R. Forrest, *Appl. Phys. Lett.* **80**, 1667 (2002).
22. J. Y. Kim *et al.*, *Science* **317**, 222 (2007).
23. P. Peumans *et al.*, *J. Mater. Res.* **19**, 7 (2004).
24. J. Kim and T. M. Swager, *Nature* **411**, 1030 (2001).
25. K. M. Coakley and M. D. McGehee, *Chem. Mater.* **16**, 4533 (2004).
26. K. M. Coakley C. Goh, and M. D. McGehee, *Nanoletters* **5**, 1545 (2005).
27. S. S. Williams *et al.*, *Chem. Mater.* **20**, 5229 (2008).
28. F. Yang, *Nature Materials* **4**, 37 (2005).
29. L. J. Guo, *J. Phys. D: Appl. Phys.* **37**, R123 (2004).

## **CHAPTER 3**

### **THE EFFECTS OF PROCESSING PARAMETERS ON THE REPRODUCIBILITY OF ORGANIC PHOTOVOLTAIC CELLS: P3HT AND PCBM BLENDS SYSTEM**

#### **3.1 Introduction**

Over the past decade oil price has risen and this trend is expected to be last for a while due to the heavy energy demand. Furthermore, environmental issues such as the destruction of the ozone layer also became a critical issue as carbon dioxide is the by-product of fossil fuels. Accordingly, the photovoltaic technology has been drawing great attention as a green and potentially free alternative energy source. An organic photovoltaic cell (OPVC) is an emerging new technology having various advantageous potentials such as bandgap tunability, flexible cell design, and easy processability and economic processing cost. To commercialize this technology, there are still unsolved technical limitations of a short life time and a low power conversion efficiency of OPVC. Nevertheless, the potential of OPVC as a promising alternative energy source is still being highly estimated as the encapsulation technology of commercialized OLED can be transferred to OPVC to improve the life time and the power conversion efficiency of OPVC has been steadily increased due to the improved understanding on the device physics and new material development.

The recent trend of OPVC research can be categorized into three areas. First, achieving high power conversion efficiency (PCE) over 10% is the primary objective.<sup>1</sup> In order to achieve high efficiency of the organic photovoltaic cell, light absorption, exciton dissociation, charge transport and charge collection efficiency should be maximized.

$$\eta_{eff} = \eta_{abs} \times \eta_{diss} \times \eta_{trans} \times \eta_{col}$$

$\eta_{abs}$  : the light absorption efficiency

$\eta_{diss}$ : the exciton dissociation efficiency

$\eta_{trans}$  : the charge transport efficiency

$\eta_{col}$  : the charge collection efficiency.

The light absorption efficiency can be improved by the band gap tuning of semiconducting organics, intermolecular packing, and absorption enhancement using surface plasmon.<sup>2,3,4,5</sup> The exciton dissociation efficiency can be improved by creating increased interface area between donor and acceptor.<sup>6</sup> The charge transport efficiency can be enhanced by creating well-organized interdigitated structure of donor and acceptor having well-routed hole and electron pass way. In this process, if a defect exists the charges are accumulated and recombined which lower the charge collection efficiency. The charge collection efficiency is correlated with the charge transport at the interface between a semiconducting organic layer and an electrode.

The second research trend is the optimization of the morphology of the active organic layer. Solar cells based on the P3HT and PCBM blend have kept breaking the highest PCE record through the morphology control of the blend layer. However, the morphology of P3HT and PCBM has not been fully understood because the phase separation of P3HT and PCBM is characterized by AFM but this doesn't provide the detailed and accurate information of the morphology. Recently, there have been several investigations about the morphology of the P3HT and PCBM blend layer. Michels *et al.* clearly showed the fibril-like lamella structure of intra and intermolecularly crystallized P3HT and the aggregation of PCBM in the annealed P3HT/PCBM film by using scanning tunneling microscopy.<sup>7</sup> The concentration gradient of P3HT and PCBM depending on the depth in the blend film was also investigated by means of Raman scattering and ellipsometry.<sup>8</sup> Nevertheless, to achieve more efficient performance from blend OPVC, more thorough understanding on the relationship between the blend morphology and the charge creation and transport should be investigated further.

The accurate characterization of OPVC performance also became one of the important research areas because there are many characterization parameters that can

influence on the device performance such as illumination spectrum mismatch and extra current from the cross shape electrode design.<sup>9,10</sup> The fact that organic semiconducting materials are also known to be sensitive to oxygen and moisture also can cause performance variation. Moreover, because there is skepticism on the reliability and reproducibility of the device performance of OPVC, the accurate and reproducible performance of organic electronic devices should be systematically studied and addressed. In this chapter, the reproducibility and reliable performance of the P3HT and PCBM blend OPVC are systematically investigated. We could achieve highly reproducible and reliable cells by controlling several important fabrication parameters.



### 3.2 Experiment

In this investigation island shape electrode cathode was used in order to exclude the extra charge collection observed in devices having the crossbar type electrode configuration. ITO coated glass was cleaned with acetone and IPA. After drying with air, the substrate was treated with UV ozone for 5min. PEDOT:PSS (Baytron PH 500) was spin cast on the cleaned ITO as received and baked for 15min. at 130°C. P3HT and PCBM solution (1:1 wt %, 20mg/ml in chlorobenzene) was prepared with stirring over 24hrs. in the glove box and spin cast at 1000rpm for 30sec. Then the samples were annealed at 130°C for 15min. 1nm LiF and 100nm Al layers were deposited sequentially under  $5 \times 10^{-7}$  torr. For ITO/PEDOT:PSS/P3HT+PCBM/Al device, first the spincast film of P3HT and PCBM was baked and after Al deposition the samples were thermally annealed again.

The fabricated devices were characterized under ambient condition without encapsulation. The illumination intensity was 100mW/cm<sup>2</sup> (AM 1.5G Oriel solar simulator) and the I-V curves were obtained using HP semiconductor analyzer.

### 3.3 Results and discussion

We systematically investigated the reproducibility of OPVC based on poly (3-hexylthiophene) (P3HT) and [6,6]-phenyl-C<sub>61</sub>-butyric acid methyl ester (PCBM) blend system by carefully controlling fabrication variables. The variables were the preparation method of the blend solution, blend ratio, blend layer thickness, poly(3,4-ethylenedioxythiophene) poly(styrenesulfonate) (PEDOT:PSS) thickness, conductivity of PEDOT:PSS, spin cast condition, cathode structure, annealing condition and method, encapsulation, illumination setup, and characterization setup. After establishing well controlled fabrication and characterization protocols less than 8% of the OPVC performance variation was achieved. This performance variation is comparable to that of silicon based photovoltaic cells.<sup>11,12</sup> The most effective processing variables in order to achieve the less than 8% error range of OPC performance turned out to be P3HT+PCBM film quality, cathode composition, and annealing condition.

#### 3.3.1 Blend layer quality

To achieve highly reproducible performance of OPVC, the film quality of P3HT and PCBM is critical. In a macroscopic point of view, the thin film quality can be examined by visual observation of whether the spin cast film forms homogeneous and uniform film or not (Fig. 3.1(b) inset). Both P3HT and PCBM have functional side groups to give solubility in organic solvent. However, the solubility of them is different from a solvent to another. Therefore, the blend solution should be carefully prepared to produce uniform film. Figure 3.1 shows J-V curves with optical microscopy images of the spin cast film from 1:1 wt % of P3HT and PCBM solution in chlorobenzene solvent (a) before and (b) after filtering through HTFE filter. The big particles in Figure 3.1(a) inset are the aggregates of organic semiconductors due to their limited solubility. The obtained J-V curves from the unfiltered solution showed inconsistent performances as shown in Fig. 3.1(a). Mainly the fill factor (FF) and the short circuit current density ( $J_{sc}$ ) fluctuated and resulting overall power conversion efficiency varied from 0.001% to 2%. The aggregates of organic semiconductor are believed to cause charge accumulate and/or charge trapping. (Fig. 3.2). After the filtration of the blend solution, the fabricated

OPVCs showed consistent and reproducible J-V curves as shown in Figure 3.1(b). All devices were fabricated on an ITO substrate.

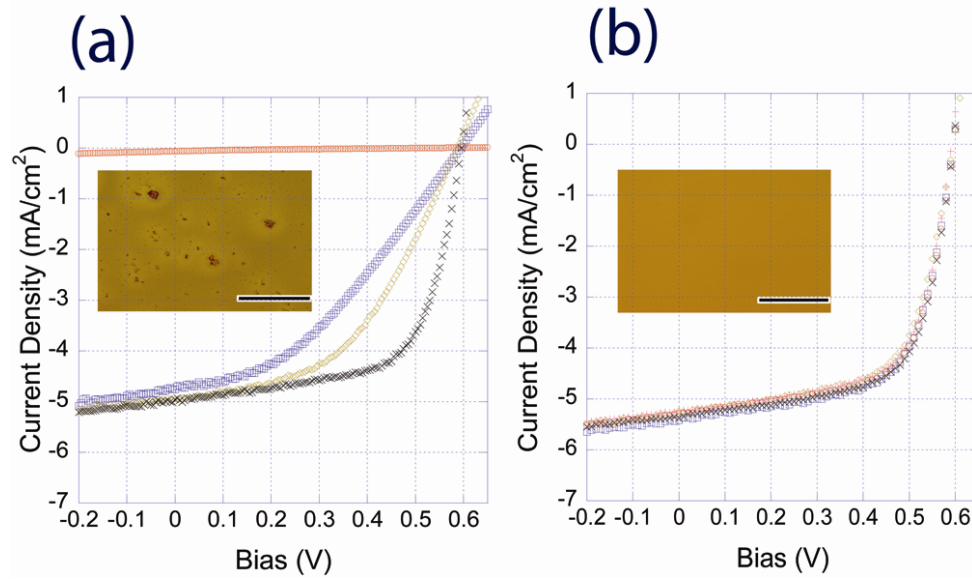


**Figure 3.1.** J-V curves with optical microscopy images of the spincast P3HT and PCBM blend solution (a) before and (b) after filtering. Scale bar: 5 $\mu$  meter.

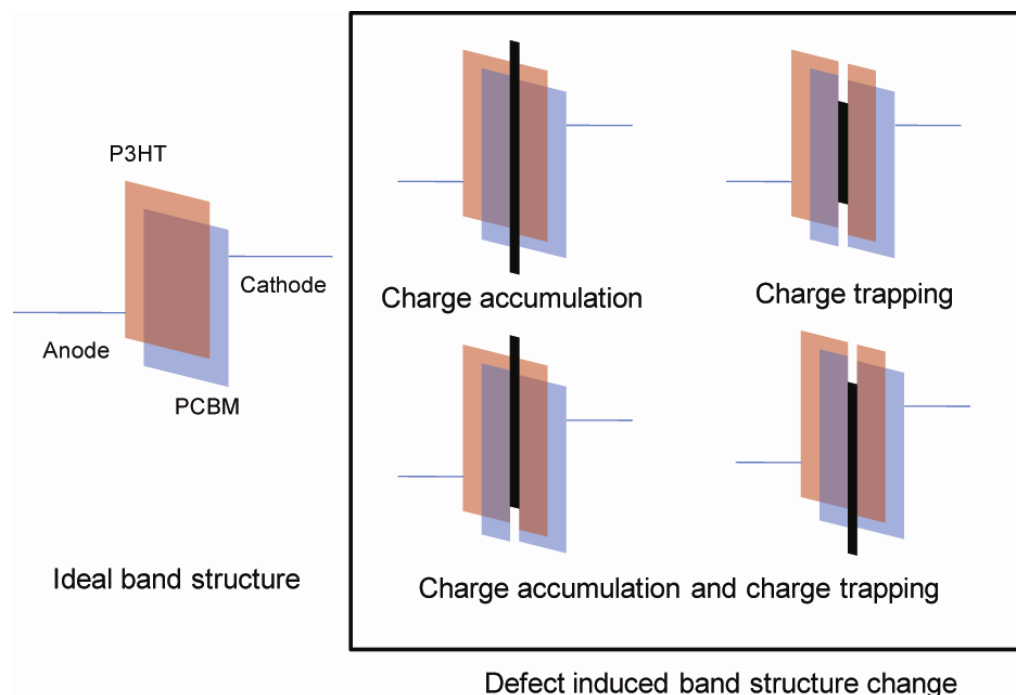


**Figure 3.2.** Schematic band diagrams having charge trapping and accumulation by aggregate impurities. Black bars in the band diagram indicate possible barrier or trap by the aggregates of P3HT and PCBM.

### 3.3.2 LiF as an interlayer between blend layer and cathode

Another important variable to achieve the highly reproducible performance of OPVC is the cathode composition. We fabricated two kinds of devices having different cathode composition: Device I having Al cathode (ITO/ PEDOT:PSS/ P3HT+PCBM/ Al) and Device II having LiF(1nm)/Al cathode (ITO/ PEDOT: PSS/ P3HT+PCBM/ LiF/ Al). When a series of Device I are fabricated in one batch all J-V curves showed excellent consistency. However, when those are fabricated in different batches the J-V curves showed very large variation on the performance depending on annealing condition and device size (diameter=2mm, 3.5mm, and 5mm) (Fig. 3.3 and Fig. 3.4(a)).  $V_{oc}$  and  $J_{sc}$  changed from 0.4V to 0.6V and from  $1\text{mA}/\text{cm}^2$  to  $5.5\text{mA}/\text{cm}^2$ , respectively, and FF was less than 0.5.

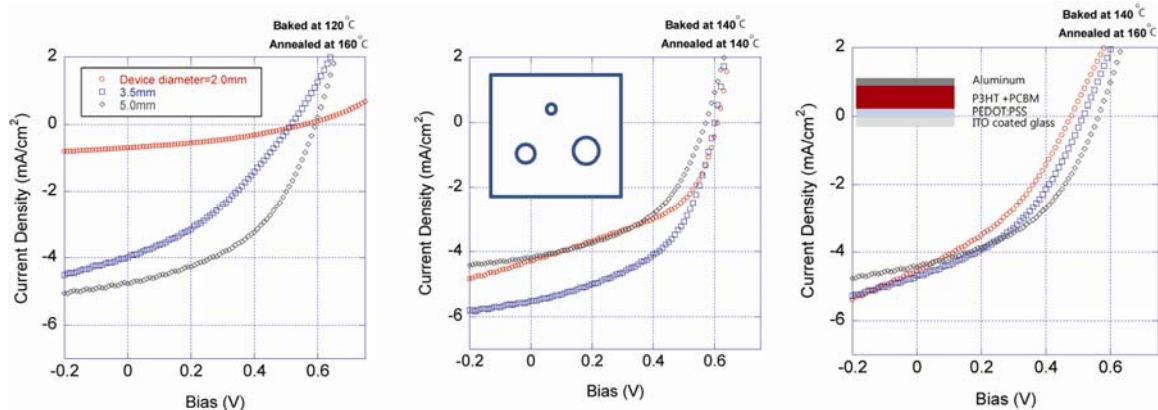


**Figure 3.3.** J-V curves of ITO/ PEDOT:PSS/ P3HT+PCBM/ Al devices. The Device I was heat treated after P3HT and PCBM (baking) casting and after Al deposition (annealing), respectively. Baking and annealing temperatures are listed in each figure.

However, when 1nm LiF was deposited between the P3HT/PCBM layer and the Al cathode, devices showed greatly improved reproducible performances (Fig. 3.4(b)). Each curve was obtained from different batches. The characterized error range of the power conversion efficiency of the cells is less than 8% due to the minor fluctuation of  $J_{sc}$  from 5.3 to 6.0 mA/cm<sup>2</sup>. The P3HT/PCBM layer was spincoated in a glove box but the devices were exposed to atmosphere while the samples were transferred to an evaporator for the electrode deposition and the characterization. This may delicately affect the film thickness or morphology. The slight performance variation can be attributed to this brief air exposure during device fabrication. However, the  $V_{oc}$  and the fill factor remained as a constant without noticeable change. The effects of oxygen and moisture on the organic device performance will be discussed later.

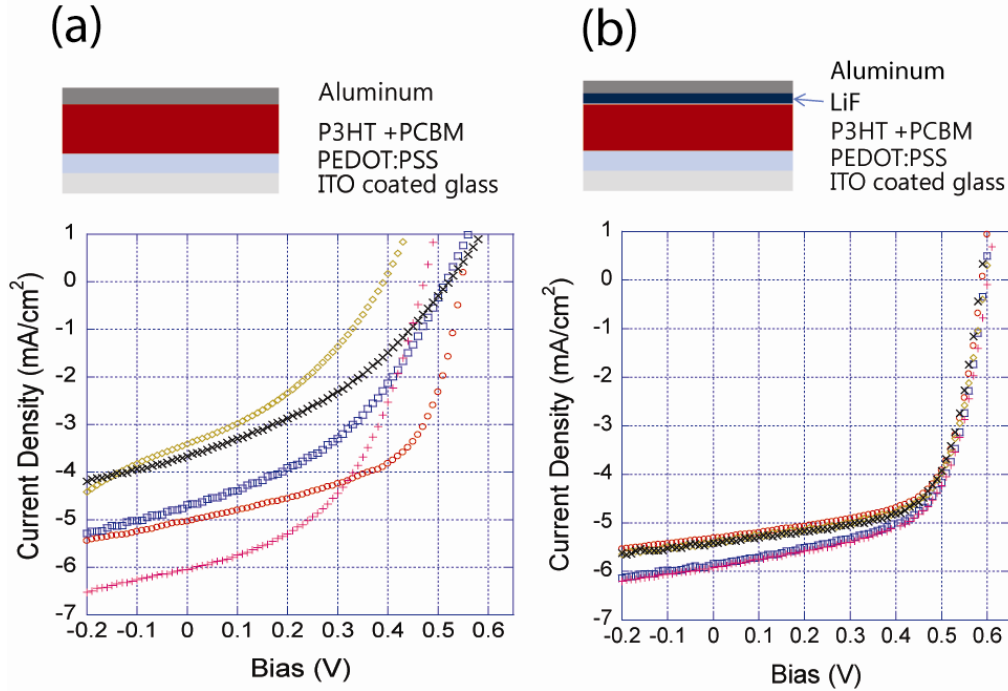


**Figure 3.4.** J-V curves from OPVC w/o LiF layer (a) and w/ LiF layer (b).

Therefore, additional layer of LiF dramatically improves the reliability and reproducibility of the OPVC. There have been hypotheses about the roles of LiF leading enhanced organic electronic device performance. First, LiF forms ohmic contact to the semiconducting organic layer by lowering the work function of Al.<sup>13</sup> In the organic light emitting diode electron injection efficiency was enhanced by adding thin LiF layer between the organic semiconducting layer (OSL) and the cathode. However, since, in the OPVC, electrons generated in the P3HT and PCBM layer need to be extracted from the blend layer to the cathode this hypothesis cannot directly explain the enhancement of the OPVC performance.

Second, thin LiF layer protects the semiconducting organic layer from the direct deposition of hot Al vapor and prevent damages. Sariciftci *et al.* systematically proved that this hypothesis is not valid by inserting SiO<sub>2</sub> or LiF thin layer between the blend layer (MDMO-PPV + PCBM) and the aluminum cathode.<sup>14</sup> If the role of LiF is the only protection of the semiconducting organic layer, a thin SiO<sub>2</sub> layer had to show the same performance enhancement. However, the enhanced Voc and FF were not observed.

The last and most reasonable hypothesis is that a thin LiF layer forms oriented dipoles at the interface of the semiconducting organic layer and the cathode and this

oriented dipole improves the electron extraction.  $\text{Li}^+$  ions are oriented towards semiconducting organic layer and  $\text{F}^-$  ions are oriented towards metal preferentially. The  $\text{Li}^+$  has very strong electron affinity so this induces efficient electron extraction from the semiconducting organic layer to  $\text{Li}^+$  ions. We believe this hypothesis can explain the highly reproducible performance of OPVC as well. The poor reproducibility in the Device I w/o LiF can be explained by accumulation or recombination of charges at the interface or defects between the semiconducting organic layer and Al or combination of these. This is correlated with the charge collection efficiency of OPVC.

### **3.3.3 Minor effect of oxidation on reproducible performance of OPV cell**

The oxygen and moisture sensitivity was investigated as another important variable on the reproducible performance of OPVC since organic semiconducting materials are known to be sensitive to oxygen and moisture. The fabricated OPVC was not encapsulated and the device performance was characterized under continuous AM 1.5G illumination condition at ambient atmosphere for 1hr. In the obtained J-V curves, FF and  $V_{oc}$  changes are negligible and  $J_{sc}$  also decreases about only 10% after continuous 1hr illumination (Fig. 5). Since each cell characterization requires less than 1 min. the effect of degradation of organic semiconductor during the device characterization can be neglected as a critical factor causing significant performance variation. When the device was exposed to ambient atmosphere w/o encapsulation for 24hrs, the  $J_{sc}$  decreased from  $5.5 \text{ mA/cm}^2$  down to  $0.1 \text{ mA/cm}^2$  and the FF decrease was also very drastic but the  $V_{oc}$  decreased slightly from 0.6V to 0.58V.

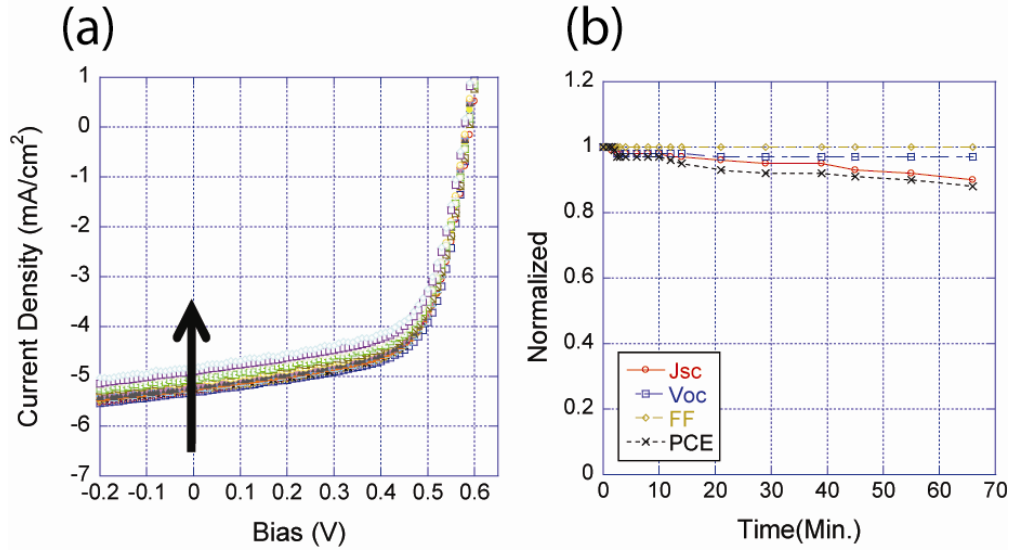


**Figure 3.5.** The degradation of OPVC w/o encapsulation for 1 hour under atmosphere and continuous (AM 1.5G) 100mW/cm<sup>2</sup> intensity light illumination (a) J-V curve change (b) device degradation.

The main degradation mechanism of P3HT and PCBM blend cells is the oxidation of semiconducting organics. The P3HT degradation by oxygen yields C=O, C=S=O and C–O– bonds which break the  $\pi$ -conjugation of the P3HT backbone.<sup>15</sup> And C<sub>60</sub> degradation is facilitated by the diffusion of O<sub>2</sub> into C<sub>60</sub> layer. This induces the O<sub>2</sub><sup>+</sup> – C<sub>60</sub><sup>-</sup> dipole formation between O<sub>2</sub> and C<sub>60</sub> molecules and the dipole defects are known to increase the recombination chance of excitons in OPVC.<sup>16,17</sup>

### 3.3.4 Excellent reproducible performance of OPV cell through optimization

After optimizing the above mentioned critical variables, the reproducibility of OPVC performance was investigated using four methods. In all experiments, all devices (ITO/PEDOT:PSS/P3HT+PCBM/LiF/Al) had the island electrode geometry in order to eliminate the extra charge collection observed in the devices having the crossbar type electrode and their PCE was around 2%.<sup>10</sup>



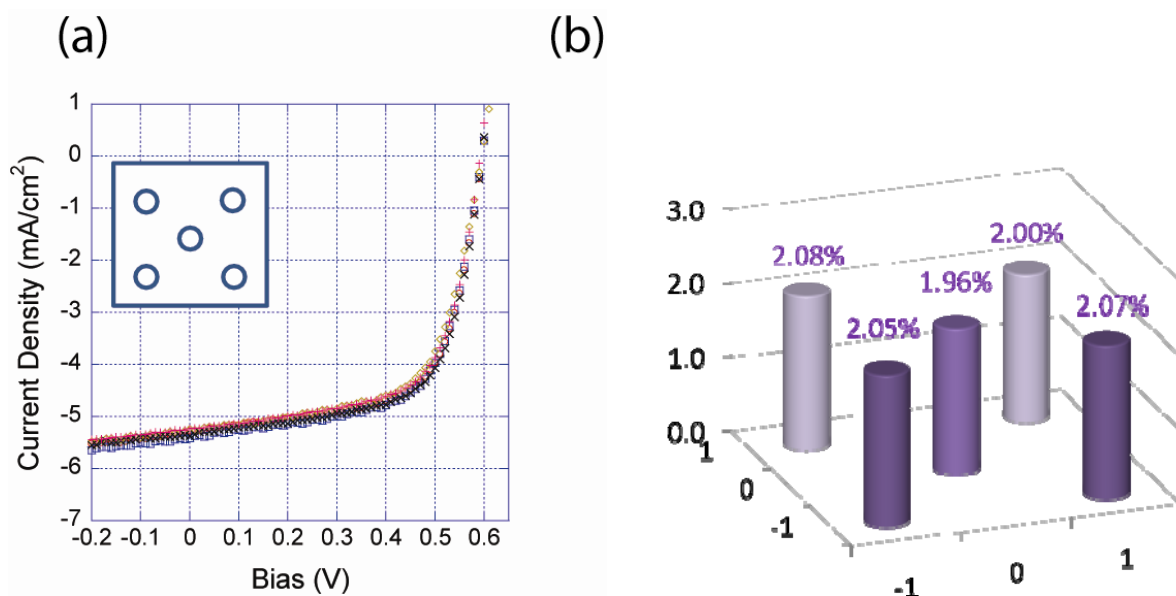


**Figure 3.6.** The reproducible device performance of five OPVCs on an ITO substrate (a) J-V curves of five OPVCs, and (b) Each bar in the figure 3.6(b) represents the PCE of each device.

First, five OPVCs were fabricated on a single ITO substrate and the device performance was characterized (Fig. 3.6 and Table 3.1). The observed  $J_{sc}$ ,  $V_{oc}$ , FF, and PCE are all very consistent. Mainly  $J_{sc}$  changed from 5.24 to 5.42 mA/cm<sup>2</sup> with standard deviation ( $\sigma$ ) 0.082 and  $V_{oc}$  was fixed at 0.59V ( $\sigma=0.002$ ). The FF range was 0.62~0.65 and the resulting PCE was 1.96~2.07% ( $\sigma=0.050$ ) indicating reproducible performance.

To achieve highly reproducible performance of OPVC, uniform thin film coating was the critical variable to control (Fig. 3.1(b) inset). The above reproducibility test was done on the five cells fabricated on a single spin cast film that has uniform thickness. However, making uniform thickness films under 200 nm thick is not always guaranteed. Solution concentration, spin speed, and the amount of dropped solution can cause the thickness variation from the center to the edge. The thickness could vary by sample to sample as well. When a polymer having a high extinction coefficient like P3HT is spincoated on a substrate the thickness variation can be easily recognized by visual observation of a color gradient from the center to the edge.

To test this, seven devices having the same structure were fabricated on different substrates in one batch (Fig. 3.7(a)). The obtained J-V curves of the seven devices were very consistent and matched well with the J-V curves of the samples in Figure 3.7. This

reproducible performance allows comparing the performances of experimental devices and control devices since experimental devices should be fabricated separately from the control cells.

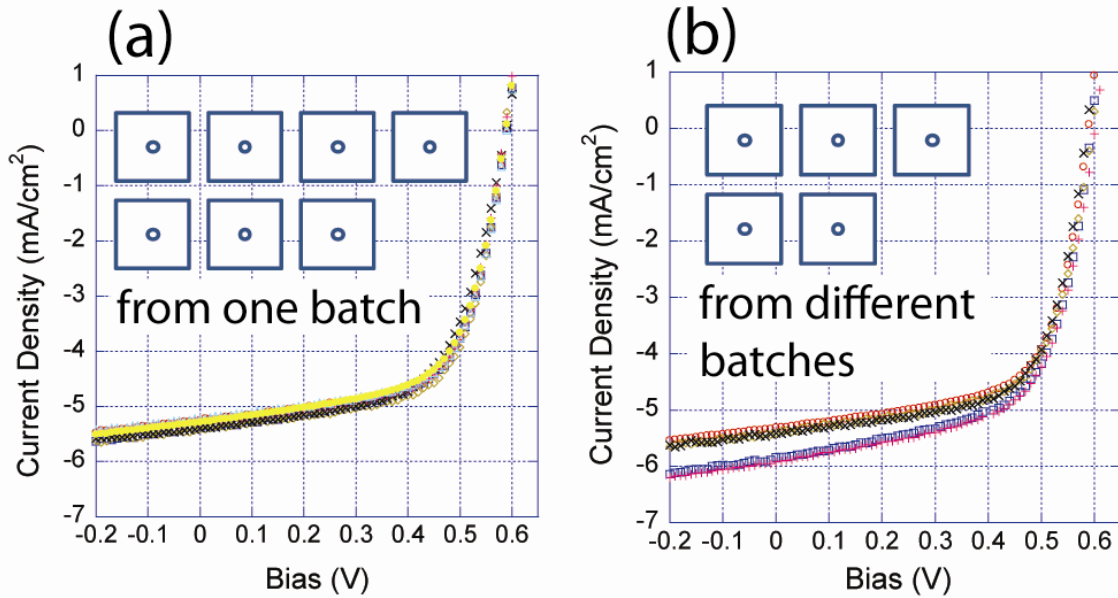


**Figure 3.7.** The Performance variations of (a) seven devices fabricated on different ITO substrates in one batch (b) five devices fabricated on different ITO substrates in different batches.

More serious performance variation tests were performed on multiple devices fabricated in different batches (Fig. 3.7(b)). The J-V curves from all devices show excellent reproducibility of the performances.  $V_{oc}$ , FF and PCE of the devices were 0.59V ( $\sigma = 0.005$ ), 0.63 ( $\sigma = 0.013$ ), and 2.10% ( $\sigma = 0.069$ ), and  $J_{sc}$  ranged from 5.41 to 5.92mA/cm<sup>2</sup> ( $\sigma=0.279$ ) (Table I). This relatively large standard deviation of  $J_{sc}$  may be attributed to the different exposure of the devices to oxygen and moisture. In the whole device fabrication process, the devices were exposed to ambient condition twice - when the devices were transferred from a glove box to an evaporation chamber and when the devices were characterized. Nevertheless, considering the reported performance variation of silicon photovoltaic devices is around 5%, the obtained 8% performance variation of OPVC indicates that reproducible and reliable OPVCs can be fabricated through the control of the critical processing parameters.

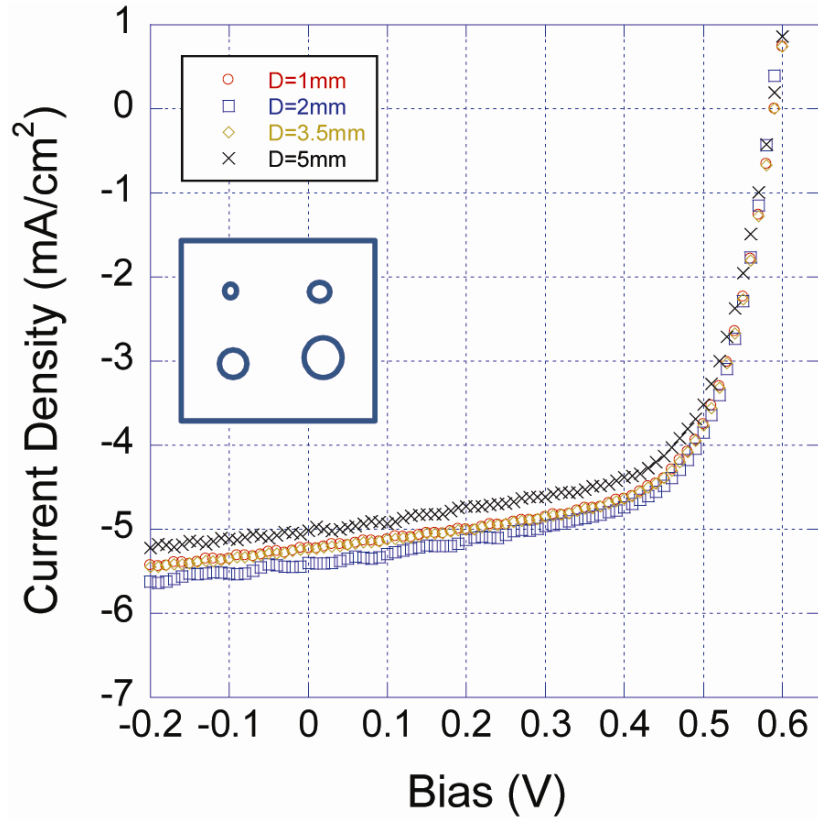


**Figure 3.8.** The performance variation of OPVC having different device sizes.

**Table 3.1.** The statistical analysis of comprehensive device performance of OPV cells

		$J_{sc}$ (mA/cm <sup>2</sup> )	$V_{oc}$ (V)	$J_{max}$ (mA/cm <sup>2</sup> )	$V_{max}$ (V)	FF	PCE (%)
Five devices on an ITO substrate	Ave.	5.31	0.59	4.34	0.46	0.64	2.03
	$\sigma$	0.082	0.000	0.058	0.007	0.009	0.050
	Range	5.24- 5.42	0.59	4.25- 4.40	0.46	0.62- 0.65	1.96- 2.07
Seven devices on different ITO substrates from one batch	Ave.	5.32	0.59	4.38	0	0.63	1.98
	$\sigma$	0.075	0.000	0.083	0.008	0.012	0.039
	Range	5.22- 5.41	0.59	4.25- 4.48	0.45- 0.46	0.61- 0.65	1.86- 2.02
Five devices on different ITO substrates from different batches	Ave.	5.58	0.59	4.51	0.47	0.63	2.10
	$\sigma$	0.279	0.005	0.161	0.005	0.013	0.069
	Range	5.31- 5.92	0.59- 0.60	4.31- 4.67	0.46- 0.47	0.62- 0.65	2.03- 2.19
Four devices having different size on an ITO substrate	Ave.	5.22	0.59	4.30	0.46	0.64	1.96
	$\sigma$	0.156	0.005	0.124	0.006	0.003	0.070
	Range	5.01- 5.39	0.59	4.12- 4.39	0.45- 0.46	0.63	1.86- 2.02

As the last variable, we tested the effects of the device size on the performance variation. Multiple devices having different sizes were fabricated on a single ITO substrate as shown in Figure 3.8 and the device performance was characterized. When the device fabrication was not optimized, the size dependence of the device performance was significant as seen in Figure 3.3. However, after device fabrication was optimized, the devices having different diameters from 1mm to 5mm showed consistent performances.  $V_{oc}$  is fixed at 0.6V and  $J_{sc}$  changes from 5.0 to 5.5mA/cm<sup>2</sup>.

### **3.4 Conclusion**

In conclusion, highly reproducible performance of OPVC can be achieved through proper control of the critical processing variables. In order to achieve highly reproducible OPVC performance, uniform blend layer through filtration of P3HT/PCBM solution must be prepared. Oxygen and moisture exposure of devices w/o encapsulation, which is assumed as one of reasons causing large device performance variation, showed only 10% degradation of device performance for 1hour characterization with continuous illumination at ambient atmosphere. After the optimization of device fabrication conditions, carefully fabricated OPVCs showed less than 8% of device performance variation of PCE. Despite the fact that the blend OPVC is composed of a random mixture of the donor and the acceptor and the resulting disordered structure might raise doubt about reliability of device performance of blend cells, our systematic analysis showed reproducible and reliable performance of OPVC.

### 3.5 References

1. K. M. Coakley and M. D. McGehee, *Chem. Mater.* **16**, 4533 (2004).
2. F. Zhang *et al.*, *Adv. Mater.* **18**, 2169 (2006).
3. Y. Kim *et al.*, *Nature Materials* **5**, 197 (2006).
4. M. M. Wienk *et al.*, *Appl. Phys. Lett.* **88**, 153511 (2006).
5. Peter Peumans, Barry P. Rand, and Stephen R. Forrest, *J. Appl. Phys.* **96**, 12 (2004).
6. M. Shtein and Stephen R. Forrest F. Yang, *Nature Materials* **4**, 37 (2005).
7. Grevin *et al.*, *Adv. Mater.* **15**, 881 (2003).
8. Campoy-Quiles *et al.*, *Nature Materials* **7**, 158 (2008).
9. G. Li V. Shrotriya, Y. Yao, T. Moriarty, K. Emery and Y. Yang, *Adv. Func. Mater.* **16**, 2016 (2006).
10. M.-G. Kang M.-S Kim, L. Jay Guo and J. Kim, *Appl. Phys. Lett.* **92**, 133301 (2008).
11. I. Pereyra and A. M. Andrade, *Solar Cells* **12**, 285 (1984).
12. Hiench *et al.*, *J. Vac. Sci. Technol. A* **1(2)**, 360.
13. Shaheen *et al.*, *J. Appl. Phys.* **84**, 2324 (1998).
14. Brabec *et al.*, *Appl. Phys. Lett.* **80**, 1288 (2002).
15. Rusu *et al.*, *Appl. Phys. Lett.* **90**, 153511 (2007).
16. Jian-Liang Liao Chih-Ming Yang, and Kuan-Cheng Chiu, *J. Appl. Phys.* **96**, 1933 (2004).
17. A. F. Hebard and M. S. Dresselhaus B. Pevzner, *Phys. Rev. B.* **55**, 16439 (1997).

## CHAPTER 4

### THE EFFECTIVE VARIABLES TO CONTROL FILL FACTOR OF ORGANIC PHOTOVOLTAIC CELLS

#### 4.1 Introduction

The high energy demand in this high energy price era and the global warming caused by fossil fuels have made an alternative green energy as a desperate solution not an option. Although as a promising alternative energy photovoltaic cells and bio fuel technology have drawn much attention recently photovoltaic technology is a more promising because solar energy is abundant, free, and green while bio fuels can produce carbon dioxide.

Among the photovoltaic technologies, organic photovoltaic cell (OPVC) technology emerged recently and recorded 3.5~ 6.5% power conversion efficiency (PCE).<sup>1,2,3</sup> Considering that 10% PCE is the minimum limit for the practical use of photovoltaic technology, more progress is demanded. So far from a single cell device, 5% is the best PCE which was obtained from P3HT and PCBM blend cell structure. Among the limiting factors of PCE of OPVC are limited light absorption efficiency and the low hole mobility ( $\sim 10^{-3} \text{cm}^2/\text{V}\cdot\text{s}$ ) of the semiconducting organics.<sup>4</sup> To improve the absorption efficiency, Lee *et al.* fabricated organic tandem cells having a front cell composed of an IR absorbing polymer and  $\text{C}_{60}$  derivative and a back cell of P3HT and PCBM. The tandem cell produced 6.5% PCE.<sup>2</sup> This approach successfully addressed the limited light absorption efficiency of OPVC and opened a new strategy to improve PCE by harvesting wider wavelength range of the solar spectrum. On the other hand the limited hole mobility of semiconducting polymers can be addressed by the morphology control and more radically and ideally through rational design of new materials. For example, the

order of  $0.1 \text{ cm}^2/\text{V}\cdot\text{s}$  hole mobility of P3HT single layer, three orders of magnitude higher than that of P3HT:PCBM blend layer, clearly implies that there is a large room for improvement by controlling the morphology of blend layer.<sup>5</sup>

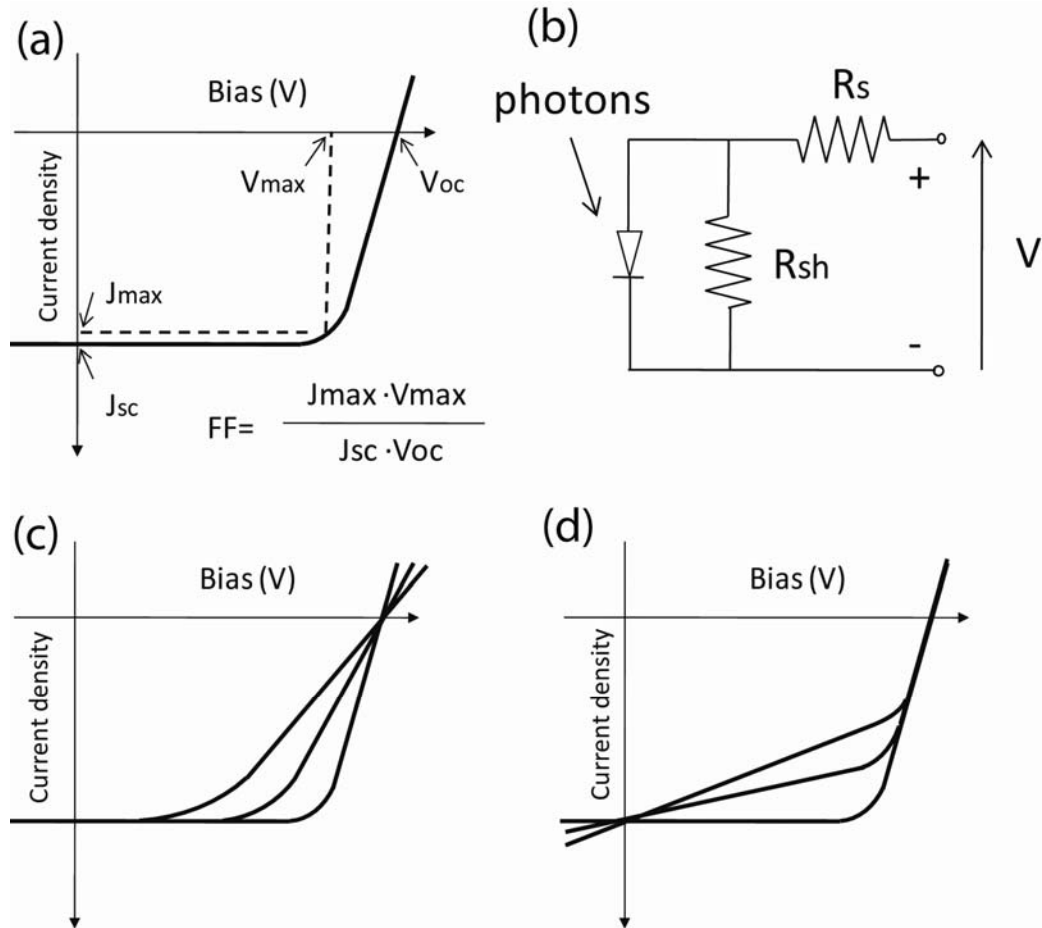


**Figure 4.1.** (a) The definition of fill factor (FF),  $J_{max}$ : current density at the maximum of  $J \times V$  in 4<sup>th</sup> quadrant,  $V_{max}$ : bias at the maximum of  $J \times V$  in 4<sup>th</sup> quadrant (b) Circuit of photovoltaic device,  $R_s$ : series resistance,  $R_{sh}$ : shunt resistance (c) Model of series resistance ( $R_s$ ) impacting FF (d) Model of shunt resistance ( $R_{sh}$ ) impacting FF.

To maximize PCE of OPVC, understanding on the parameters that affect on  $J_{sc}$ ,  $V_{oc}$ , and FF should be made. FF is defined by  $(J_{max} \times V_{max}) / (J_{sc} \times V_{oc})$  (Fig 4.1(a)) and its characteristic is determined by series resistance ( $R_s$ ) and shunt resistance ( $R_{sh}$ ) of the device (Fig 4.1(c),(d)).<sup>6</sup>  $R_s$  is the measure of the series resistance of the organic semiconductor layer, which is related with the intrinsic resistance, morphology, and thickness of the semiconductor layer.  $R_s$  determines the slope of J-V curve in the 1<sup>st</sup> quadrant and is calculated by  $V/J$ . On the other hand, the shunt resistance  $R_{sh}$  is



correlated with how much charge are recombined and generate the leakage current that are closely related to the amount and character of the impurities and/or defects in the active organic semiconductor layer.  $R_{sh}$  determines the slope of JV curve in the 4<sup>th</sup> quadrant.

Gupta *et al.* investigated the concaved-up shape of S-like JV curve having drastically small FF. In their investigation, the concaved up shape JV curve was explained by charge accumulation at the interface between an electrode and the organic semiconducting layer.<sup>7</sup> To verify that hypothesis, the authors prepared two types of OPVCs - one was ITO/PEDOT:PSS/P3HT+PCBM/Al and the other was ITO/PEDOT:PSS/P3HT+PCBM/Ca/Al. The former device showed the concaved up shape IV curve and the obtained FF was only 0.12. In the latter device, the thin calcium layer at the interface of Al and the organic layer facilitates the charge collection due to the ohmic contact and the resulting FF was improved up to 0.37. Instead of Ca Brabec *et al.* added a lithium fluoride layer between the blend layer and the aluminum cathode and observed enhanced FF from 0.5 up to 0.6.<sup>8</sup> In this case, the authors explained that the enhanced FF originates from the dipole formation induced by LiF rather than the ohmic contact formation.

In this chapter, we report the relationships between FF and various parameters including the quality and thickness of the OPVC blend layer and the two interfaces between the electrodes and the blend layer. Through the study we used island-type electrode geometry to prevent the additional charge collection observed from the crossbar type device configuration.<sup>9</sup>

## 4.2 Experimental

### 4.2.1 Materials

In this investigation, two isomeric conjugated polymers were used – regio-random poly (3-hexylthiophene) (RRa P3HT) was polymerized by using FeCl<sub>3</sub> and regio-regular poly (3-hexylthiophene) RRe P3HT and PCBM were purchased from Rieke Metals and American Due source, respectively.

### 4.2.2 Device fabrication and characterization

ITO coated glasses were cleaned with acetone and IPA. After drying the substrates with air, the substrates were treated with UV ozone for 5 min. PEDOT:PSS (Baytron PH 500) was spin cast on the cleaned ITO as received and baked for 15 min. at 130°C. To vary the conductivity of PEDOT:PSS, 5wt% of dimethyl sulfoxide (DMS) was added in PEDOT:PSS solution. Conjugated polymers, RRa P3HT and RRe P3HT, with PCBM blend solutions (1:1 wt %, 20mg/ml in chlorobenzene) were prepared with stirring the solution over 24hrs. in a glove box and spun cast at 1000 rpm for 30sec. The samples were then annealed at 130°C. 1 nm LiF and 100 nm Al layers were deposited sequentially under  $5 \times 10^{-7}$  torr. When only Al was deposited without LiF, the devices were annealed after deposition. All devices were characterized under the ambient condition and the typical illumination intensity was 100 mW/cm<sup>2</sup> (AM 1.5G Oriel solar simulator) and for the illumination intensity study the illumination intensity varied from 20 mW/cm<sup>2</sup> to 500 mW/cm<sup>2</sup>. The IV plots were recorded using a HP semiconductor analyzer.

### 4.3 Results and Discussion

We have systematically tested the effect of the character of the organic layers, such as, the morphology, thickness, and regioregularity of the conjugated polymer to the FF. The device structure was ITO/PEFOT:PSS/P3HT+PCBM/LiF/Al.

#### 4.3.1 Blend morphology effect on FF

We used regio-regular poly (3-hexylthiophene) (RRe P3HT) and PCBM and studied the effect of the blend morphology on the FF. The Regio-regularity of P3HT provides better crystallinity to the polymer and the crystallinity can be controlled by tuning the molecular packing through thermal annealing.<sup>10</sup> When the blend layer was annealed, the blend film showed a bathochromic shift to darker purple which comes from the enhanced intermolecular packing of P3HT by thermal annealing (Fig. 4.2(a)). The absorption maximum moved from 500nm to 520nm and the overall absorption efficiency increased due to the formation of the ground state aggregation and backbone planarization, which can be observed through the gradual shift of the  $\lambda_{\text{max}}$  depending on the annealing time. The crystal formation by better molecular packing through annealing was confirmed by XRD (Fig. 4.2(b)). The hexyl side chains of P3HT are interdigitated in the P3HT crystal and the sharp peak at  $5.4^\circ$  (16 Å spacing) is assigned to the distance between P3HT backbones that is closed to the length the fully extended hexyl side chain (13 nm). As the sample was annealed the peak at  $5.4^\circ$  grew indicating the thermally induced better molecular packing. The broad peak at  $25^\circ$  (3.8 Å spacing) is originated from the distance between the cofacially arranged thiophene rings.

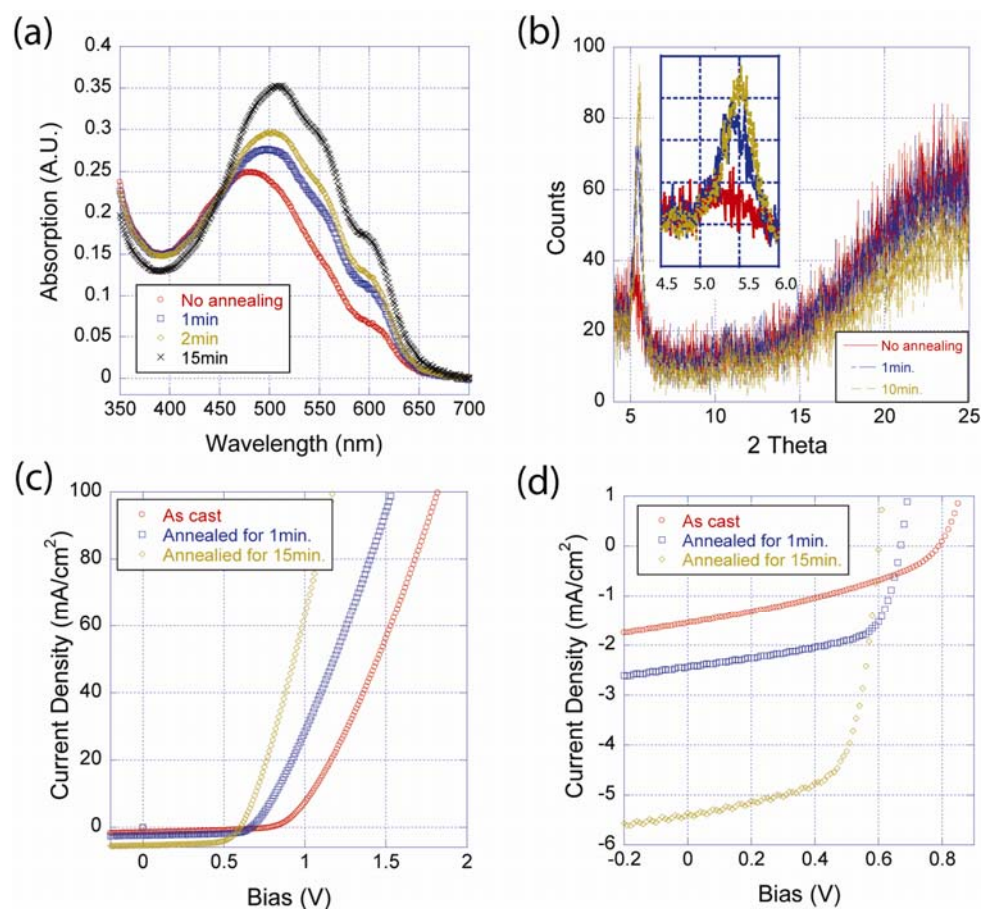


**Figure 4.2.** The annealing effect on the FF of OPVCs (a) Absorption change affect by thermal annealing. (b) Crystallinity evolution during thermal annealing (c) and (d) JV curve evolution during thermal annealing for 15min. in different scale.

The molecular packing of the conjugated polymer turned out to largely influence on  $R_s$  of the OPVC (Fig. 4.2(c) and table 4.1). As the device was annealed, the  $R_s$  decreased from 9.6 to 3.8  $\Omega\text{cm}^2$ . Since the charge transport in the semiconducting organics occurs by intramolecular charge transport and intermolecular charge transport the thermally induced better intermolecular packing and crystallization allow more efficient charge transport.<sup>11</sup> The kink and torsional disorder along the conjugated polymer backbone can be considered as a defect that increase the resistivity of the conjugated polymer as a conducting conduit. As the backbone of conjugated polymers gets densely packed through thermal annealing, the kink and torsional disorder should be reduced in some extents.<sup>12</sup> Furthermore, densely packed conjugated polymer backbone will provide more efficient intermolecular charge hopping as well.

**Table 4.1.** The performances of P3HT and PCBM blend photovoltaic devices under different various annealing conditions

Annealing time (min.)	$J_{sc}$ (mA/cm <sup>2</sup> )	$V_{oc}$ (V)	PCE (%)	$R_s$ ( $\Omega \cdot \text{cm}^2$ )	FF
0	1.54	0.8	0.44	9.6	0.36
1	2.43	0.67	0.99	6.7	0.61
15	5.36	0.6	2.10	3.8	0.65

The detailed device performances are summarized in table 4.1. As the active layer was annealed, PCE increased from 0.44% to 2.10%. As the device was annealed, the PCE increased from 0.44% to 2.10% due to the increased  $J_{sc}$  and FF. FF increased from 0.31 to 0.65 due to the reduced  $R_s$ . However,  $R_{sh}$  doesn't account for FF enhancement JV curves showed essentially the same  $R_{sh}$  values (Fig. 4.2(c)). The enhanced  $J_{sc}$  can be attributed to not only the increased absorption efficiency but also the reduced resistivity of the blend layer.

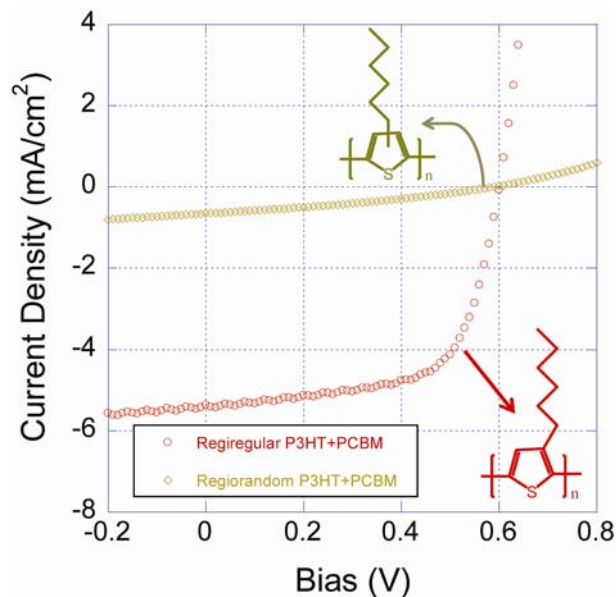


**Figure 4.3.** The regio regularity effect of conjugated polymers on FF.

**Table 4.2.** Device performances of P3HT and PCBM blend photovoltaic devices having different regioregularity of the conjugated polymer

	$J_{sc}$ (mA/cm <sup>2</sup> )	$V_{oc}$ (V)	PCE (%)	FF	$R_s$ ( $\Omega \cdot \text{cm}^2$ )	$R_{sh}$ ( $\Omega \cdot \text{cm}^2$ )
Regiorandom P3HT+PCBM	0.65	0.59	0.12	0.31	0.05	1.6
Regioregular P3HT+PCBM	5.40	0.60	2.12	0.65	0.005	1.1

### 4.3.2 The effect of regioregularity of conjugated polymer on FF

As a supporting experiment for the molecular packing consideration, we built PV cells with region-random P3HT as well and examined the regioregularity effect on FF. All other fabrication conditions were kept the same. Even after the same thermal annealing the cells having regio-random P3HT did not show any color change unlike the regio-regular P3HT due to the lack of molecular regularity required for crystallization. As we can clearly see from Figure 4.3, the performance of the cells composed of regio-regular P3HT was much better than that of the cells with region-random P3HT. Both the  $R_s$  and  $J_{sc}$  were one order of magnitude lower for the regio-regular cells than the region-random cells. The  $R_{sh}$  of the regio-regular cells is larger than that of regio-random cells indicating that there are more charge recombination in the regio-random cells. Due to the smaller  $R_s$  and larger  $R_{sh}$ , the FF of the regio-regular cells was much larger (0.65) than that of regio-random cells (0.31). These data clearly support that the morphology and molecular packing of the blend layer is detrimental to FF.

### 4.3.3 Blend film thickness effect on FF

Another important variable in the blend layer having an impact on FF is film thickness. The thickness was varied from 150nm to 800nm.  $R_s$  increases and  $R_{sh}$  decreases as the device thickness increases. The obtained JV curves shown in Figure 4.4(a) and (b) and table 4.3 clearly demonstrate the relationship between the device thickness and the  $R_s$  and  $R_{sh}$ . As the device thickness increased,  $R_s$  increased from 0.005 to 0.059  $\Omega \cdot \text{cm}^2$  indicating that the blend layer became more resistive and  $R_{sh}$  decreased from 0.83 to 0.29  $\Omega \cdot \text{cm}^2$  implying that there are more charge recombination and leakage current. As the result FF gradually decreased from 0.65 for 150 nm thick cells to 0.38 for 800 nm thick cells. An interesting phenomenon was observed in Figure 4.4(a). Even

though the thickness of the blend layer increased largely from 150 through 320 to 800 nm the  $J_{sc}$  minimally increased from the 150 nm cell to the 320 nm cells. The  $J_{sc}$  even decreased when the thickness increased further to 800 nm. As the thickness of the energy harvesting blend layer increases more photons should be absorbed into the solar cells but the reduced  $J_{sc}$  implies there is more charge recombination in the thicker cells due to the longer travel distance of the charges to the electrodes.

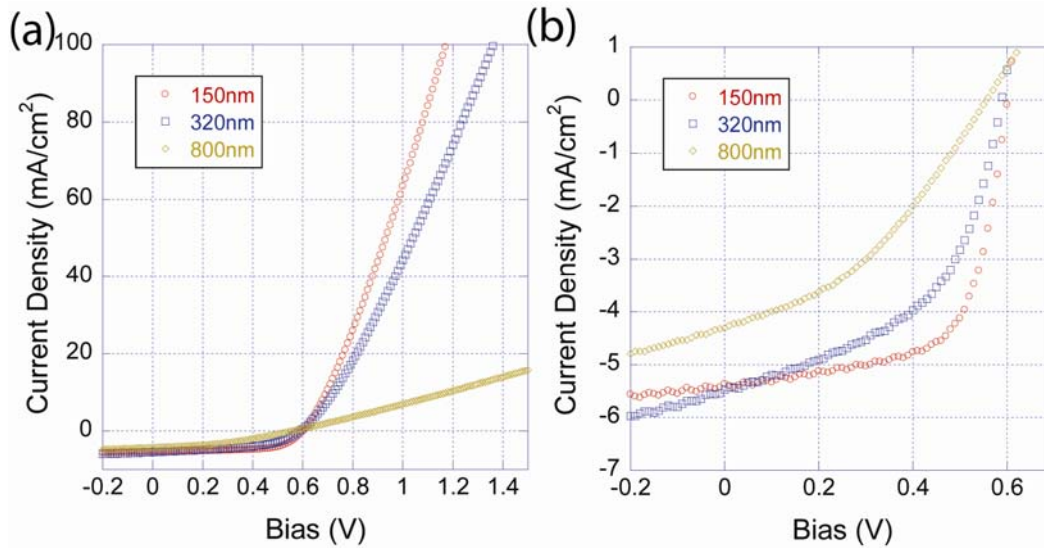


**Figure 4.4.** Thickness effect on FF.

**Table 4.3.** The device performance depending on blend layer thickness effect

P3HT PCBM layer thickness	$J_{sc}$ (mA/cm <sup>2</sup> )	$V_{oc}$ (V)	PCE (%)	$R_s$ ( $\Omega \cdot \text{cm}^2$ )	$R_{sh}$ ( $\Omega \cdot \text{cm}^2$ )	FF
150nm	5.36	0.60	2.10	0.005	0.83	0.65
320nm	5.47	0.58	1.62	0.007	0.36	0.51
800nm	4.31	0.55	0.91	0.059	0.29	0.38

#### 4.3.4 The effect of interface between blend layer and electrode on FF

In the previous section, we could understand that the blend layer morphology, regioregularity, and thickness have significant impact on FF. We further investigated the effects of two interfaces between electrodes and blend layer on FF. First, the effect of the interface between the cathode and the blend layer was examined before and after thermal annealing after Al deposition. The device structure for this study was ITO/PEDOT:PSS/P3HT+PCBM/Al without LiF. In order to exclude any morphological

effects of the P3HT:PCBM blend layer, before the Al deposition the blend layer was pre-annealed. Overall as the device was annealed, all important parameters,  $J_{sc}$ ,  $V_{oc}$  and FF, largely changed:  $J_{sc}$ :  $4.5 \sim 5.5 \text{ mA/cm}^2$ ,  $V_{oc}$ :  $0.3 \text{ V} \sim 0.58 \text{ V}$ , and FF:  $0.43 \sim 0.60$  (Fig. 4.5 and table 4.4.) As the device was annealed up to 20 min. FF changed from 0.43 to 0.60 which can be explained by not  $R_s$  but  $R_{sh}$ . The inset of Figure 4.5 shows consistent  $R_s$  value regardless of the annealing condition. However,  $R_{sh}$  increased significantly from  $0.3 \Omega \cdot \text{cm}^2$  to  $1.5 \Omega \cdot \text{cm}^2$  when the device was annealed for 20 minutes. This indicates that annealing reduces charge recombination and leakage current. We believe that the thermal annealing induced better Al contact with the blend layer and facilitate charge collection that is also supported by the improved  $J_{sc}$ .<sup>13</sup>

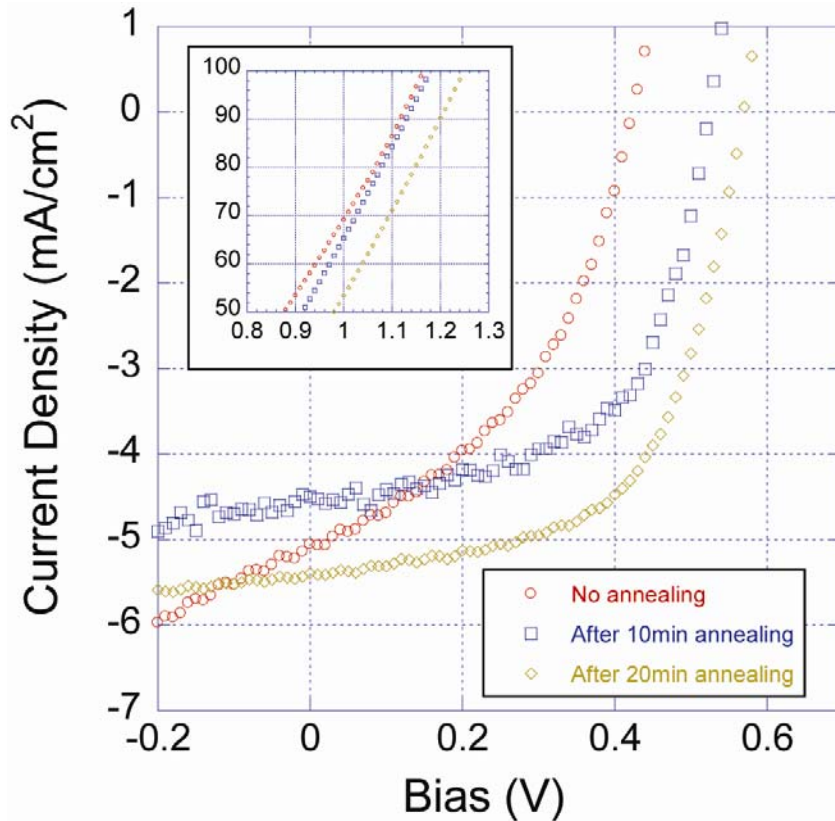


**Figure 4.5.** The interface effect between the cathode and the blend layer on FF. (inset) currents from 0.8V to 1.3V which shows  $R_s$ .



**Table 4.4.** FF change depending on the interface between cathode and blend layer

	$J_{sc}(\text{mA}/\text{cm}^2)$	$V_{oc}$ (V)	PCE (%)	FF
Not annealed	5.06	0.42	0.92	0.43
Annealed for 10min.	4.50	0.52	1.37	0.59
Annealed for 20min.	5.40	0.56	1.81	0.60

The effect of another interface between the anode and the blend layer was investigated by using electrode materials having different conductivity such as PEDOT:PSS (Baytron PH 500,  $\sigma=100$  S/cm), PEDOT:PSS (Baytron PH 500 + 5wt% DMS, 300 S/cm), and PEDOT:PSS (Baytron PH 500,  $10^5\sim 10^6$  S/cm) on ITO. The device structure was anode/P3HT+PCBM/LiF/Al. As we can see in Figure 4.6 (a) and Table 4.5, as the anode conductivity decreased  $J_{sc}$  and FF decreased.<sup>14</sup> This trend can be explained by the fact that the efficiency of charge extraction decreases as the conductivity of the anode decreases. To support this hypothesis, we conducted two more experiments. In the first supporting experiment, the amount of photogenerated charges was controlled by varying the illumination intensity on the cells having PEDOT:PSS+5wt% DMS/P3HT+PCBM /LiF/Al (Fig. 4.6(b)). The anode of these cells has a low conductivity and the resulting FF was 0.20 under 1 sun intensity (Table 4.5). As the light intensity decreased down to 0.01 sun intensity FF increased to 0.30 even though the  $J_{sc}$  also decreased (Fig. 4.6(b) and Table 4.6).

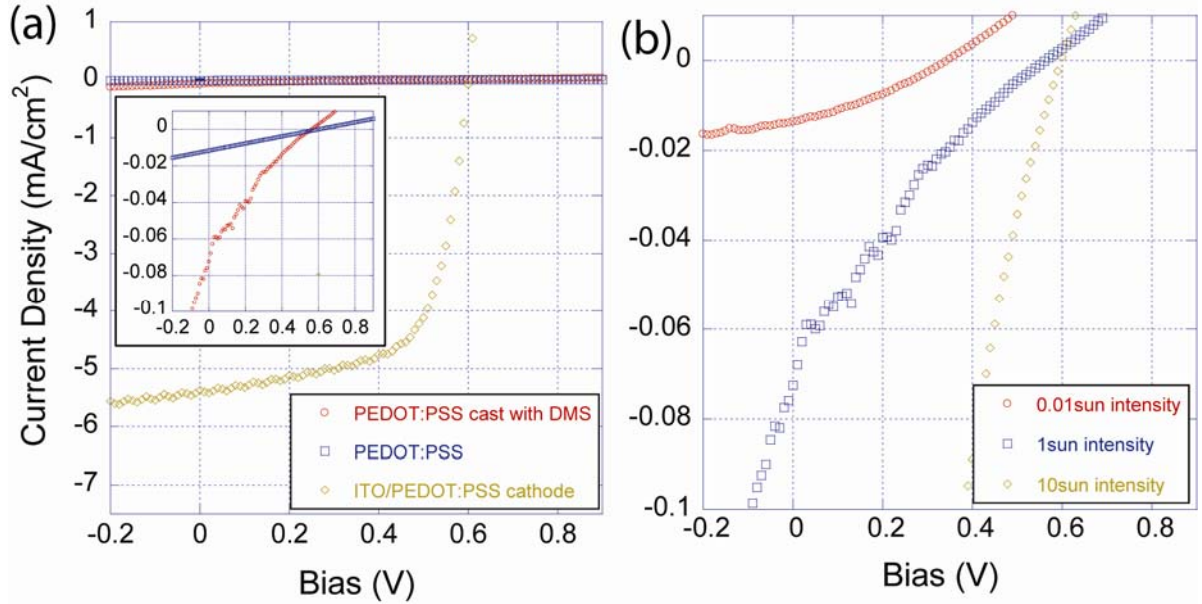


**Figure 4.6.** (a) The effect of anode conductivity on FF and (b) Illumination intensity effect on FF.

**Table 4.5.** Device performances depending on anode conductivity

	$J_{sc}$ (mA/cm <sup>2</sup> )	$V_{oc}$ (V)	FF
PEDOT:PSS	0.02	0.59	0.16
PEDOT:PSS (w/ 10% DMS)	0.07	0.57	0.20
ITO/PEDOT:PSS	5.36	0.60	0.64

**Table 4.6.** Device performances depending on illumination intensity

Intensity	$J_{sc}$ (mA/cm <sup>2</sup> )	$V_{oc}$ (V)	FF
0.01 sun	0.01	0.35	0.30
1 sun	0.08	0.57	0.20
10 sun	0.53	0.59	0.17

### 4.3.5 The effect of light intensity on FF

When the illumination intensity was varied from 0.2 to 5 sun intensity  $J_{sc}$  increased accordingly but the  $R_{sh}$  decreased gradually likely due to charge recombination in the blend layer. As the illumination intensity increases the amount of absorbed photon to the PV cell also will increase. That explains the increased  $J_{sc}$ . However, as the amount of photo-induced charges increases in the blend layer the chance of charge recombination can be reasonably expected to increase as well due to the limited charge collection efficiency at the interface between the blend layer and the anode resulting in more leakage current and decrease in  $R_{sh}$ . While the illumination intensity largely influence on  $R_{sh}$  it does not affect much on  $R_s$  as we can see from Figure 4.7 (b). Therefore, the inverse correlation between FF and the illumination intensity does not come from  $R_s$  but from  $R_{sh}$ .

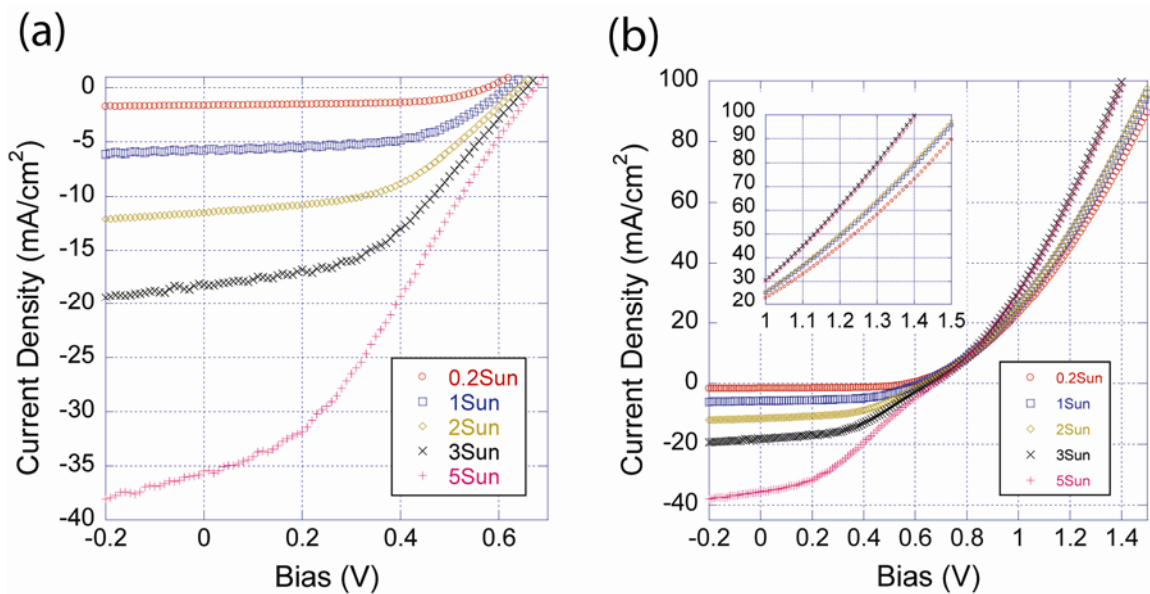


**Figure 4.7.** JV curves of a P3HT and PCBM blend photovoltaic device under various illumination intensities. (a) JV curves from -0.2V to 0.7V (b) JV curves from -0.2V to 1.5V. The larger scale JV curves are added to provide the graphical information of  $R_s$ .

**Table 4.7.** The device performances of a P3HT and PCBM blend photovoltaic device under various illumination intensities

	$J_{sc}(\text{mA}/\text{cm}^2)$	$V_{oc}(\text{V})$	PCE	FF
0.2Sun	1.64	0.57	2.84	0.61
1Sun	5.83	0.61	2.00	0.56
2Sun	11.5	0.64	1.76	0.48
3Sun	18.2	0.66	1.63	0.41
5Sun	35.5	0.68	1.62	0.34

#### 4.4 Conclusion

In this chapter, the effective variables having impact on FF of OPVC having P3HT and PCBM were systematically identified. Systematic understanding of the way to control FF and the correlation between the device variables and  $R_s$  and  $R_{sh}$  are important to achieve high performance OPVC. As the variable in the blend layer component, the blend morphology, the regioregularity of the conjugated polymer, and the thickness of the blend layer showed large influence on FF and through affecting on  $R_s$  and  $R_{sh}$ . When the crystallinity of the blend layer was increased by thermal annealing,  $R_s$  decreased. When the regioregular P3HT was used one order of magnitude lower  $R_s$  was also observed. The higher crystallinity induced by thermal annealing and regio-regularity should enhance the efficiency of the intermolecular and intramolecular charge transport. On the contrary, as the thickness of the blend layer increased,  $R_s$  increased and  $R_{sh}$  decreased due to the increased distance the charges should travel until they reach the electrodes and this will increase the resistivity and the charge recombination

The quality of the two interfaces between the blend layer and the electrodes was revealed to play a significant role in determining FF as well. When a less conducting cathode was used FF decreased due to more charge recombination and leakage current that was evidenced by lower  $R_{sh}$ . By controlling the amount of the photo-induced charges in the blend layer through various illumination conditions, we could prove that the  $R_{sh}$  and resulting FF are largely influence by how efficiently extract the generated charge through the cathode. As the chance of charge recombination increased in the experimental condition of the higher illumination intensity,  $R_{sh}$  and FF gradually decreased indicating more charge recombination in the blend layer. The nature of the interface between the Al anode and the blend layer turned out to be detrimental to FF as well. As the PV cells were thermally annealed after Al deposition FF  $R_{sh}$  increased indicating the interface became more favorable for charge extraction. It is likely due to the better contact between Al and the blend layer.

## 4.5 References

1. J. Y. Kim *et al.*, *Science* **317**, 222 (2007).
2. Gang Li *et al.*, *Nature Materials* **4**, 864 (2005).
3. Y. Kim *et al.*, *Nature Materials* **5**, 197 (2006).
4. Stephen R. Forrest, *MRS bulletin* **30**, 28.
5. Sirringhaus *et al.*, *Nature* **401**, 685 (1999).
6. Jenny Nelson, *The Physics of Solar Cells*. (Imperial College Press, 2002).
7. Monojit Bag Dhritiman Gupta, and K. S. Narayana, *Appl. Phys. Lett.* **92**, 093301 (2008).
8. Brabec *et al.*, *Appl. Phys. Lett.* **80**, 1288 (2002).
9. M.-G. Kang M.-S Kim, L. Jay Guo and J. Kim, *Appl. Phys. Lett.* **92**, 133301 (2008).
10. Guo *et al.*, *Thin Solid Films* **516**, 3138 (2008).
11. Wu *et al.*, *Appl. Phys. Lett.* **87**, 052103 (2005).
12. Grozema *et al.*, *J. Phys. Chem. B* **106**, 7791 (2002).
13. Kim *et al.*, *J. Kor. Phys. Soc.* **48**, 441 (2006).
14. Zhang *et al.*, *Adv. Mater.* **14**, 662 (2002).

## CHAPTER 5

### CHOICE OF ELECTRODE GEOMETRY FOR ACCURATE MEASUREMENT OF ORGANIC PHOTOVOLTAIC CELL PERFORMAMNCE

#### 5.1 Introduction

The relationship between the performance and the electrode geometry of organic photovoltaic devices was investigated to establish proper electrode geometry for reproducible and accurate performance measurement. Photovoltaic cells (ITO/PEDOT:PSS/P3HT+PCBM/LiF/Al) having crossbar-type and island-type electrode geometry were fabricated. The crossbar-type cells varied greatly in performance depending on the illuminated light beam size relative to the overlap area of the crossbar-type electrodes due to excess photo-current generated from the cell region outside the overlapped electrode area, where PEDOT:PSS plays as anode. We systematically investigated the relationship between the conductivity of the PEDOT:PSS, the illumination area and the amount of excess photo-current generated.

Organic photovoltaic cells (OPVCs) are one of the popular research areas and have been investigated intensively because of their unique advantages such as easy processability, light weight, and the flexibility in organic material design. Currently the best power conversion efficiency (PCE) of OPVC is around 3.5-6.5%.<sup>1,2,3,4,5</sup> However, since at least 10% PCE should be achieved in order to commercialize OPVC, various efforts are in progress to achieve better performance. Heterojunction solar cells having controlled nano-structures have been investigated to increase the interface area between the donor and the acceptor in order to achieve efficient exciton dissociation and charge transport<sup>6,7,8</sup>. Improving energy harvesting capability of OPVC through developing low bandgap conjugated molecules<sup>9,10</sup> and applying surface plasmonic resonance concept<sup>11</sup>

has been also actively investigated. Very recently tandem cells composed of a front cell (P3HT/PCBM blend) and a back cell (infra-red absorbing conjugated polymer/PCBM blend) were reported with 6.5% PCE and opened a new strategy to achieve a higher PCE<sup>1</sup>.

As the power conversion efficiency (PCE) is the representative parameter to evaluate the performance of photovoltaic cells, the measurement of this value should be accurate and reproducible in order that different devices can be compared on equal basis.<sup>12</sup> However, in reality it could be challenging to obtain precisely reproducible PCE even from the cells having an identical structure and composition because there are many subtle parameters such as annealing condition<sup>2,3,4,13</sup>, solvent selection<sup>14</sup>, and presence of oxygen and moisture<sup>10,15,16</sup> in the device fabrication steps and during the device characterization steps. Moreover, there are no standardized device size and structure, illumination condition, and characterization methods of OPVC. Two types of electrode configuration are often used in making OPVCs: a cross-bar type and an island electrode type. In this work, we systematically investigated the effects of the electrode geometry combined with illumination condition on the PCE of organic solar cells.



## 5.2 Experimental

### 5.2.1 Device fabrication

ITO coated glass was cleaned with acetone and IPA. After drying the substrates with air, UV ozone was treated for 5min. PEDOT:PSS (Baytron P CH 8000, Baytron P, and Baytron PH 500) was spin cast on cleaned ITO after filtering using hydrophilic filter and baked for 15min. at 130°C. P3HT and PCBM solution (1:1 wt %, 20mg/ml in chlorobenzene) was prepared with stirring over 24hrs in the N<sub>2</sub> filled glove box and spincast at 1000rpm for 30sec. Then the samples were annealed at 130°C for 15min. 1nm LiF and 100nm Al layers were deposited sequentially under  $5 \times 10^{-7}$  torr.

### 5.2.2 Electrode patterning

In this investigation, we used two kinds of geometries of electrode configurations- island shape electrode and cross bar shape electrode - in order to define active device area of OPV cell.

To build island shape cathode, first ITO coated glass was used as a substrate without any treatment. After depositing organic semiconducting layers island shape aluminum cathode was deposited using island shape mask (2mm x 2mm).

Cross shape electrode configuration required ITO and aluminum patterning. ITO layer was etched using photolithography process. Resist was spincast on ITO and baked at 115°C for 45sec. The mask having two vertical openings (2mm x 20mm) was placed on resist coated ITO substrate. Then ITO UV light was irradiated to photoresist. The sample was treated with a developer and baked again. The pattern was etched using R.I.E. and after completing etching process the remaining resist was washed with resist stripper.

### 5.2.3 Device characterization

The fabricated devices were characterized under ambient condition without encapsulation. The beam size was controlled using different size of mask ( diameters: 2mm, 3.5mm, 5mm, and 13mm). The illumination intensity was 100mW/cm<sup>2</sup> (AM 1.5G

Oriel solar simulator) and the I-V curves were obtained using HP semiconductor analyzer.

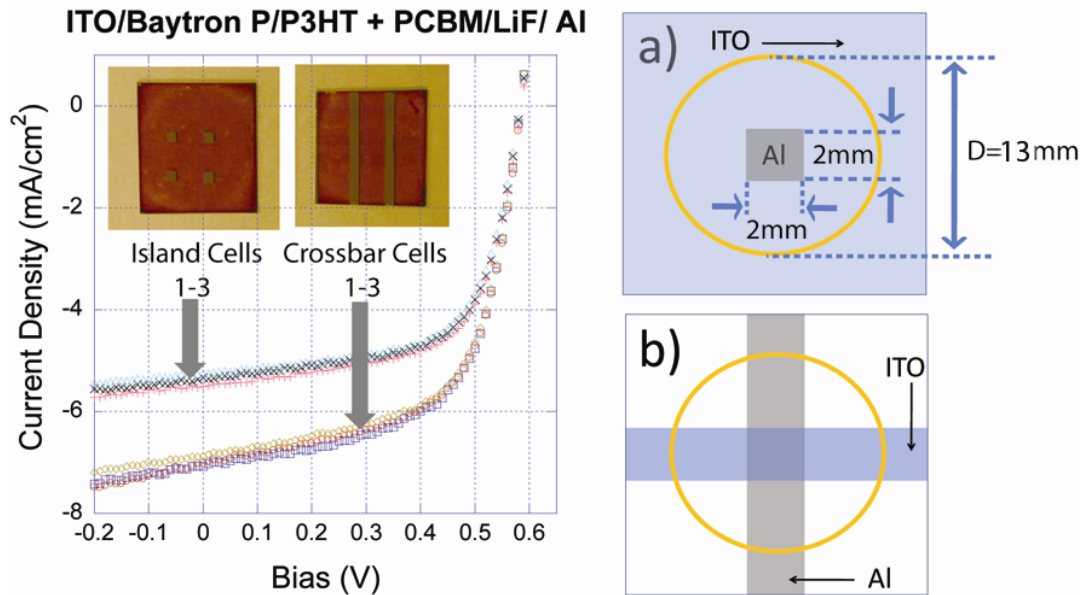
## 5.3 Results and discussion

### 5.3.1 Observation of overestimation of OPVC performance

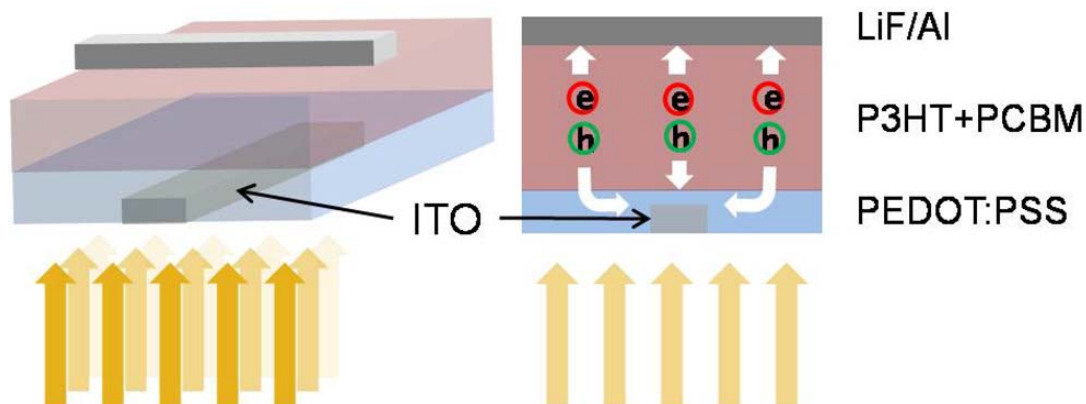
We fabricated photovoltaic cells (ITO/ PEDOT:PSS/ P3HT+PCBM/ LiF/ Al) using both aforementioned electrode configurations. The patterned crossbar-type electrode geometry is the most commonly used configuration for organic light emitting diodes (OLED) because this structure allows convenient addressing of individual pixels. The same crossbar-type electrode geometry has been adapted to OPVC fabrication for the same convenience. However, we found that the crossbar-type electrode geometry can lead to incorrect analysis of PCE of the OPVCs even though it is an acceptable structure for OLED. While the cells having the island-type electrode geometry gave consistent cell performance, the performance of the crossbar-type cells varied greatly depending on the size of the illuminated light beam on the cells relative to the overlapped area of the crossbar electrodes. When the illuminated area was larger than the overlapped area of the crossbar electrodes, excess photo-current was generated from the parasitic OPVC regions outside of the overlap area where there was no ITO electrode because the conductive PEDOT:PSS layer plays the role of an effective anode.

Figure 5.1 shows the structure of the crossbar-type cell and the island-type cell having an identical overlapped area of  $2 \times 2 \text{ mm}^2$  between the ITO anode and the Al cathode. To make the island-type PV cells a 65 nm of PEDOT:PSS layer was spin coated on to an ITO slide followed by P3HT/PCBM blend deposition (blend ratio 1:1, thickness: 150nm) by spin casting. An 1 nm-thick LiF layer and a 100 nm-thick Al were deposited subsequently through a shadow mask to form a  $2 \times 2 \text{ mm}^2$  area cathode. The crossbar-type PV cells had the same composition and layer thicknesses but used patterned ITO and Al electrodes as shown in figure 5.1 b). We analyzed the cell performance by illuminating AM 1.5G simulated sun light (Oriel Solar Simulator,  $100\text{mW}/\text{cm}^2$ ) on the PV cells. The beam diameter of the simulated sun light on the device surface was 20mm and the intensity of the light was uniform throughout the area. In principle we should expect to obtain the same cell performance from the two different types of PV cells. However, our measurements of the cell performances between the PV cells having the two different electrode geometry were consistently different. While the measured short

circuit current density ( $J_{sc}$ ) of the island-type PV cells was  $5.5\text{mA}/\text{cm}^2$ , the  $J_{sc}$  of the crossbar-type PV cells was much larger,  $\sim 7\text{mA}/\text{cm}^2$ . Multiple PV cells having the same electrode geometry of either type showed less than 5% variation in their PCE as shown in figure 5.1.



**Figure 5.1.** J-V curves of OPVCs having (a) island type electrode geometry and (b) crossbar-type electrode geometry, Illumination diameter = 13mm, Intensity: AM1.5G  $100\text{mW}/\text{cm}^2$ . For the device characterization having the island type electrode, the anode contact was made using a probe and the cathode contact was made using a gold wire.



**Figure 5.2.** Left: Characterization scheme of OPVC having crossbar-type electrode geometry under illumination larger than the overlapped area of the crossbar-type electrodes. Right: Excess current generation in PEDOT:PSS//Al device where there is no ITO.

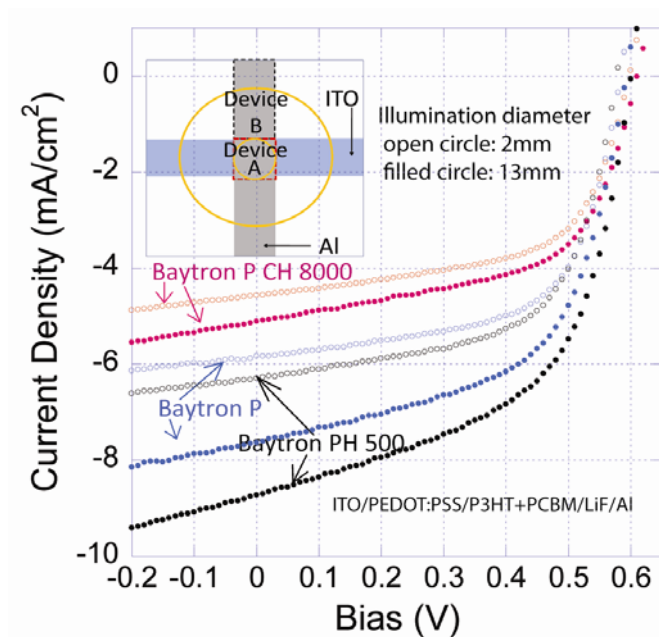


**Figure 5.3.** J-V curves of devices having (a) crossbar-type electrode geometry. Three devices having different PEDOT:PSS-(b)Baytron P CH 8000, (c)Baytron P, and (d)Baytron PH 500- were built and characterized under illumination by varying the beam diameters sizes (Beam diameters: 2mm and 13mm).

**Table 5.1.** Illumination area dependence of OPVCs ( $2 \times 2 \text{ mm}^2$ ) having crossbar-type electrode geometry

PEDOT:PSS	Beam Diameter	2mm	3.5mm	5mm	13mm
Baytron P CH 8000 $10^{-4}$ - $10^{-5}$ S/cm	Jsc ( $\text{mA}/\text{cm}^2$ )	4.57	4.95	5.11	5.11
	FF	0.59	0.57	0.56	0.56
	PCE(%)	1.63	1.71	1.77	1.78
Baytron P 0.1-1S/cm	Jsc ( $\text{mA}/\text{cm}^2$ )	5.84	7.1	7.58	7.64
	FF	0.61	0.58	0.57	0.56
	PCE(%)	2.1	2.4	2.57	2.56
Baytron PH 500 $10$ - $10^2$ S/cm	Jsc ( $\text{mA}/\text{cm}^2$ )	6.29	7.05	8.65	8.72
	FF	0.60	0.56	0.54	0.54
	PCE(%)	2.2	2.36	2.81	2.86

### 5.3.2 Evidences of extra current

We hypothesized that the excess photocurrent of the crossbar-type cells is because the conducting PEDOT:PSS layer near the overlapped electrode region also collected photo-generated holes from the area where there is no ITO as illustrated in figure 5.2. To verify this hypothesis we investigated the relationship between the conductivity of the PEDOT:PSS and the excess photocurrent. We used three different conducting PEDOT:PSS materials- Baytron P CH 8000 ( $\sigma = 10^{-4}$  - $10^{-5}$  S/cm), Baytron P ( $\sigma = 0.1$ -1 S/cm), and Baytron PH 500 ( $\sigma = 10$ -100 S/cm) and made identical crossbar-type cells. The cell performance was characterized by varying the illuminated beam sizes (beam diameter of 2mm, 3.5mm, 5mm, and 13mm) of AM 1.5 G simulated sun light (figure 5.3 and table 5.1). A few effects were observed. First, we illuminated only the overlapped electrode area by a 2.0mm beam and found that the Jsc values increased with the conductivity of PEDOT:PSS. Second, with increased beam size excess photocurrent was observed in all the crossbar-type PV cells till it eventually saturated, and the amount of the excess photocurrent increased with the PEDOT:PSS conductivity. We plotted the excess photocurrent against the size of the exposed area subtracting the overlapped electrode region in figure 5.4. As shown in the figure the excess current saturated when the excess exposed area outside of the electrode overlap (device B in figure 5.3 a)) was  $5 \text{ mm}^2$ . This indicates that only PEDOT:PSS close to the edge of the ITO electrode can collect charges and contribute to excess current; and the amount of the excess current is proportional to the conductivity of PEDOT:PSS.

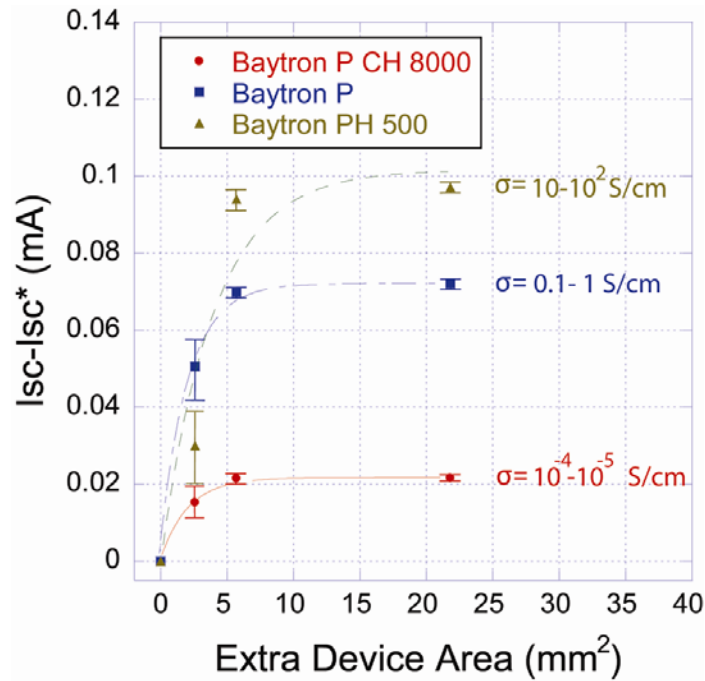


**Figure 5.4.** The plot of excess current ( $I_{sc}-I_{sc}^*$ ) from PEDOT:PSS//Al device vs. extra device area of PEDOT:PSS//Al device.  $I_{sc}$ : total current from organic photovoltaic cells having crossbar type electrode geometry,  $I_{sc}^*$ : current generated from ITO//Al device. The lines are guides for the eyes.

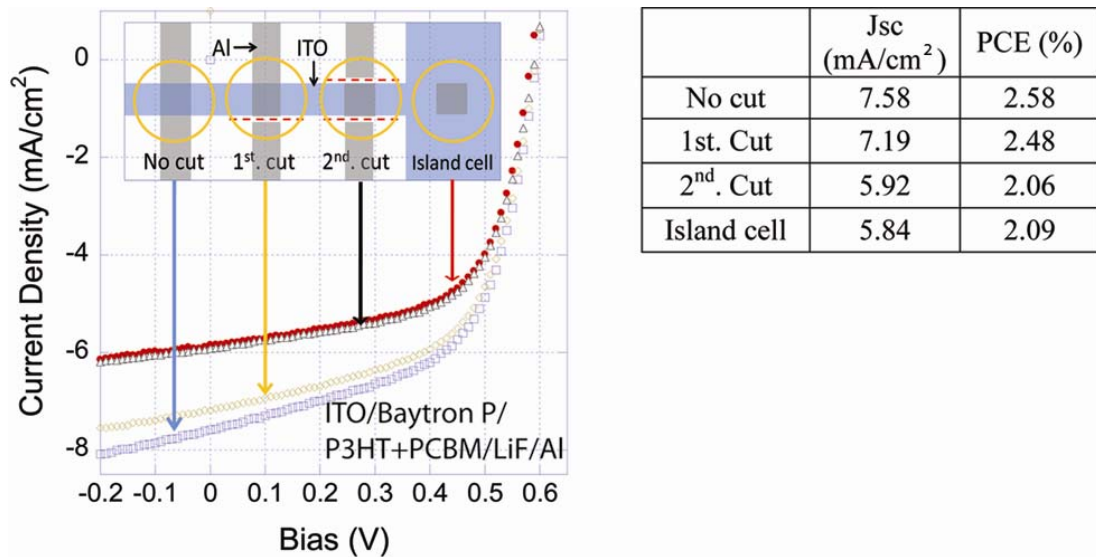


**Figure 5.5.** J-V curves of organic photovoltaic cells having crossbar-type electrode geometry as the aluminum cathode was cut to remove excess current from PEDOT:PSS//Al device. (Illumination diameter: 13mm and intensity : AM1.5G 100mW/cm<sup>2</sup>.)

Based on the experimental results, we can consider that the crossbar-type cells are composed of two types of PV cells connected in parallel. One is the PV cell having ITO anode and Al cathode (i.e. Device A in figure 5.3 a) and the other is the Device B in the same figure that has PEDOT:PSS as an effective anode instead of ITO. We built PEDOT:PSS (Baytron P)/ P3HT+PCBM/ LiF/ Al PV cells on a glass substrate without ITO to mimic the Device B in figure 5.3 a). The devices indeed showed photovoltaic characteristic but with a fill factor of only 0.25, which is much smaller than the fill factor of 0.61 of the equivalent device having ITO. This also explains why the fill factor of the crossbar-type PV cells decreased when the illuminated beam size increased, while the Jsc increased due to the contribution of the device B to the total measured Jsc. In order to directly confirm that the excess current is from the parasitic PEDOT:PSS// Al device (Device B), we built a crossbar-type PV cell (ITO/ Baytron P/ P3HT+PCBM/ LiF/ Al) and illuminated the PV cell with beam diameter of 20mm. We measured the J-V curves as we cut the Al cathode right next to the overlapped region as illustrated in figure 5.5. Cutting the Al cathode is to remove the contribution of the parasitic PV cell (i.e. device B). As we can see from the figure as the Al cathode was cut into the 2 x 2mm<sup>2</sup> square shape the Jsc and PCE decreased while the FF increased. After the second cut the J-V curve of the crossbar-type PV cell became essentially the same as that of the island-type PV cell. We found the same effects from the crossbar-type PV cells made of Baytron P CH 8000 and Baytron PH 500.

### 5.3.3 Quantitative analysis of extra current of OPVC

To quantify the characteristic length of the parasitic device region that contributes to the excess photocurrent, we modeled the crossbar-type PV cell by a parallel connection of device A and a series of distributed PV cells of different distance (and therefore different resistance) to the biased ITO electrode. As the photo-generated holes collected by the PEDOT layer have to reach to the ITO electrode to contribute to the measured photocurrent, the characteristic length of the parasitic device can be estimated by considering the voltage drop along the distance away from ITO device. The voltage drop can be expressed as  $\Delta V = \int J_{ph} \cdot R_{sq} \cdot L \, dL$ , where  $J_{ph}$  is the photocurrent,  $R_{sq}$  is the sheet



resistance, and  $L$  is the distance of the parasitic element from the ITO electrode. The maximum distance can be estimated as  $L_{\max} = \sqrt{2D V / J_{ph} R_{sq}}$ , at which the voltage drop is equal to the open-circuit voltage of the device and beyond which photo-generated holes can no longer contribute to the measured photocurrent. Based on the sheet resistance of the PEDOT material, our analysis showed this length to be  $\sim 400 \mu\text{m}$ , which is in the same order of the later extent of the region outside the overlapped electrode beyond which the measured excess current saturates.

## 5.4 Conclusions

To summarize our experiment, we found that the commonly used crossbar-type PV cells can produce a significant error in the power conversion efficiency measurement if the beam diameter of the illuminated light is larger than the area of electrodes. The larger PCE observed using such a configuration is due to excess photocurrent generated from the parasitic OPVC structure where the conductive PEDOT layer acts as an effective anode.<sup>17,18,19</sup> This can also explain why the excess photocurrent is proportional to the conductivity of the PEDOT:PSS layer and increases with the illuminated area. Two solutions are possible to prevent the error in characterization: either by making the area of light illumination equal to that of the active electrode area of PV cells or using the island-type cathode design. Considering the technical difficulty of the former method, the latter approach is more convenient and practical.

## 5.5 Reference

1. J. Y. Kim, K. Lee, N. E. Coates, D. Moses, T. -Q. Nguyen, M. Dante, and A. J. Heeger, *Science* **317**, 222 (2007).
2. G. Li, V. Shrotriya, J. Huang, Y. Yao, T. Moriarty, K. Emery, and Y. Yang, *Nature Materials* **4**, 864 (2005).
3. W. Ma, C. Yang, X. Gong, K. Lee, and A. J. Heeger, *Adv. Func. Mater.* **15**, 1617 (2005).
4. Y. Kim, S. A. Choulis, J. Nelson, D. D. C. Bradley, S. Cook, J. R. Durrant, *Appl. Phy. Lett.* **86**, 063502 (2005).
5. C. -J. Ko, Y.-K. Lin, F.-C. Chen, and C.-W. Chu, *Appl. Phy. Lett.* **90**, 063509 (2007).
6. F. Yang, M. Shtein, and S. R. Forrest, *Nature Materials* **4**, 37 (2005).
7. K. M. Coakley, and M. D. McGehee, *Appl. Phy. Lett.* **83**, 3380 (2003).
8. M. -S. Kim, J. -S Kim, J. C. Cho, M. Shtein, and L. J. Guo, *Appl. Phy. Lett.* **90**, 123113 (2007).
9. M. W. Martijn, G. R. T. Mathieu, P. S. Martin, F. Marta, and A. J. J. Rene, *Appl. Phy. Lett.* **88**, 153511 (2006)
10. W. Mammo, L. M. Andersson, S. Admassie, M. R. Andersson, O. Inganäs, and F. Zhang, *Adv. Mater.* **18**, 2169 (2006).
11. B. P. Rand, P. Peumans, and S. R. Forrest, *J. Appl. Phy.* **96**, 7519 (2004).
12. V. Shrotriya, G. Li, Y. Yao, T. Moriarty, K. Emery, and Y. Yang, *Adv. Func. Mater.* **16**, 2016 (2006).
13. S. Miller, G. Fanchini, Y. -Y Lin, C. Li, C.-W Chen, W.-F. Su, and M. Chhowalla, *J. Mat. Chem.* **18**, 306 (2008).
14. S. E. Shaheen; C. J. Brabec, N. S. Sariciftci, P. Franz, F. Thomas, and C. H. Jan, *Appl. Phy. Lett.* **78**, 841 (2001).
15. G. Dennler, C. Lungenschmied, H. Neugebauer, N. S. Sariciftci, M. Latreche, G. Czeremuszkin, M. R. Wertheimer, *Thin Solid Films* **511**, 349 (2006).
16. C. Brabec, H. Neugebauer, J.C. Hummelen, and N.S. Sariciftci, *Solar Energy Mater. & Solar Cells* **61**, 35 (2000).
17. C. S. Lee, J. Y. Kim, D. E. Lee, J. Joo, B. G. Wagh, S. Han, Y. W. Beag, and S. K. Koh, *Synthetic Metals* **139**, 457 (2003).
18. O. Inganäs and K. Tvingstedt, *Adv. Mater.* **19**, 2893 (2007).

19. While we prepared this manuscript a paper was published reporting similar excess photocurrents from crossbar-type photovoltaic cells; P. Schilinsky, and C. J. Brabec, A. Cravino, *Adv. Func. Mat.* **17**, 3906 (2007).

## CHAPTER 6

### **FLEXIBLE CONJUGATED POLYMER PHOTOVOLTAIC CELLS WITH CONTROLLED NANOSCALE HETEROJUNCTIONS FABRICATED USING NANOIMPRINT LITHOGRAPHY**

#### **6.1 Introduction**

Solar cells based on conjugated polymer (CP) offer an attractive alternative to silicon-based photovoltaic (PV) technology for low-cost solar energy conversion due to easy large-area processability, compatibility with low-cost flexible substrates, and the high degree of control over the optoelectronic properties of the CPs. However, the power conversion efficiency remains low due in part to the inefficient exciton diffusion that typically precedes exciton dissociation in organic PV cells. The typical diffusion length,  $L_D$ , of excitons in conjugate organics is only 10 to 20nm leading to a bottleneck in the photocurrent generation process. Bulk heterojunction (BHJ) polymer PV cells have been developed to improve exciton diffusion and dissociation,<sup>1,2</sup> by creating phase-separated donor-acceptor domains on the nanoscale. The spontaneous phase separation that generates the BHJ, however, results in a disordered morphology, with cul-de-sac regions that severely limit separation and transport of the geminate charges to the electrodes. Here we demonstrate CP-based flexible solar cells with well-defined interdigitated donor-acceptor interfaces that enhance the charge separation and transport processes. These devices are achieved using solution coating and nanoimprinting of the active polymer layers. Nanoimprinting enables the precise and direct nano-scale control of the shape of the donor-acceptor interface on both rigid and flexible substrates, along with solution coating is well-suited for high throughput roll-to-roll fabrication.<sup>3</sup>

In spite of its unique merits of the tunable optoelectronic properties and

processibility, a CP-based solar cell has the unsolved problem of low power conversion efficiency (PCE). This problem stems from the fact that photo-excited electrons in a CP are not free from holes. Instead they are strongly bound with holes to form excitons<sup>4</sup> due to the low dielectric constant of a CP. To break apart the electron-hole pair within its short lifetime and a short diffusion length, effective electron acceptors have been investigated as a dispersed second component in the bulk heterojunction CP-based solar cells. Crystalline dyes and semiconductor nanorods as well as C<sub>60</sub> have been studied as electron acceptors. Once electrons and holes are separated, efficient transport of the charges to electrodes is another critical step in energy conversion. The importance of the charge transport has been demonstrated by dye-sensitized TiO<sub>2</sub> solar cells.<sup>5,6</sup> In these cells, the continuous TiO<sub>2</sub> phase simply plays a role as an electron transport material since it does not contribute to photon absorption. But efficient electron-transport through the continuous TiO<sub>2</sub> and fast hole-transport by electrolytes in the cells produce much higher PCE as compared to that of CP-based solar cells. In contrast, in most bulk heterojunction CP-based solar cells, large amounts of electron acceptors above their percolation threshold have been mixed to provide a pathway for electrons to reach the cathode. Therefore, the major transport mechanism of the charges in bulk heterojunction CP solar cells is electron hopping among dispersed electron acceptors in CP matrix<sup>7</sup>, much less effective than that of the TiO<sub>2</sub> cells. In this context, producing ordered continuous nano-scale multi-domains with large interfacial area is necessary to realize effective separation and transport of the charges.

## **6.2 Experimental**

### **6.2.1 Fabrication of the SiO<sub>2</sub> mold**

A 200-nm thick SiO<sub>2</sub> was thermally-grown on a Si wafer, then a 10-nm thick chrome (Cr) was deposited on the SiO<sub>2</sub> layer by using a radiofrequency (RF) sputtering. The roles of Cr layer are the improvement of adhesion properties between the photoresist and the SiO<sub>2</sub> layer as well as an etch mask to etch the SiO<sub>2</sub> layer.<sup>8</sup> A thin photoresist was spin-coated on the Cr layer, and laser interference lithography (LIL) was performed to form a grating pattern of 510-nm pitch and 700nm pitch on the PR. The Cr layer was etched with Cl<sub>2</sub> and O<sub>2</sub> reactive ion etching (RIE), and then SiO<sub>2</sub> layer with CHF<sub>3</sub> RIE. After etching the SiO<sub>2</sub>, the Cr mask was removed by Cr wet etchant. The He-Cd Laser used for LIL has a wavelength of 325 nm and a power of 50 mW. The periodic line grating patterns were obtained through the laser interference between the direct beam and the reflected beam from the mirror. The period of the line patterns can be adjusted by changing the stage angle. The fabricated mold was pretreated by an anti-sticking layer (1H, 1H, 2H, 2H Perfluorodecyl trichlorosilane)<sup>3</sup> to prevent the mold from adhering to the imprinted patterns during the mold separation step.

### **6.2.2 Device fabrication and characterization**

Samples used in the fabrication of the solar cell were prepared as follows: TDPTD (3mg/ml) in chlorobenzene was spin-coated on a clean ITO-coated PET substrate at 800 rpm for 1 min and baked at 130°C for 1 hr under inert conditions (to remove the remaining solvent.) To minimize oxidation, prepared samples were stored in a portable vacuum chamber before imprinting. An NIL system of Nanonex-2000 was used to pattern the TDPTD film. The sample stage was heated to 180°C and then imprinted by using the SiO<sub>2</sub> mold at a pressure of 600 psi for 5 min. The sample stage was cooled to room temperature by a N<sub>2</sub> flow. After that, the mold was released from the sample. During the imprinting process TDPTD becomes insoluble, and a solution of PCBM in chlorobenzene was spincast on the imprinted sample and baked at 130°C without affecting the imprinted TDPTD layer. A 100 nm Al layer was then deposited on the baked PCBM layer at 2Å/sec under 10<sup>-6</sup>torr by thermal evaporation. Fabricated

photovoltaic cells were characterized by an HP 4156B Semiconductor Analyzer and a 150 W Oriel solar simulator under  $56\text{mW}/\text{cm}^2$  intensity.



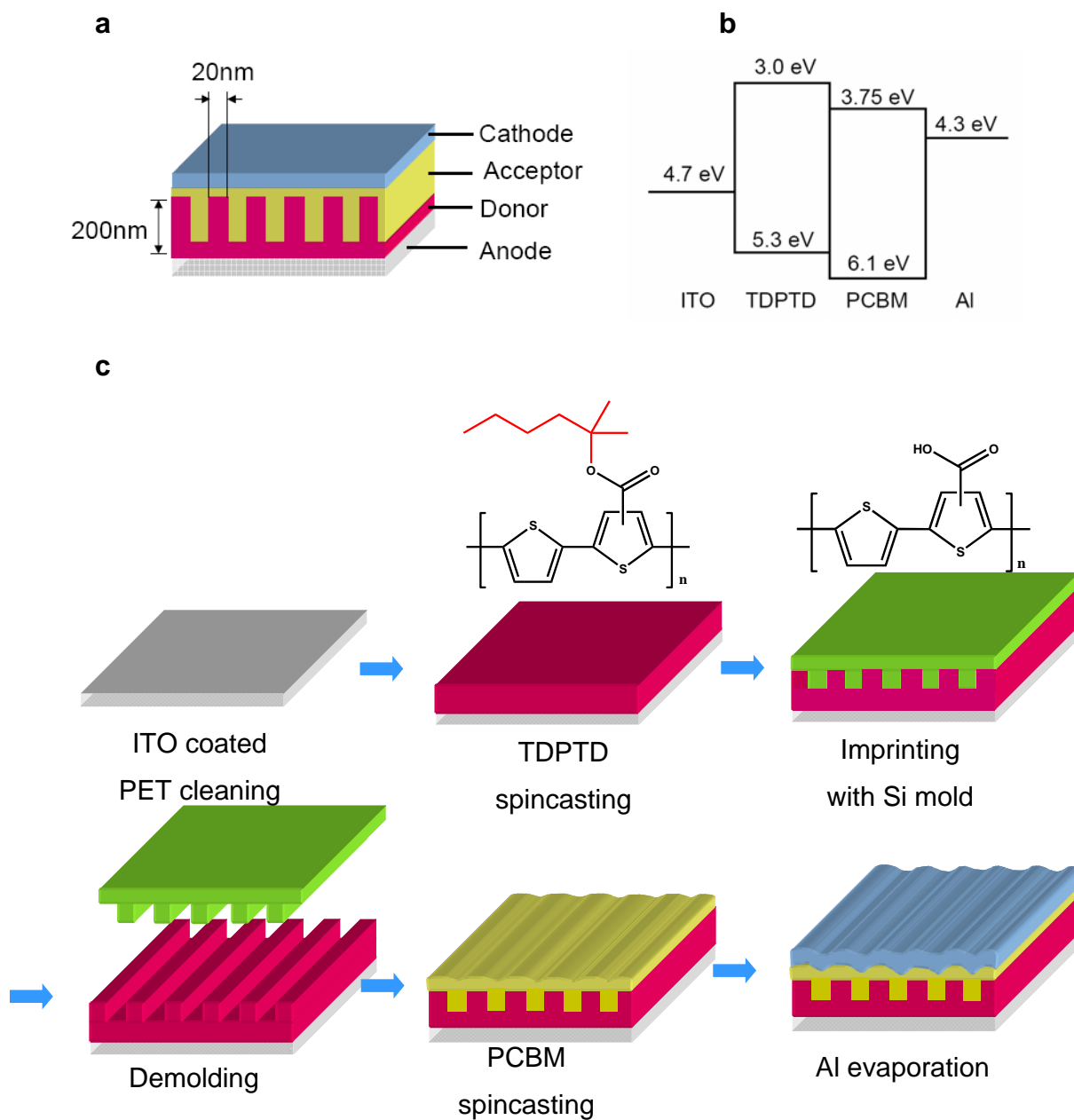


**Figure 6.1.** Nanostructured conjugated polymer solar cells fabricated using NIL. **a**, An proposed organic photovoltaic cell structure is depicted. Polymer thickness is 200 nm absorbing over 95% of incident light and the pattern width is 20 nm. **b**, Band structure of the fabricated cell. **c**, Device fabrication procedure and deprotection chemistry.

## 6.3 Results and discussion

### 6.3.1 Design principle of nanostructured OPV cell

Figure 6.1. a) shows an structure of an organic photovoltaic cell, which has straight, continuous, and large heterojunctions between donor and acceptor so that charge separation and transport are facilitated. The optimum thickness of the CP layer is approximately 200 nm to absorb solar energy efficiently (for example, a 200 nm-thick P3HT layer absorbs over 95% incident light energy in the intrinsic absorption wavelength range).<sup>9</sup> The optimum pattern size should be on the order of the exciton diffusion length,  $L_D \approx 10 - 20$  nm. To realize the ideal cell structure, there are two possible top-down approaches. First, nanostructured inorganic electron-transporting materials can be prepared followed by infiltration of the nanochannels with energy harvesting and hole-transporting CPs. Considering the large molecular weight of a CP and the nanosize channels, this approach has an intrinsic difficulty in CP infiltration and the ensuing disordered CP structure that induces inefficient hole transport.<sup>10</sup> The other approach is to nanopattern the energy harvesting and hole-transporting CP layer and subsequently coat the surface with electron accepting/transporting materials. This second approach unlikely has the disordered CP structure and low hole mobility issue that is commonly found in infiltrated conjugated polymers. In fact, our preliminary results using XRD have shown that the crystallinity of a regioregular poly(3-hexylthiophene) films is improved during the nanoimprinting process (see supporting materials).

### 6.3.2 Nanoimprinting lithography as a patterning tool

We used nanoimprint lithography (NIL), an emerging technology enabling low-cost and high-throughput nanofabrications<sup>3, 11</sup> to produce well-defined ordered nanostructural heterojunction CP solar cells (Figure 6.2). The ordered heterojunction having a large surface area allows efficient charge separation and the vertically oriented feature provides a line-of-sight pathway for rapid charge transport toward the electrodes while minimizing the probability of charge recombinations.<sup>7,12</sup> In this paper we present how the nanoimprinting lithography (NIL) can be used to produce defined nanostructured heterojunction solar cells and be used to systematically study the correlation between the interface area/structure and the PV cell performance.

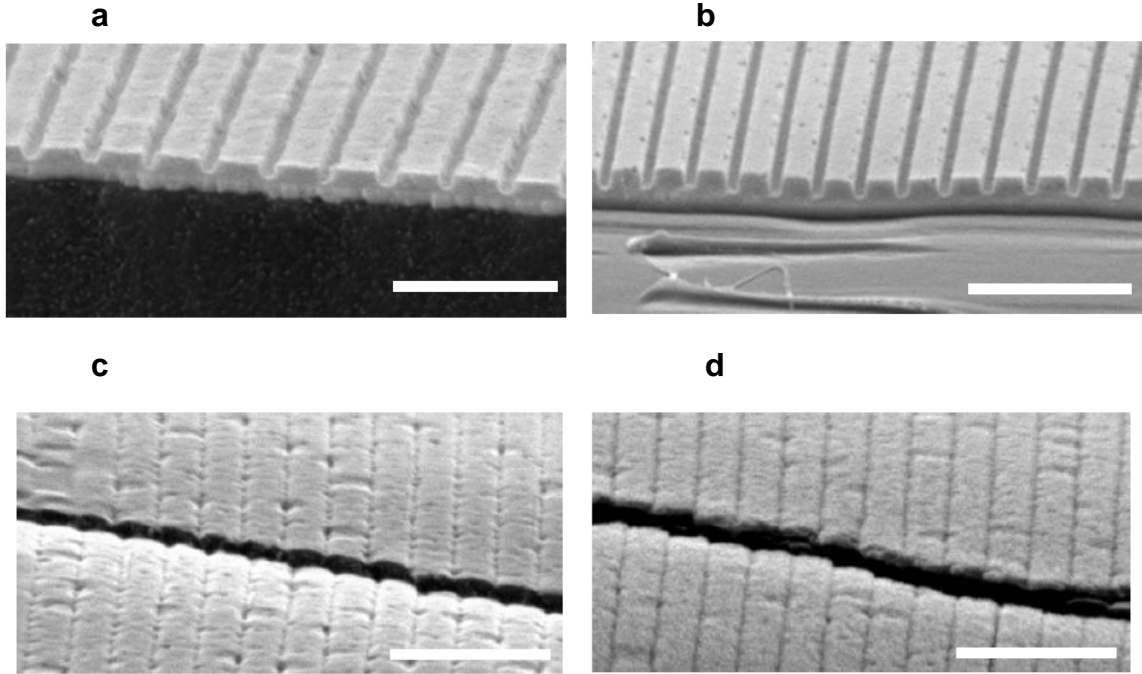


**Figure 6.2.** SEM images a, TDPTD on a flexible ITO-coated PET was imprinted with a 700 nm period grating mold. (Pattern period: 700nm, depth: 200nm, top width: 520nm, open width: 180nm) b, TDPTD on a flexible ITO-coated PET was imprinted with a 510 nm period grating mold. (Pattern period: 510nm, depth: 200nm, top width: 380nm, open width: 130nm) c, After PCBM coating on the imprinted TDPTD with the 510 nm period. In contrast to Fig. 2b, the deep trenches are completely filled with PCBM. d, Al (100 nm thickness) was evaporated at  $2 \text{ \AA}/\text{sec}$  under  $10^{-6}$  torr on the PCBM layer. The scale bars shown in the images are  $2 \mu\text{m}$ .

In NIL, a mold with nanopatterns can be prepared by applying the electron beam lithography or the optical projection lithography. Even though these lithography techniques are low throughput and high cost methods, once the mold is fabricated the nanopatterns can be easily replicated onto thin layer polymer films multiple times by imprinting the mold as a stamp on the polymer thin layer. The currently achievable smallest feature size through the nanoimprinting is below  $10 \text{ nm}$ <sup>13, 14</sup> Therefore, considering  $L_D \approx 10 - 20 \text{ nm}$ , nanoimprinting can potentially enable a solar cell having the optimized length scale of donor-acceptor layer integration. In this investigation 510nm period and 700nm period grating molds were used for imprinting to prove the feasibility and concept of the controlled nanoscale heterojunction first. We have observed a systematic increase in PV efficiency by reducing the feature size. Molds with smaller

features are being produced and the nanoimprinted solar cells with the smaller features will be investigated in due course.

To apply NIL for organic photovoltaic cell (OPVC) fabrication we optimized imprinting pressure, temperature, imprinting time, and demolding conditions (see the experimental section). In the beginning we investigated P3HT and C<sub>60</sub> system. P3HT was imprinted and then C<sub>60</sub> was deposited on the imprinted P3HT in a vacuum chamber. However, conformal C<sub>60</sub> coating on the imprinted P3HT surface was not successful due to the shadow effect in the evaporation process. Instead, mushroom-like discontinuous C<sub>60</sub> film was deposited, resulting in a poor performance of the cells. To achieve uniform and conformal coating of C<sub>60</sub> we changed the processing method from vacuum evaporation to solution casting. During the solution casting of the electron acceptors the nanopatterned conjugated polymer film has to maintain its structure. This inevitably requires us to use an insoluble conjugated polymer and a soluble electron acceptor. We used PCBM ([6,6]-phenyl-C<sub>61</sub> butyric acid methyl ester), a soluble C<sub>60</sub> derivative, and the thermally deprotectable polythiophene derivative (TDPTD) Frechet *et. al.* developed as an insoluble CP.<sup>15</sup> The pristine form of this polymer is solution processible. However because the long branched alkyl side chain is removable by heating the polymer becomes insoluble after nanoimprinting at 180 °C. Figure **6.1. b)** shows the bandgap structure of the four components of the nanoimprinted solar cells.

The overall device fabrication process is illustrated in figure **6.1. c)**. We used ITO-coated PET as a flexible substrate. Conjugated polymer solar cells on a plastic substrate have advantages of light weight, flexibility, good toughness, and possible cost effective roll-to-roll fabrication. On an ITO-coated PET TDPTD was spincast. After baking, TDPTD was imprinted with two different molds with grating structures: 510nm period and 700nm period with 200nm depth. The grating patterns of the molds were effectively transferred to TDPTD layer. Figure **6.2 a)** and **b)** show the cross sectional SEM images. The inset of figure **6.3** shows the imprinted TDPTD layer with the 700nm-period mold, as evidenced by the multicolor appearance due to the diffraction of ambient light. After imprinting, PCBM dissolved in chlorobenzene was spincast to conformally coat the imprinted TDPTD surface (figure **6.2 c)**. Finally Al was deposited on PCBM layer to complete the device fabrication (figure **6.2 d)**. The fabricated cells were

characterized by using Oriel solar simulator at  $56\text{mW}/\text{cm}^2$  illumination intensity. The resulting flexible PV cell is shown in figure 6.3.

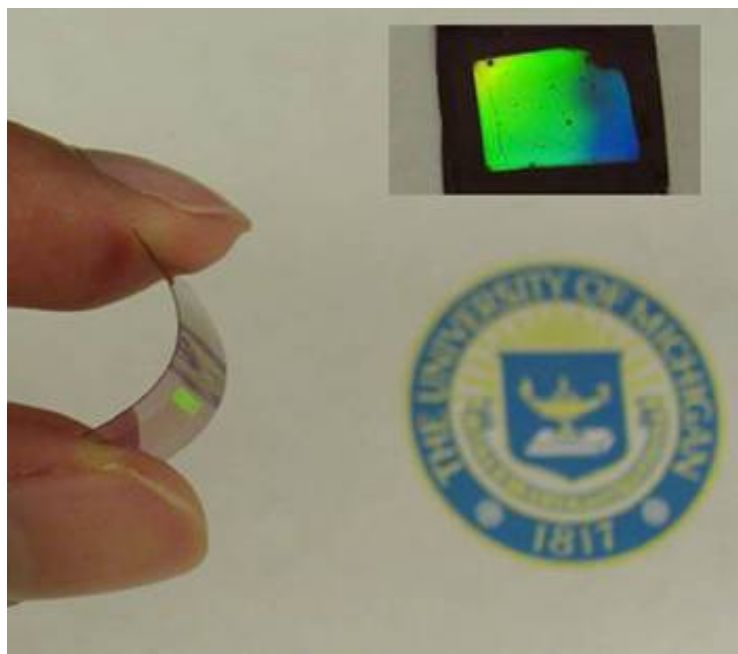


**Figure 6.3.** A flexible conjugated polymer solar cell with controlled nanoscale heterojunctions. TDPTD on a flexible ITO-coated PET was imprinted with a 700 nm period grating mold. Insert, the imprinted pattern shows a bright light diffraction.

### 6.3.3 Performance enhancement of nanostructured OPV cell

We analyzed the cell performance by measuring the J-V curve. Flexible solar cells with three different structures were compared (control cells with a flat interface and nanostructured cells with 510 nm and 700 nm periodicity). The J-V curve clearly shows that as the interface area between the donor and the acceptor increases short circuit current density increases (figure 6.4 a). The effect of interface area on the short circuit current is plotted in figure 6.4 b). The short circuit current linearly increases as the interface area increases. This clearly supports the working principle of organic photovoltaic cell that the excitons are separated at the donor/acceptor interface and also demonstrates that the interface area is directly related to amount of charge generation.

Interestingly, the ratio of the increased short circuit current to the surface area gain (the slope of the figure 6.4 b)) is 1.39, larger than 1:1 correlation. We attribute this additional synergic effect to the improved charge transport pathways provided by the continuous electron acceptor layer.

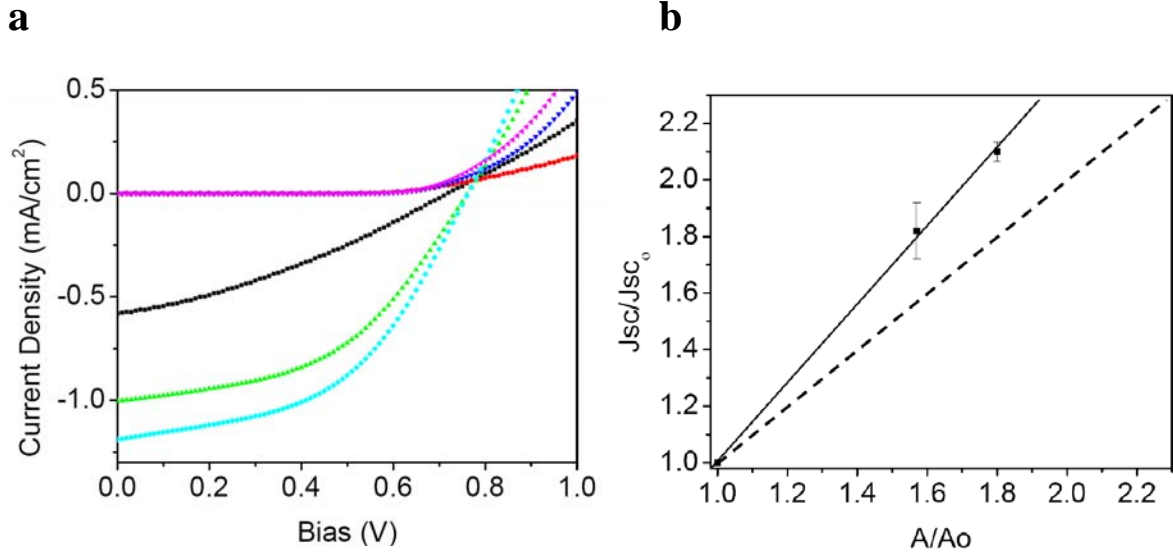


**Figure 6.4.** Characterization of the device performance. a, J-V curves of the flexible conjugated polymer solar cells. The control PV cell(●), the imprinted PV cell having the 700 nm(▼) period, and the imprinted cell having the 510 nm(◀) period under dark condition. The control cell(■), the imprinted cell having the 700 nm(▲) period, and the imprinted cell having the 510 nm(◆) period under illuminated condition (56mW/cm<sup>2</sup> intensity). b, The effect of the vertically oriented interface areas between TDPTD and PCBM is plotted. The interface areas are 0.79 mm<sup>2</sup> for control cell, 1.24 mm<sup>2</sup> for the nanopatterned cell having the 700 nm period, and 1.42 mm<sup>2</sup> for the nanopatterned cell having the 510 nm period. As interface area increases the short circuit current density increases. (Jsc/Jsc<sub>0</sub>: the ratio of the Jsc of the cells to the Jsc of the control cell, A/A<sub>0</sub>: the ratio of the interface area of the cells to the interface area of the control cell, Solid line: linear fit of data, Dashed line: 1:1 line of Jsc/Jsc<sub>0</sub> and A/A<sub>0</sub>).

The fill factor, open circuit voltage, and power conversion efficiency are listed in Table 6.1. The fill factor has a relationship with the resistance of the cell.<sup>16</sup> When the shunt resistance to prevent leakage currents is high and the series resistance to get a sharp rise is low high FF is obtained in the forward current. As we can see in Table 6.1, the fill factors of the nanostructured cells are 0.47 and 0.48 for the 700 nm and 510 nm period, respectively, larger than 0.34 of the control cell that has a flat interface. As described earlier the vertically oriented interfaces can provide a straight pathway for efficient

charge transport once the excitons dissociates to electrons and holes at the interfaces. Due to this synergistic effects the power conversion efficiency of the nanostructured cells with 510 nm and 700 nm period are 3.20 and 2.64 times larger than that of the control cell, respectively, even though the actual interface area increases 1.75 and 1.5 times only.

**Table 6.1** The performance of the flexible solar cells with controlled nanostructures

	$A/A_0^*$	$J_{sc}(mA/cm^2)$	$V_{oc}(V)$	FF	PCE(%)**
Control cell	1	0.58	0.78	0.34	0.25
Imprinted cell (700nm)	1.57	1	0.78	0.47	0.66
Imprinted cell (510nm)	1.80	1.19	0.78	0.48	0.80

\*  $A/A_0$ : The ratio of the interface area of the cell to the interface area of the control cell.

\*\* Illumination intensity:  $56mW/cm^2$ .

The large open circuit voltage  $V_{oc}$  of the device also draws our attention. Usually organic PV cells show the  $V_{oc}$  of about 0.6 V<sup>17,18</sup> but the  $V_{oc}$  of our cells is 0.78V. When we made a control cell with a flat interface on a ITO-coated PET out of P3HT, C<sub>60</sub>, and Al we observed a  $V_{oc}$  of 0.4-0.5V. There is no firmly established understanding on what determines the  $V_{oc}$ . One hypothesis on  $V_{oc}$  is that the open circuit voltage is related to the work functions of the two electrodes.<sup>19,20</sup> On the other hand, recently some observations have been made that  $V_{oc}$  is related to the semiconducting materials between the two electrodes.<sup>21,22</sup> Our results strongly support the second hypothesis.

## 6.4 Conclusions

In summary, we successfully applied nanoimprinting technology to conjugated polymers and fabricated flexible solar cells with well-controlled nanostructural heterojunctions. The experimental data clearly showed that the short circuit current linearly increases as the donor/acceptor interface area increases. Moreover, the incensement of the short circuit current is more than the actual gain of the interfacial suggesting an additional orientational benefit of the imprinted heterojunction. The fill factor was also significantly increased in the nanoimprinted PV cells with vertically oriented heterojunctions. This synergistic performance enhancement is believed to be originated from the achieved vertically oriented heterojunctions that facilitate charge transport as well as charge separation. We are currently developing molds with a smaller feature size and expanding the nanoimprinting techniques to multicomponent conjugated polymer photovoltaic cells.



## 6.5 References

1. Yu, G., Gao, J., Hummelen, J. C., Wudl, F. & Heeger, A. J., *Science*, **270**, 1789-1791 (1995).
2. Wendy U. Huynh, Janke J. Dittmer & A. Paul Alivisatos, *Science*, **295**, 2425-2427 (2002).
3. L. J. Guo, *J. Phys. D: Appl. Phys.*, **37**, R123-R141 (2004).
4. Tang, C. W., *Appl. Phys. Lett.*, **48**, 183-185 (1986).
5. Brian O'Regan & Michael Grätzel, *Nature*, **353**, 737-740 (1991).
6. Marketa Zukalova, Arnost Zukal, Ladislav Kavan, Mohammad k. Nazeeruddin, Paul Liska & Michael Grätzel, *Nano Lett.*, **5**, 1789-1792 (2005).
7. Jinsong Liu, Toru Tanaka, Kevin Sivula, A. Paul Alivisatos & Jean M. J. Fréchet, *J. Am. Chem.*, **126**, 6550-6551 (2004).
8. Seh-Won Ahn *et al*, *Nanotechnology*, **16**, 1874–1877 (2005)
9. Kevin M. Coakley & Michael D. McGehee, *Chem. Mater.*, **16**, 4533-4542 (2004).
10. Kevin M. Coakley, Yuxiang Liu, Michael D. McGehee, Karen L. Frindell & Galen D. Stucky, *Adv. Funct. Mater.*, **13**, 301-306 (2003).
11. Chou S Y, Krauss P R & Renstrom P J, *Appl. Phys. Lett.*, **67**, 3114-3116 (1995).
12. Fan Yang, Max Shtein & Stephen R. Forrest, *Nature Materials*, **4**, 37-41 (2005).
13. S. Y. Chou, P. R. Krauss, W. Zhang, L. J. Guo, and L. Zhuang, *J. Vac. Sci. Technol. B*, **15**, 2897-2904 (1997).
14. Zhaoning Yu, Paru Deshpande, Wei Wu, Jian Wang & Stephen Y. Chou, *Appl. Phys. Lett.*, **77**, 927-929 (2000).
15. Jinsong Liu, Ekaterina N. Kadnikova, Yuxiang Liu, Michael D. McGehee, & Jean M. J. Fréchet, *J. Am. Chem.*, **126**, 9486-9487 (2004).
16. Harald Hoppe & Niyazi Serdar Sariciftci, *J. Mater. Res.*, **19**, 1924-1945 (2004).
17. Gang Li, Vishal Shrotriya, Jinsong Huang, Yan Yao, Tom Moriarty, Keith Emery & Yang Yang, *Nature Materials*, **4**, 864-868 (2005).
18. Wanli Ma, Cuiying Yang, Xiong Gong, Kwanghee Lee & Alan j. Heeger, *Adv. Funct. Mater.*, **15**, 1617-1622 (2005).
19. V.D. Mihailetschi, P.W.M. Blom, J.C. Hummelen, & M.T. Rispens, *J. Appl. Phys.* **94**, 6849-6854 (2003).

- 
20. H. Frohne, S.E. Shaheen, C.J. Brabec, D.C. Müller, N.S. Sariciftci, & K. Meerholz, *Chem Phys Chem.* **9**, 795-799 (2002).
  21. C.M. Ramsdale, J.A. Barker, A.C. Arias, J.D. MacKenzie, R.H. Friend & N.C. Greenham, *J. Appl. Phys.*, **92**, 4266-4270 (2002).
  22. J. A. Barker, C.M. Ramsdale, & N.C. Greenham. *Phys. Rev. B*, **67**, 075205 (2003).

## CHAPTER 7

### SUB MICROMETER SCALE PATTERNED ORGANIC PHOTOVOLTAIC DEVICE USING TiO<sub>2</sub> AND P3HT

#### 7.1 Introduction

To improve the power conversion efficiency of an organic photovoltaic device, organic photovoltaic devices having a sub-micrometer scale pattern were fabricated. The device structure was FTO/TiO<sub>2</sub>/P3HT/gold. In order to investigate the relationship between the cell performance and the patterned TiO<sub>2</sub> layer, a control OPV cell having a flat bilayer structure was also fabricated. The patterning on the TiO<sub>2</sub> layer was conducted by means of nanoimprint lithography (NIL) with a sub-micrometer scale PMDS mold. The patterned device showed improved PCE up to 40% compared with the control cell. Our investigation showed that the performance enhancement originates from the increased interface area between the donor and the acceptor as well as the improved absorption efficiency due to the extended light travel distance induced by light scattering at the patterned interface.

Organic photovoltaic technology has attracted great attention due to the potentially economic fabrication cost, light weight, foldable and rollable advantage.<sup>1</sup> However, the performance of organic photovoltaic cell (OPVC) still suffers from its low power conversion efficiency mainly due to the low hole mobility through the organic layer and the short exciton travel distance.<sup>2,3,4,5,6,7,8</sup> OPVC having disordered bulk heterojunctions are most popular due to the easy fabrication by spin cast and reasonable power conversion efficiency.<sup>9,10,11</sup> However, the random bulk heterojunction produces a larger than ideal feature size considering 10 – 20 nm of exciton diffusion length. Therefore, the exciton separation at the heterojunction interface is not efficient even much better than that in the bilayer cells. Charge transport can be hampered at the cur-de-

sec areas as well. Recently reported well-visualized images of the phase separated blend layer showed that PCBM aggregates are embedded in the entangled fibril-like structure of P3HT. During the charge transport through this entangled and disordered structure, charge recombination, i.e. back electron transfer, can be more prone to occurring.<sup>1</sup>

To overcome the drawbacks of the heterojunctional OPV cell, the idea of the nanostructured OPV cells was developed. These devices have nanoscaled interfaces of the donor and the acceptor and this small feature is anticipated to improve the exciton dissociation efficiency and lower the chance of back electron transfer due to the straight and shorter interfaces.<sup>12,13</sup> Various strategies have been reported to realize the idealized nanostructured OPV cells. Nanostructured OPV cells were fabricated by growing needle-shaped CuPc followed by conformal coating of PTCBI.<sup>14</sup> The PCE was improved due to the 2.5 times increased interface area between the donor and the acceptor compared to the analogous cells having a flat interface. Nanostructured OPV cells having pillars of anatase TiO<sub>2</sub> covered with P3HT were also reported to have 2-3 times improved performance compared with the analogous cells having a flat interface.<sup>12</sup> Another example is the nanostructured PV cells having the patterned CuPc and C<sub>60</sub> bilayer Cocoyer *et al.* reported.<sup>15</sup> The cells having the sub-micrometer scale feature showed enhanced photocurrent due to the light entrapping effect by the sub-micrometer feature. The light entrapping effect by sub-micrometer scale patterns of OPV cells was also observed from the OPV having patterned poly(3-hexylthiophene) and soluble C<sub>60</sub> derivative.<sup>16</sup>

## 7.2 Experimental

In this investigation, we fabricated TiO<sub>2</sub> layers having sub-micrometer scale patterns by applying nanoimprint lithography.<sup>17</sup> To form the n-type anatase TiO<sub>2</sub>, we used a commercially available organic titanate as the precursor of titania, N-butyl polytitanate, n-C<sub>4</sub>H<sub>9</sub>O-[Ti-(O-n-C<sub>4</sub>H<sub>9</sub>)<sub>2</sub>O]<sub>n</sub>-n-C<sub>4</sub>H<sub>9</sub> having the molecular weight of ~ 1250 g/mol. 6.25 g of n-butyl polytitanate (Tyzor® BTP, DuPont, Wilmington, Delaware) was reacted with 4.46 g of benzoylacetone (BzAc, Aldrich) to synthesize a chelated precursor. The chelated precursor was dissolved in propylene glycol propyl ether (PGPE) to make a 30 wt% solution.

The OPV cell structure was FTO on glass/ patterned TiO<sub>2</sub>/ P3HT/ gold. To investigate the patterning effect, an analogous control cell having a flat bilayer structure was also fabricated. After the FTO coated glass substrate was cleaned, the TiO<sub>2</sub> precursor was spincoated at 1500 rpm for 1 min. and calcined at 450°C for 1 hr. to form anatase TiO<sub>2</sub>. During the calcination, the furnace chamber was filled with oxygen to promote the removal of the organic side groups of the precursor. To pattern the TiO<sub>2</sub> layer nanoimprint lithography (NIL) was applied and the detailed processing conditions are described in the next paragraph. After NIL process, the patterned TiO<sub>2</sub> was calcined again with the same condition of the previous calcination. Then P3HT solution in chlorobenzene (10 mg/ml) was spincoated on the patterned TiO<sub>2</sub> and the device was annealed at 130°C for 5 min. 100 nm thick gold anode was vacuum evaporated under 10<sup>-6</sup> torr and the devices were post annealed to complete the OPV cell fabrication.

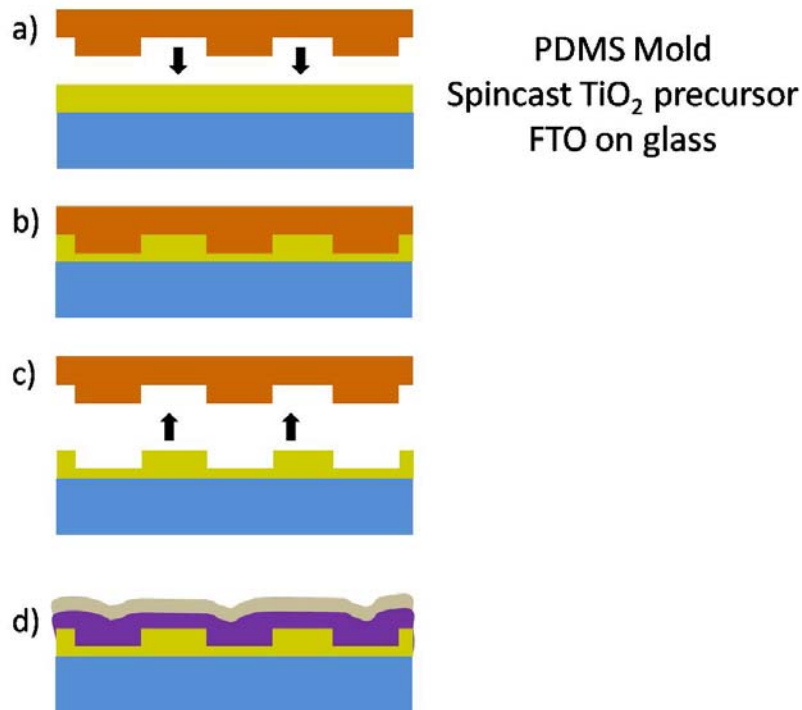


**Figure 7.1.** Device fabrication scheme a) – b) Spin cast TiO<sub>2</sub> precursor imprint using PDMS mold, c) Demolding and calcination at 450°C for 90min. and d) P3HT casting and gold deposition.

The TiO<sub>2</sub> precursor doesn't have glass transition temperature requiring careful optimization of the NIL process. First, a flexible PDMS mold having the grating pattern was fabricated and used as a mold for the nanoimprinting. The recently developed high modulus PDMS2 was used to make the mold fabrication easy and the detailed fabrication procedure of the PDMS stamp can be found elsewhere.<sup>18,19</sup> The fabricated PDMS grating pattern has the period of 700 nm, depth of 180 nm, and the line width of 200 nm. The TiO<sub>2</sub> precursor solution was spincast on the FTO-coated glass substrate at a 1000 rpm for 30 sec. and the PDMS stamp was then applied on the TiO<sub>2</sub> film to transfer the pattern. A Nanonex NX 2000 nanoimprinter (Princeton, NJ) was used to apply a uniform pressure of 50 psi and a temperature of 130 °C for 5 min. Unlike other common thermoplastic materials (e.g. PMMA) for NIL, TiO<sub>2</sub> was imprinted without solvent evaporation step. It turned out that a pressure of 50 psi was enough to create the nanoscale pattern, and 130 °C was only used to bake TiO<sub>2</sub> layer during imprinting. The residual solvent after spin-casting is believed to be evacuated during NIL. Even though the original TiO<sub>2</sub> pattern had a depth of 180 nm after NIL, the final TiO<sub>2</sub> pattern had only 90 nm of depth and the

changed duty cycle as shown in Figure 7.2. The changes in the feature size was made due to the shrinkage during the sintering process.

### 7.3 Results and discussion

After establishing the fabrication process for TiO<sub>2</sub> patterning using NIL, a flat control cell was fabricated for accurate comparisons of the device performance. To achieve highly reproducible performance of the devices the effective variables had to be optimized. Since TiO<sub>2</sub> precursor we formulated was a novel precursor every processing step had to be carefully examined. First, as the anatase formation from the TiO<sub>2</sub> precursor is a critical step to achieve excellent device performance, the crystallinity of the film was verified by XRD. We varied the calcination temperature from 130°C to 500°C and examined the correlation between the calcinations temperature and the anatase formation. XRD data from the specimens calcined between 300 and 500°C showed peaks corresponding to the (001) and (201) plane confirming the anatase formation. Next, the thin film quality from the spin cast TiO<sub>2</sub> precursor to the calcined one was carefully investigated since a uniform and defect-free TiO<sub>2</sub> layer having 100~200 nm thickness is essential to make a well-performing photodiode. As described in the device fabrication procedure, we prepared the TiO<sub>2</sub> layer through two times calcinations to efficiently remove any pin holes possibly existing in the spin cast layer and to achieve more stable photodiode behavior. To confirm the consistency of device performance, multiple devices having the same feature size were fabricated on a substrate and those having various sizes of devices were fabricated on another substrate. The short circuit current density and the power conversion efficiency of all control cells varied within the 8% error range. Lastly, after P3HT casting on the TiO<sub>2</sub> layer the device was carefully annealed for 15 minutes to induce better molecular packing of P3HT. Additionally, in order to achieve improved charge collection the device was post annealed at 130°C after the gold anode deposition. The J<sub>sc</sub> of the annealed OPV cell increased from 0.2 mA/cm<sup>2</sup> to 0.3 mA/cm<sup>2</sup>. This enhancement can be attributed to a facilitated charge collection induced by the better contact between P3HT and the gold anode through the thermal annealing process.



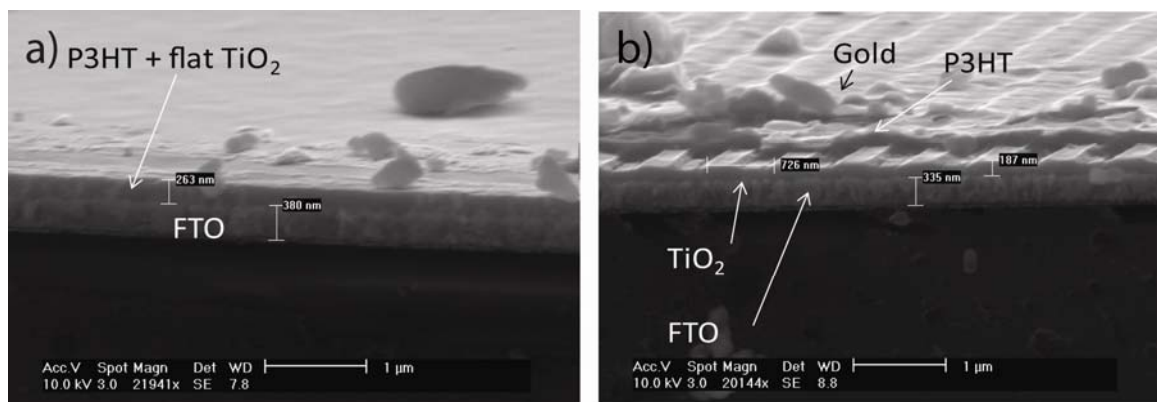


**Figure 7.2.** SEM images of the patterned  $\text{TiO}_2$  a) flat bilayer of  $\text{TiO}_2$  and P3HT and b) the OPV device having the sub-micrometer pattern of P3HT and gold electrode.

After establishing the optimization of the  $\text{TiO}_2$  patterning process and the performance reliability of the flat control cells, the OPV cells having sub-micrometer scale pattern were fabricated to investigate the effect of the patterned  $\text{TiO}_2$  on the device performance. In Figure 7.3 (right) the JV curves of the control cell and the patterned cell are plotted. The imprinted cell showed 1.53 times improved photogenerated current density compared with the performance of the flat control cell. Because the exciton dissociation occurs at the interface between the donor and the acceptor the performance enhancement can be attributed to the increased interface area. However, because the imprinted  $\text{TiO}_2$  had 90 nm depth, 1:1 duty ratio, and the 700nm period the imprinted cell should have only 1.2 times increased interface area of the donor and the acceptor compared with that of the flat control cell. Therefore, the origin of the additional performance enhancement was investigated. We could verify that the extended travel distance of the absorbed sun light inside the patterned OPV cell contributes to the extra performance improvement. In Figure 7.3 (left), the absorption spectra of the patterned OPV cell is plotted. First, flat  $\text{TiO}_2$  film has relatively weak absorption and there are two maximum peaks at 530 nm and 670 nm. The patterned  $\text{TiO}_2$  film is showing distinguished absorption peaks at 320, 360 and 480 nm. This patterned film was coated with P3HT and the plot in red is showing the overlapped absorption from the patterned  $\text{TiO}_2$  and P3HT.

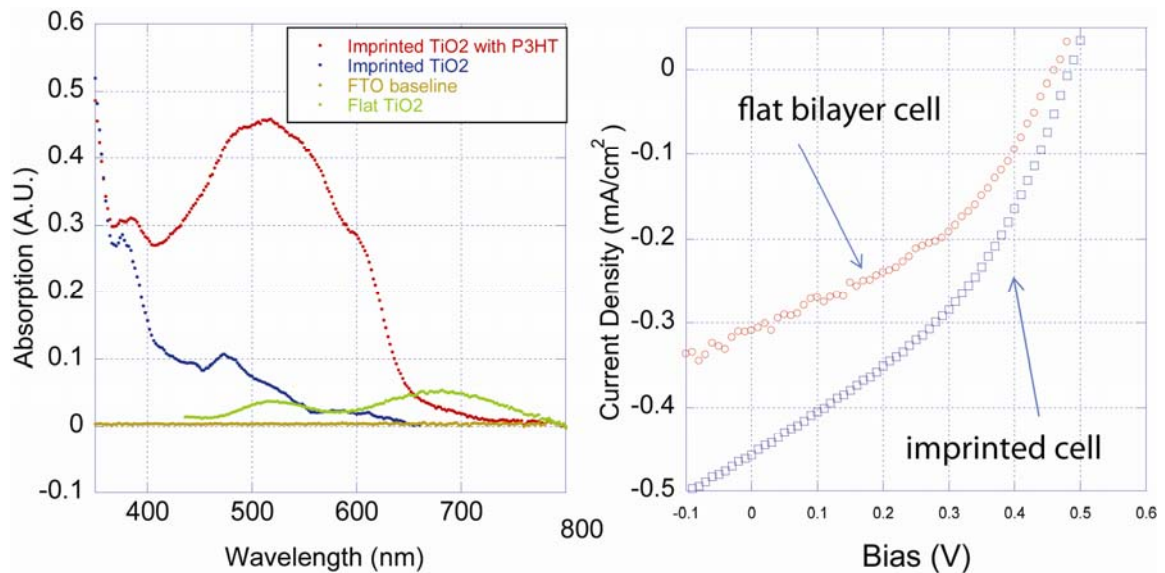


**Figure 7.3.** Absorption spectra of OPV cell (left), and JV curves of the control cell (red open circle) and the imprinted cell (blue open square) (right).

The nature of absorption peaks was carefully investigated. Since TiO<sub>2</sub> layer is quite transparent film, absorption peaks of patterned TiO<sub>2</sub> layer in the visual light range cannot be explained by the absorption of light in the material. Because the sub micrometer scale pattern is known to cause light scattering due to the pattern, the absorption peaks of the patterned TiO<sub>2</sub> is believed to be originated from the refracted light by the sub micrometer scale pattern.

## 7.4 Conclusions

In summary, a novel spin castable  $\text{TiO}_2$  precursor was synthesized and the cells composed of a bilayer of  $\text{TiO}_2$  from the precursor and P3HT showed reasonable photovoltaic behavior. We built patterned  $\text{TiO}_2$  layers by applying nanoimprint lithography and investigated the effects of the patterned  $\text{TiO}_2$  layer to the performance of the OPV. The performance improvement by increasing the interface between the donor and the acceptor was successfully demonstrated by comparing the performance between the OPV cells having sub-micrometer scale pattern with the analogous cells having a flat interface. The improved performance of the OPV cells having the sub-micrometer scale pattern can be attributed to that the increased interface area of the donor and the acceptor facilitate exciton dissociation as well as light entrapping effect at the patterned interface.

## 7.5 References

1. K. M. Coakley and M. D. McGehee, *Chem. Mater.* **16**, 4533 (2004).
2. Halls *et al.*, *Appl. Phys. Lett.* **68**, 3120 (1996).
3. L.S. Roman and O.J. Inganas L.A.A. Petterson, *J. Appl. Phys.* **86**, 487 (1999).
4. Theander *et al.*, *Phys. Rev. B.* **61**, 12957 (2000).
5. J. M. Warman and A. Goossens T.J. Savenije, *Chem. Phys. Lett.* **287**, 148 (1998).
6. Stephen R. Forrest, *MRS bulletin* **30**, 28 (2006).
7. Grozema *et al.*, *J. Phys. Chem. B* **106**, 7791 (2002).
8. Sirringhaus *et al.*, *Nature* **401**, 685 (1999).
9. Gang Li *et al.*, *Nature Materials* **4**, 864 (2005).
10. J. Y. Kim *et al.*, *Science* **317**, 222 (2007).
11. Y. Kim *et al.*, *Nature Materials* **5**, 197 (2006).
12. Williams *et al.*, *Chem. Mater.* **20**, 5229 (2008).
13. Jung-Min Kima Hyun-Jung Hera, C.J. Kanga, and Yong-Sang Kim, *J. Phys. Chem. Solids* **69**, 1301 (2008).
14. F. Yang *et al.*, *Nature Materials* **4**, 37 (2005).
15. Cocoyer *et al.*, *Appl. Phys. Lett.* **88**, 133108 (2006).
16. Na *et al.*, *Appl. Phys. Lett.* **91**, 173509 (2007).
17. L. J. Guo, *Adv. Mater.* **19** (495) (2007).
18. J.-S. Kim C. Pina-Hernandez, L. J. Guo, and P.-F. Fu, *Adv. Mater.* **19**, 1222 (2007).
19. M.-G. Kang and L. J. Guo, *J. Vac. Sci. Technol. B* **25**, 2637 (2007).

## CHAPTER 8

### CONCLUSIONS

#### 8.1 Conclusions

Through this thesis performance reproducibility issue, working device principles, accurate performance characterization, and the photovoltaic cells having controlled nanostructures are systematically discussed. In the following sections the conclusions of each subject are summarized.

##### 8.1.1 Highly reproducible performance of blend OPV cell

The reproducibility issue of OPV has not yet been clearly addressed for several reasons. First, establishing highly reproducible performance of OPV cells requires tremendous trial and error, and poorly reproducible performance is believed to be an intrinsic drawback of organic electronic devices. The poorly reproducible performance of OPV cells is similarly explained as the result of an electrical property of  $\mu\text{c-Si}$ , of which the morphology is not easy to control consistently. The  $\mu\text{c-Si}$  structure has crystalline domains and grain boundaries; therefore, achieving uniform charge transport in the thin film is challenging. Organic thin film consists of the assembly of many semiconducting organics where crystalline or amorphous regions exist together. It was believed that this morphology induces poor reproducibility of organic electronic devices, and in reality, many researchers experienced significant performance variation even though devices were fabricated using a consistent procedure. Therefore, the research community in organic electronics has shared doubts about whether organic electronic devices can be fabricated with excellent performance reproducibility.

In the device fabrication, there are several process variables: blend solution preparation method, blend ratio, blend layer thickness, PEDOT:PSS thickness, various kinds of PEDOT:PSS with different conductivity, spincoating conditions, cathode structure, annealing conditions and method, oxygen and moisture exposure, encapsulation, illumination set-up, characterization set-up, etc. Among these, blend layer quality and LiF layer greatly affect device performance reproducibility. When the blend layer was poorly prepared, the blend layer included aggregates of the organic semiconductor, which created barriers or charge trappers in the semiconducting layer. To remove aggregates, the blend solution should be carefully prepared to minimize the aggregates with filtering. Use of a thin LiF layer with aluminum as a cathode also significantly improved reproducibility. LiF layer plays an ideal role as an interfacial layer to transfer charges from the blend layer to the cathode without loss. However, slight atmospheric exposure to the device during fabrication and characterization did not significantly lower the reproducibility of OPV cell performance.

After optimizing the process of device fabrication, the performance variation of OPV cell was less than 7% in terms of  $J_{sc}$  and PCE. This reproducibility was tested and concluded by analyzing the performance of multiple devices fabricated in different batches using the same fabrication conditions. This report of outstanding reproducibility means it is possible to set a high standard of device performance with small variations, and enable the deriving of conclusions by comparing the result from devices fabricated with experimental concepts to the result from control devices with small variation.

### **8.1.2 The relations between fill factor and resistance**

The photovoltaic behavior of OPV cells was understood in terms of fill factor (FF), which characterizes the shape of the JV curve in the 4<sup>th</sup> quadrant. The FF in blend OPV cells has correlations with series resistance ( $R_s$ ) and shunt resistance ( $R_{sh}$ ), which are individually controlled by manipulating effective variables such as crystallization of semiconducting organics, region regularity of polymers, and blend layer thickness, as well as cathode structure and anode conductivity in the interfaces between blend layer and electrodes.

In the blend layer, first, the crystallinity of the conjugated polymer was controlled by thermal annealing. After P3HT and PCBM solution casting, the blend layer was

annealed. As the blend layer was annealed, the crystallinity of P3HT increased, resulting in improved hole mobility in P3HT. This self-aggregation is induced by the strong packing of hexyl side groups and thiophene rings, which enhances intra and inter molecular charge transfer. As a result, the  $R_s$  of OPV cells decreased, and FF increased. Next, depending on the region regularity of the conjugated polymer, resulting  $R_{sh}$  was significantly affected.  $R_{sh}$  can be correlated with charge leakage in the device since region random polymers have lower mobility and therefore there is more chance of charge recombination. Also the poor packing of conjugated polymers results in less efficient intermolecular charge transfer. The last variable in the blend layer was layer thickness. As the thickness increased,  $R_s$  increased and  $R_{sh}$  decreased. As the device gets thicker, the charge path distance increases, and therefore  $R_s$  increases. In addition, as the device got thicker,  $R_{sh}$  decreased; in other words, the device had more charge leakage. Since thicker films have more chance of having charge traps or barriers, the resulting  $R_{sh}$  decreased.

In the interface between the cathode and blend layer, the defect at the interface was controlled using aluminum cathode without LiF. In chapter three, it was observed that LiF plays a role in transferring charges efficiently from blend layer to cathode. Without LiF, the charge transfer from the blend layer and cathode is not efficient because of defects at the interface. By using only aluminum as the cathode, the defects were intentionally embedded in the interface and removed using thermal annealing for 15 to 20 min. After depositing aluminum, the device had interface defects and  $R_{sh}$  was relatively low. This is interpreted to mean that the photogenerated charges are dissipated during transfer from blend layer to cathode due to defects. As the device was annealed,  $R_{sh}$  got higher, and after 15 min of annealing, the resulting FF was almost 60%. This number is the same as the FF from the OPV cell containing LiF.

Finally, the conductivity of anodes was also varied. We used three kinds of anodes: PEDOT:PSS ( $\sigma = 100$  S/cm), PEDOT:PSS with DMS (300S/cm), and PEDOT:PSS on ITO ( $10^5 \sim 10^6$  S/cm). As the conductivity of the anode decreased, charge collection from the blend layer to the electrode was limited and  $R_{sh}$  decreased. When anode conductivity decreases, charges are accumulated near the electrode and have more chance for recombination. Therefore, resulting FF decreased due to low  $R_{sh}$ . On

the other hand, when the conductivity of the anode increased, charges were efficiently collected at the electrode without recombination due to charge accumulation, and FF increased to 60%.

### **8.1.3 Accurate characterization**

To evaluate the performance of organic photovoltaic devices in a precise manner, accurate device characterization is important. In the sense that establishing optimized characterization set-up is technically complex, and generally accepted characterization protocols are not available, there are many chances to include errors in device performance characterization.

Therefore, we carefully investigated possible mistakes during characterization. The electrode configurations - crossbar shape electrodes and island shape electrodes - affect PCE significantly. OPV cells having crossbar shape electrode configurations included overestimation of PCE originating from PEDOT:PSS/ P3HT+ PCBM/ LiF/ Al. PEDOT:PSS has lower conductivity compared to ITO, but it works as an electrode collecting charges.

This observation was verified by varying PEDOT:PSS conductivity and illumination area on OPV cells having crossbar electrode configuration. As PEDOT:PSS conductivity increased, the extra charge collection area in the device increased and the characterized performance included an extra current, which explained overestimation of performance. In addition, depending on the illumination area, the device performance also varied. When simulated sunlight is illuminated, there exists a large enough diameter to cover the cross area of electrodes. overestimation of performance was also observed compared to the performance from the control device having island electrode configuration. This also supports the assumption that cross shape electrode configurations generate extra current from PEDOT:PSS/ P3HT +PCMB/ LiF/ Al outside of ITO/ PEDOT:PSS/ P3HT +PCMB/ LiF/ Al. To exclude the overestimation of current, the devices having cross bar shape configurations were cut using a knife; after removing two devices, PEDOT:PSS/ P3HT +PCMB/ LiF/ Al, the performance was exactly same as the performance of the device having island shape electrode configuration.

The observed overestimation of the device having a crossbar shape configuration ranged from 10 to 50% of the original performance of the cell having an island electrode



configuration. In order to increase confidence of the performance of OPV cells in the research community, generally acceptable criteria from device structures to characterization should be standardized after removing any possibility of overestimation of device performance.

#### **8.1.4 The performance enhancement of OPV cells that have a patterned interface between the donor and the acceptor**

The performance of OPV cells has been improved by using a blend OPV cell structure. The drawback of this structure is that the hole and electron conducting material is a randomly entangled structure that necessitates longer travel distance for charges. Also, due to the randomness of the morphology, there is a chance that isolated donor or acceptor material will occur in the blend layer, which is not connected to the electrode and that eventually charges will be dissipated by recombination or trapping.

As depicted in chapters six and seven, nanostructured cells were designed to increase the interface area of donor and acceptor, as well as incorporate a straight pathway between donor and acceptor to the electrodes.

To realize this concept, we applied nanoimprint lithography (NIL) to pattern the donor, a thermally deprotectable thiophene derivative. Since this investigation was initiated to measure the feasibility of this approach, we fabricated a prototype nanostructured OPV cell using a 700 and 510nm period pattern. After patterning the donor, PCBM was spincoated, and an aluminum cathode was finally deposited. To verify improvements, we also fabricated a FTO/ Patterned TiO<sub>2</sub>/ P3HT/ Gold device. In both cases, we observed PCE improvement depending on the interface area of donor and acceptor compared to the performance of a flat control cell.

In addition to the performance enhancement originating from the interface area of donor and acceptor, a light-trapping effect also affected performance improvement because of light refraction on the patterned structure. When the incident light was refracted on the patterned structure of the OPV cell, the pathway of light was extended and eventually light absorption efficiency was enhanced.

This investigation demonstrated the possibility of achieving further improvement of OPV cell performance in that NIL can be successfully applied for OPV cell fabrication,

and that a 20 to 40nm genuine nanostructured OPV cell with maximized exciton dissociation efficiency, as well as charge transport efficiency, can be fabricated.